**Title**
Molecular solution processing of metal chalcogenide thin film solar cells

**Permalink**
https://escholarship.org/uc/item/6hg907d4

**Author**
Yang, Wenbing

**Publication Date**
2013

Peer reviewed|Thesis/dissertation

UNIVERSITY OF CALIFORNIA

Los Angeles

Molecular solution processing of metal chalcogenide thin film solar cells

A dissertation submitted in partial satisfaction

of the requirements for the degree

Doctor of Philosophy

in Materials Science and Engineering

by

Wenbing Yang

2013

Abstract of the Dissertation

# Molecular solution processing of metal chalcogenide thin film solar cells

by

## Wenbing Yang

Doctor of Philosophy in Materials Science and Engineering

University of California, Los Angeles, 2013

Professor Yang Yang, Chair

The barrier to utilize solar generated electricity mainly comes from their higher cost relative to fossil fuels. However, innovations with new materials and processing techniques can potentially make cost effective photovoltaics. One such strategy is to develop solution processed photovoltaics which avoid the expensive vacuum processing required by traditional solar cells. The dissertation is mainly focused on two absorber material system for thin film solar cells: chalcopyrite $CuIn(S,Se)_2$ (CISS) and kesterite $Cu_2ZnSn(S,Se)_4$ organized in chronological order.

Chalcopyrite CISS is a very promising material. It has been demonstrated to achieve the highest efficiency among thin film solar cells. Scaled-up industry production at present has reached the giga-watt per year level. The process however mainly relies on vacuum systems which account for a significant percentage of the manufacturing cost. In the first section of this dissertation, hydrazine based solution processed CISS has been explored. The focus of the research involves the procedures to fabricate devices from solution. The topics covered in Chapter 2 include: precursor solution synthesis with a focus on understanding the solution chemistry, CISS absorber formation from precursor, properties modification toward favorable device performance, and device structure innovation toward tandem device.

For photovoltaics to have a significant impact toward meeting energy demands, the annual production capability needs to be on TW-level. On such a level, raw materials supply of rare elements (indium for CIS or tellurium for CdTe) will be the bottleneck limiting the scalability. Replacing indium with zinc and tin, earth abundant kesterite CZTS exhibits great potential to reach the goal of TW-level with no limitations on raw material availability. Chapter 3 shows pioneering work towards solution processing of CZTS film at low temperature. The solution processed devices show performances which rival vacuum-based techniques and is partially attributed to the ease in controlling composition and CZTS phase through this technique. Based on this platform, comprehensive characterization on CZTS devices is carried out including solar cells and transistors. Especially defects properties are exploited in Chapter 4 targeting to identify the limiting factors for further improvement on CZTS solar cells efficiency. Finally, molecular structures and precursor solution stability have been explored, potentially to provide a universal approach to process multinary compounds.

The dissertation of Wenbing Yang is approved.

_____

Yang Yang, Committee Chair

_____

Sarah Tolbert

_____

Suneel Kodambaka

_____

Yu Huang

**University of California, Los Angeles**

**2013**

*The dissertation is dedicated to my parents for their love*

*and pursuit of higher education opportunities for me.*

# Table of Contents

**List of Figures**

**Chapter 1**

Chapter 2

x

**Chapter 3**

**Chapter 4**

**Chapter 5**

**Chapter 6**

**List of Tables**

**Chapter 2**

**Chapter 4**

# Acknowledgements

I would like to acknowledge many people for their inspiration, mentoring, encouragement and support. Without their priceless help, I could not imagine how to complete my PhD, not even to mention the born of this dissertation. First of all, I owned the deepest gratitude to my advisor professor Yang Yang for offering me the research opportunity at 2008 and providing full support ever since. I acknowledge the culture of "find way out" professor Yang Yang established in the group that brings me inspiration and freedom to initiate new direction. Thank professor Yang Yang for the guidance through challenges on research and project growth. The training process enables me independent thinking and proactive action toward the best. I would also like to acknowledge my committee members professor Sarah Tolbert, professor Yu Huang, professor Suneel Kodambaka for valuable inputs.

Special thanks to Dr William Hou for his mentoring on research, and help on experiment techniques when I first started research project in the lab. His vision, analytical thinking, detail-oriented attitude have constant influence on my research career at UCLA. Thanks Dr Bao Lei for guidance on research report and sharing his own software for data analysis. Thanks Dr Sheng-Han Li for sharing experience to move CIGS project forward and strong problem-solving skills on facilities. I also own great gratitude to other senior labmates for teaching me their experiment skills and offer their friendship to make lab interesting as well: thank Dr Li-Men Chen, Dr Zheng Xu, Dr. Ankit Kumar for sharing expertise of XPS technique; Dr. Guanwen Yang and Dr Kitty Cha on AFM, Dr. Juo-Hao Li on polymer LED, Dr. Wei Lek Kwan on transistor characterization, Dr. Srinivas Sista

on transient absorption, Dr. Ziruo Hong, Dr. Mi Hyae Park, Dr Hsing-Yu Chen, Ms Teresa Chen, Ms Huai-Hsuan Tsai, Ms Renee Green. All their help allows me to integrate with the lab efficiently and go through hard time.

Thanks Mr Brion Bob for help on the first edition of proposals that initiated CZTS research. Thanks Mr Shin-Sheng Duan for the collaborative work to move CZTS technique forward quickly. Thanks Dr Huanping Zhou for input of expertise on nonocrystal. Thanks Ms. Chia-Jung Hsu, Ms. Wan-Ching Hsu for the collective work on some CZTS project. Thanks Dr Choong-Heui Chung, Dr. Xiaohui Tan, Mr. Shenglin Ye, Mr. Tze-bin Song, Mr Eric Richard for the team work and valuable discussion on inorganic projects in our lab. I would also thank all my colleagues for their assistance. Beyond the lab, Dr. Saeed Khan provided valuable input on X-ray diffraction techniques; Dr. Qi Chen, Mr James Ma, Mr Min Xue and many others also provide valuable technical help assisting me to move forward.

Finally, I would like to thank my family, mom and dad, for your love, support and encouragement, especially your effort to create the opportunity never happened in your life. Your love gives me endless inspiration and spiritual power to overcome challenges in the last five years.

Chapter two is a version of "C.-H. Chung, S.-H. Li, B. Lei, W. Yang, W. W. Hou, B. Bob, and Y. Yang, Identification of the Molecular Precursors for Hydrazine Solution Processed CuIn(Se,S) 2 Films and Their Interactions, *Chemistry of Materials*, vol. 23, no.

4, pp. 964–969, Feb. 2011" and "A Simple Route for Alkali Metal Incorporation in Solution-Processed Crystalline Semiconductor, Internationla Patent Application No.: PCT/US2010/061323, UCLA Case No. 2008-552-2."

Chapter Three is a version of "W. Yang, H.-S. Duan, B. Bob, H. Zhou, B. Lei, C.-H. Chung, S.-H. Li, W. W. Hou, and Y. Yang, "Novel Solution Processing of High-Efficiency Earth-Abundant Cu(2) ZnSn(S,Se)(4) Solar Cells.," *Advanced materials*, vol. 24, no. 47, pp. 6323–6329, Sep. 2012."

Chapter Four and Chapter Five is a version of "H.-S. Duan, W. Yang, B. Bob, C.-J. Hsu, B. Lei, and Y. Yang, The Role of Sulfur in Solution-Processed Cu 2 ZnSn(S,Se) 4 and its Effect on Defect Properties, *Advanced Functional Materials*, DOI: 10.1002/adfm.201 201732, Oct. 2012." and "W. Yang, H. S. Duan, K. C. Cha, C. J. Hsu, W. C. Hsu, H. Zhou, B. Bob, Y. Yang, A Molecular Solution Approach to Synthesize Electronic Quality $Cu_2ZnSnS_4$ Thin Films, *JACS submitted*."

**VITA**

2007     Research Internship

       *Institute of Chemistry Chinese Academy of Sciences*

       *Beijing, China*


2008     B. S., Materials Science and Engineering

       University of Science and Technology of China

       Hefei, Anhui, China


2008-2012   Graduate Student Researcher

       University of California Los Angeles

       Los Angeles, California


2009     M. S. Materials Science and Engineering

       University of California Los Angeles

       Los Angeles, California

# Publications

[1] W. Yang, H.-S. Duan, B. Bob, H. Zhou, B. Lei, C.-H. Chung, S.-H. Li, W. W. Hou, and Y. Yang, "Novel Solution Processing of High-Efficiency Earth-Abundant Cu(2) ZnSn(S,Se)(4) Solar Cells.," *Advanced materials*, vol. 24, no. 47, pp. 6323–6329, Sep. 2012.

[2] H.-S. Duan, W. Yang, B. Bob, C.-J. Hsu, B. Lei, and Y. Yang, "The Role of Sulfur in Solution-Processed Cu 2 ZnSn(S,Se) 4 and its Effect on Defect Properties," *Advanced Functional Materials*, DOI: 10.1002/adfm.201201732, Oct. 2012.

[3] W.-C. Hsu, B. Bob, W. Yang, C.-H. Chung, and Y. Yang, "Reaction pathways for the formation of Cu2ZnSn(Se,S)4 absorber materials from liquid-phase hydrazine-based precursor inks," *Energy & Environmental Science*, vol. 5, no. 9, p. 8564, 2012.

[4] R. Zhu, C.-H. Chung, K. C. Cha, W. Yang, Y. B. Zheng, H. Zhou, T.-B. Song, C.-C. Chen, P. S. Weiss, G. Li, and Y. Yang, "Fused silver nanowires with metal oxide nanoparticles and organic polymers for highly transparent conductors.," *ACS nano*, vol. 5, no. 12, pp. 9877–82, Dec. 2011.

[5] B. Bob, B. Lei, C.-H. Chung, W. Yang, W.-C. Hsu, H.-S. Duan, W. W.-J. Hou, S.-H. Li, and Y. Yang, "The Development of Hydrazine-Processed Cu(In,Ga)(Se,S)2 Solar Cells," *Advanced Energy Materials*, vol. 2, no. 5, pp. 504–522, May 2012.

[6] B. Lei, W. W. Hou, S.-H. Li, W. Yang, C.-H. Chung, and Y. Yang, "Cadmium ion soaking treatment for solution processed CuInSxSe2−x solar cells and its effect on defect properties," *Solar Energy Materials and Solar Cells*, vol. 95, no. 8, pp. 2384–2389, Aug. 2011.

[7] C.-H. Chung, S.-H. Li, B. Lei, W. Yang, W. W. Hou, B. Bob, and Y. Yang, "Identification of the Molecular Precursors for Hydrazine Solution Processed CuIn(Se,S) 2 Films and Their Interactions," *Chemistry of Materials*, vol. 23, no. 4, pp. 964–969, Feb. 2011.

[8] H. Zhou, C.-J. Hsu, W.-C. Hsu, H.-S. Duan, C.-H. Chung, W. Yang, and Y. Yang, "Non-Hydrazine Solutions in Processing CuIn(S,Se) 2 Photovoltaic Devices from Hydrazinium Precursors," *Advanced Energy Materials*, p. n/a–n/a, Oct. 2012.

[9] W.-C. Hsu, I. Repins, C. Beall, C. DeHart, B. To, W. Yang, Y. Yang, and R. Noufi, "Growth mechanisms of co-evaporated kesterite: a comparison of Cu-rich and Zn-rich composition paths," *Progress in Photovoltaics: Research and Applications*, p. n/a–n/a, Nov. 2012.

[10] Y. Li, Z. W. Wang, C.-Y. Chiu, L. Ruan, W. Yang, Y. Yang, R. E. Palmer, and Y. Huang, "Synthesis of bimetallic Pt-Pd core-shell nanocrystals and their high

electrocatalytic activity modulated by Pd shell thickness.," *Nanoscale*, vol. 4, no. 3, pp. 845–51, Feb. 2012.

[11]  W. Yang, H.-S. Duan, B. Bob, B. Lei, S.-H. Li, and Y. Yang, "Novel solution processing of high efficiency earth abundant CZTSSe solar cells," in *2012 38th IEEE Photovoltaic Specialists Conference*, 2012, pp. 002664–002667.

[12]  C.-H. Chung, B. Lei, B. Bob, H.-S. Duan, S.-H. Li, W. W. Hou, W. Yang, and Y. Yang, "Molecular precursor species and their effects on the energy band-gap of hydrazine solution processed CuIn(S,Se)$_2$ films," in *2012 38th IEEE Photovoltaic Specialists Conference*, 2012, pp. 002640–002643.

[13]  B. Lei, C.-H. Chung, B. Bob, W. Hou, S.-H. Li, W. Yang, and Y. Yang, "Cadmium ion soaking treatment and defect characterizations of hydrazine processed CISS photovoltaic cells," in *2011 37th IEEE Photovoltaic Specialists Conference*, 2011, pp. 001298–001301.

# Chapter 1   Introduction

## 1.1   Motivation

"The stone age did not end because the world ran out of stones." Indeed, the stone age ended because humans discovered bronze, a technology that provides more desirable properties and greater functionality than stone. In the same way, dependence on oil for energy will end when human innovation finds alternative ways to produce sustainable and clean energy that are more desirable, functional and cost-effective than fossil fuels. Solar irradiation supplies an incredible amount of energy to the earth. The sun provides enough energy in one minute to supply the world's energy needs for one year. "The amount of solar radiation striking the earth over a three-day period is equivalent to the energy stored in all fossil energy sources." Harvesting energy directly from sunlight using photovoltaic (PV) technology is increasingly being recognized as an essential component of future global energy production. Solar electricity represents a direction of great potential toward a renewable, sustainable, and clean energy future while reducing the threat to the climate posed by green house gas emissions. Currently the main barrier to wide adoption of PV electricity is that fossil fuel is much more affordable. Constant innovation on new materials, processing, and devices is essential for PV technology to make a dent in our energy future.

To advance PV-electricity as an alternative resource, candidate material systems have to satisfy the critical parameters of equal importance: cost, efficiency, lifetime and materials availability beyond terra-watt production. Single crystalline GaAs and Si based materials have achieved the highest efficiency (beyond 40%), but the material quality requirements make their fabrication extremely expensive.[1-1][1-2]Organic photovoltaics from

polymer or small molecular materials, though consisting of earth abundant elements and potentially made using low cost fabrication, are tremendously prone to degradation by the environment. OPV is still in the academic incubator with efforts targeting higher efficiency and a way to address stability issue.[1-3] Metal chalcogenide based materials have demonstrated the highest efficiency in thin film solar cells.[1-2][1-4] The stability of chalcogenide materials enables a lifetime beyond 30 years. Their great tolerance of materials defects in particular reduces the requirement for high purity in fabrication and has motivated a variety of innovations in materials processing to substantially reduce their processing cost. [1-5]

## 1.2    Dissertation organization

The focus of the research is dedicated to an ultimate simple route to fabricate metal chalcogenide based thin film solar cells via molecular solution processing. Simplicity is the ultimate sophistication. This dissertation is organized in chronological order and describes the search for simple processing of chalcopyrite $Cu(InGa)(SSe)_2$ and new kesterite $Cu_2ZnSn(S, Se)_4$ material systems. The similarity of these materials systems enables us to have almost the same device processing procedures while their different constituents lead to totally different solution chemistry and device physics.

In chapter one, the solar cell operating principle is briefly introduced regarding the core component, the p-n junction. Device structure and general properties of CIS absorber materials are introduced. In the following research, we focused on material chemistry innovation for a simple molecular solution approach to process multinary compounds.

In chapter two, solution chemistry of hydrazine processed $CuInSe_2$ is first explored using solution Raman to prove soluble molecular structures. The mechanism inspired an expanded soluble copper precursor, from which a high efficiency CISS device was demonstrated. A transparent device structure based on CISS was studied potentially for tandem device application. An innovative approach to introduce sodium as an additive is also discussed to modify the CISS absorber to reduce carrier recombination.

In chapter 3, pioneering work on kesterite CZTS based solar cells is initiated. An innovative processing of CZTS was introduced to break the solubility limitation of zinc constituents in hydrazine for the first time to synthesize a molecular level homogenous precursor solution for producing chemically clean films. Simple molecular solution processing for multinary compounds was realized and could potentially be expanded to be a universal approach. From the precursor, the reaction mechanism of the formation of the CZTS phase is explored. A decent device was demonstrated, which generated the eighth-best reported efficiency at that time.

In the following chapters, CZTS materials properties and device physics, and solution chemistry are explored to advance the frontier of CZTS technology toward high efficiency. In Chapter 4, defect physics in CZTS devices with different band gap is explored. The compositional influence on device performance is discussed. The defect properties including defect concentration and energy levels are examined to identify that severe recombination accounts for the major losses. CZTS transistors are also explored with discussion of both their potential and barriers. The comparable mobility to CIS shows the promise of high efficiency CZTS with breakthroughs in defect manipulation to reduce charge traps.

In chapter 5, solution chemistry of this molecular solution system is explored. The soluble molecular structure is identified and the stability issue of precursor solution is addressed. The molecular structures also revealed the hidden roadmap for a potential universal way processing previously hard-to-dissolve elements. Based on identified molecular structures, other corresponding solvent systems could also be chosen to realize an environmentally friendly precursor solution with potential improvement of safety and toxicity. Finally the summary, chapter 6, overviewed the progress of solution processing CIGS and CZTS solar cells. The experience with CIGS materials inspired and contributes to the progress on the CZTS materials system, which takes advantages of the success of previous materials while slowly eliminating their disadvantages

## 1.3     Photovoltaic device theory

All photovoltaic devices work in essentially the same way: they contain a p-n junction formed by contacting a p-type and n-type material. In the junction, a build-in potential and electric field are created. Under illumination, photons are absorbed and create electron hole pairs in the semiconducting materials. The photo-generated electron hole pairs are separated by the internal electric field cross p-n junction and flow in opposite directions. As a result, photons are converted to electric flow through the process of light absorption, electron-hole generation, charge separation, and carrier collection by electrodes to drive continuous electric flow.
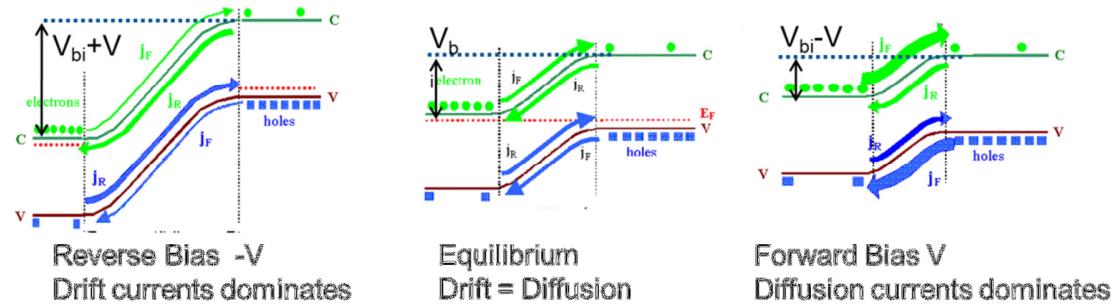
**Figure 1-1** p-n homojunction in the dark at reverse bias, in equilibrium and under forward bias.

A p-n junction is established when a p-type materials and an n-type material are brought together. Majority carrier (electrons in n-type materials and holes in p-type materials) diffuse across the interface, leaving behind a layer of fixed charge due to the ionized defects, on either side with opposite charges. The space charge region forms an electric potential to prevent further diffusion of majority carriers. Equilibrium is established when the diffusion of majority carriers is balanced by the drift of minority carriers. In the equilibrium condition, the Fermi levels of p- and n-materials are equal shown in figure 1-1. The difference in work function is taken up by a step in the conduction and valence bands, forming a build-in potential. The junction region, with the double layer of ionized defects, is depleted of free charges. This region is called a depletion region of the space charge region. With two oppositely charged depletion layers, the whole contact of p-and n-materials is still electrically neutral.

The drift current of minority carriers is limited by the diffusion of minority carrier to the edge of junction. The following flux of minority carriers across a p-n junction is fast. The drift current could be estimated from the diffusion of minority carriers within the distance of a diffusion length. In the example of p-type region, the minority carrier drift current is,

5

$$J_{o,n} = D\frac{\partial n}{\partial x} = \frac{n_i^2 D_n}{N_A L} \qquad (1.1)$$

Where $N_A$ is the density of dopants that contribute to the hole density, $D_A$ is the diffusivity of electrons in p-type materials, and $\frac{n_i^2}{N_A}$ is the equilibrium electron density in the p-type region. Similarly, the drift current for holes can be calculated from the n-type side.

When external bias is applied to a p-n junction, the Fermi level is split with one side higher with respect to the other, and the build in potential becomes ($V_{bi} - V$). In forward bias, the diffusion barrier for majority carrier decreased, so that majority carriers (electron from n-type) injected into the other side, increasing the minority carrier density exponentially. Thus the diffusion current will dominate. From the boundary condition at the interface between depletion region and neutral region indicates, the diffusion current could be derived:

$$J_n = D_n\frac{\partial n}{\partial x} = \frac{n_i^2 D_n}{N_A L}(e^{qV/kT} - 1) \qquad (1.2)$$

Where, $n = \frac{n_i^2 D_n}{N_A}e^{qV/kT}$ is the minority carrier concentration at the boundary injected from the other side. In reverse bias, the build in potential increases significantly and prevents the diffusion current of majority carriers. Drift current dominates. Similarly, on n-type side, the current contribution from holes will be:

$$J_p = D_p\frac{\partial p}{\partial x} = \frac{n_i^2 D_p}{N_D L}(e^{qV/kT} - 1) \qquad (1.3)$$

So a p-n junction has the rectifying effect indicated in equation 1.4. For an ideal diode, the current density varies like:

$$J_{dark}(V) = J_o(e^{qV/kT} - 1) \qquad (1.4)$$

$J_o = qn_i^2(\dfrac{D_n}{N_A L_n} + \dfrac{D_p}{N_D L_p})$ is the diffusion current, where the diffusion length $L = \sqrt{\tau D}$ is

determined by minority carrier lifetime.

Under light bias (figure 1-2), electron hole pairs generated in the depletion region and neutral region capable of diffusing into junction are separated by the build-in electric field. The opposite flow of electron and holes contribute to the photo-current, in a reverse direction as diffusion current in dark condition. For an ideal diode, as shown in figure 1-3 the current then becomes:

$$J_{light} = J_{sc} - J_o(e^{qV/kT} - 1) \quad (1.5)$$

Photo-generated carriers lead to splitting of the Fermi-level to different quasi Fermi levels on each side. At open circuit, the potential difference reaches its maximum—the open circuit voltage. For an ideal diode from Eq. 1.5, open circuit voltage

$$V_{oc} = \frac{kT}{q} \ln\left(\frac{J_{sc}}{J_o} - 1\right) \quad (1.6)$$
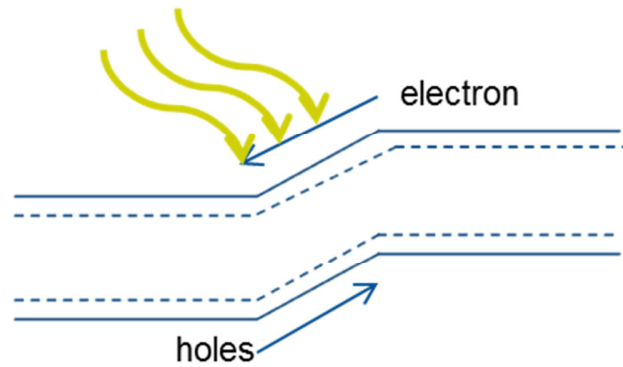
**Figure 1-2** p-n homojunction under illumination.
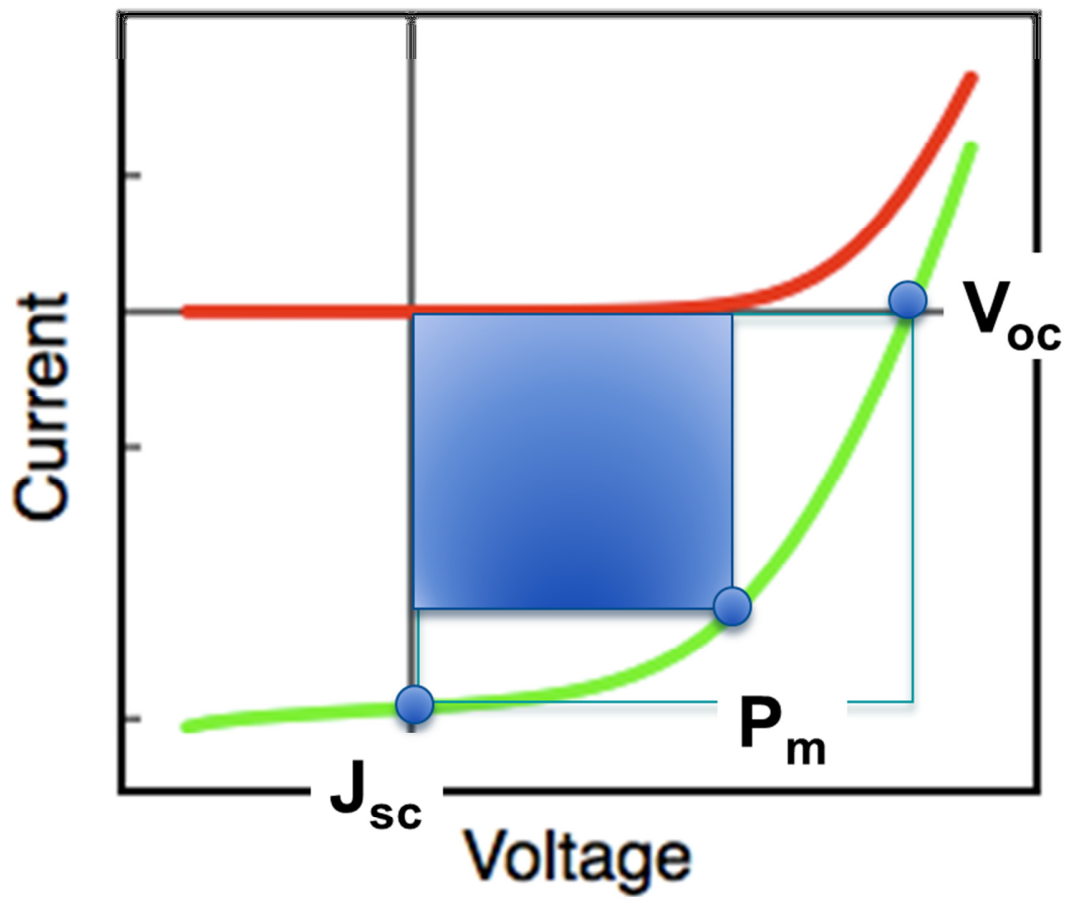


**Figure 1-3** The current voltage characteristics of a solar cell. The maximum powder density is given by the area of the inner rectangle.

The operating regime for solar cells is the range of bias from 0 to $V_{oc}$ so that the cell can generate power. The power that the cell can generate is determined by current density (J) and voltage (V):

$$P = JV \qquad (1.7)$$

The maximum power point $P_{max}$, occurs at a certain $V_m$ with a corresponding current density $J_m$. At the optimum load, the fill factor is defined as the ratio

$$FF = \frac{J_m V_m}{J_{sc} V_{oc}} \qquad (1.8)$$

Efficiency is determined by the maximum power that the cell can generate and the incident power density $P_s$.

$$\eta = \frac{J_{sc} V_{oc} FF}{P_s} \qquad (1.9)$$
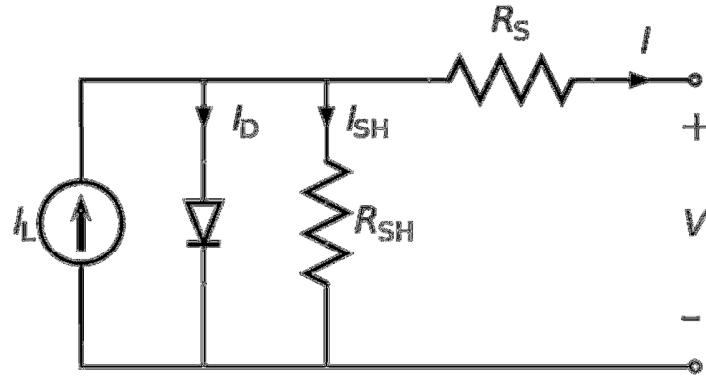


**Figure 1-4** Equivalent circuit of a solar cell including series and shunt resistance.

At standard testing conditions, air mass 1.5 spectrum, the incident power density is 1000 $W \cdot cm^{-1}$. The three parameters $J_{sc}$, $V_{oc}$ and FF are the key performance characteristics for a solar cell. In a real cell, power is dissipated through the serial resistance of contacts and cell materials, and leakage current across the junction of the device. A real solar cell can

be modeled with an equivalent circuit that has a current generator connected in parallel with a diode and a shunting path in series with a resistor as shown in figure 1-4. $R_s$ and $R_{sh}$ reduce the "square" of maximum power rectangle, compared with $V_{oc} \times J_{sc}$ and affect FF substantially.

## 1.4    Thin film materials & Processing innovation

## 1.4.1    CIS materials properties

Photovoltaic techniques could be divided into different categories based on their absorber materials. Devices based on silicon wafers, single or polycrystalline, have normally been termed as "first generation" PV technology.[1-6][1-7] Crystalline silicon is an indirect band gap semiconducting material. The band gap value is 1.1 eV. The homojunction has a significant advantage over a heterojunction since there is no material interface at the junction thus avoiding interface defects. For a single junction based device, a maximum theoretical power conversion efficiency of 31% under direct AM1.5 sunlight known as Shockley-Queisser limit.[1-8] The second generation technology focus on thin film materials, mainly including CdS/CdTe, Cu(In,Ga)Se2 (CIGS), and amorphous Si.[1-4][1-9] As direct band gap semiconducting materials, they have a dramatically increased light absorption coefficient compared with silicon. The absorption coefficient for CuInSe2 is very high, larger than $10^5$/cm for 1.4 eV and higher photon energies. A roughly 1 µm thick absorber is enough for light absorption across most of the sun's spectrum.

1200

1100

Liquid

1000

900

δ
(Sphalerite)

Cu$_2$Se + δ

T [°C]

800

β

β+γ

γ

In$_2$Se$_3$ + γ

700

Cu$_2$Se + CuInSe$_2$

CuInSe$_2$ (Chalcopyrite)

α

(Ordered Defect
Compound – ODC)

(Layered
Structure)

600

α+β

500

0    10    20    30    40    50    60    70    80    90    100

Cu$_2$Se                    X [mol. %]                    In$_2$Se$_3$
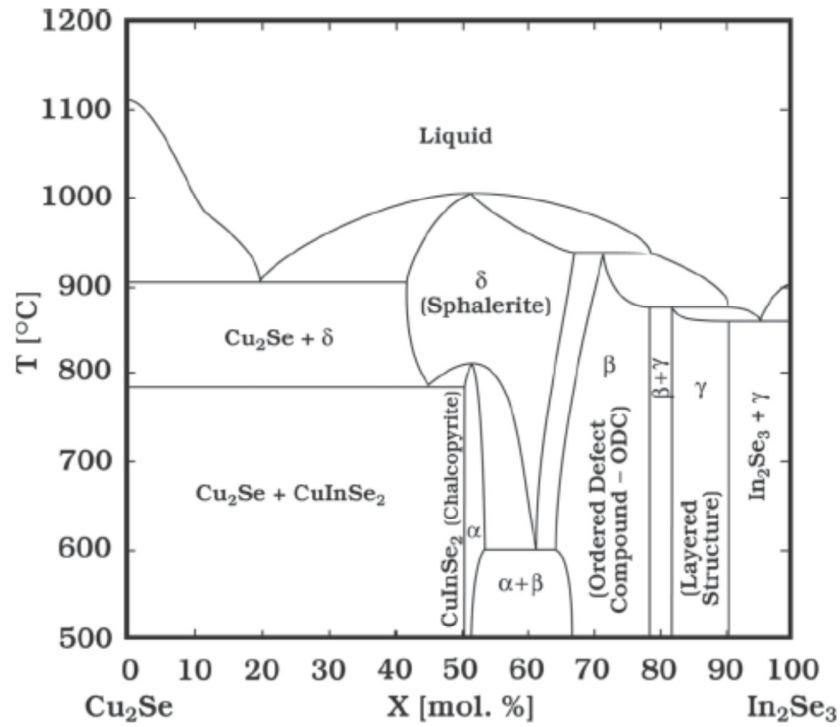
**Figure 1-5** CIS phase diagram along the Cu2Se–In2Se3 pseudobinary section of the Cu–In–Se chemical system.[1-10]

CIS materials have a chalcopyrite lattice structure. Chalcopyrite is a diamond-like structure similar to sphalerite (ZnS) but with an ordered substitution of group I and III on group II sites. This leads to a tetragonal unit cell with a ratio c/a close to 2. In the Cu-In-Se ternary phase diagram, the chalcopyrite phase and a variety of other ordered defect compounds (ODC) lie on the tie-line between Cu$_2$Se and In$_2$Se.[1-10] Chalcopyrite phase is thermally stable up to 900 °C. For In-rich stoichiometry, the ODC structure shares a similar lattice structure, but with ordered defects from the combination of V$_{cu}$ & In$_{Cu}$. These ODC compound actually show benign effects on actual device performance at the interface. Thus in practical synthesis, Cu-poor and In-rich composition is always targeted.

11

The wide tolerance of In/Cu ratio actually allows a variety of processing approaches to obtain device quality CIS phase.

$CuInSe_2$ has a band gap of 1.04 eV. The valence band maximum is formed by Cu-d and Se-p orbitals, and the conduction band minimum is formed by . Alloying of Ga on group III sites or S on Se-sites changes the lattice constant, thus effectively modifying the band gap. The relation between Ga/In ratio and band gap is calculated approximately as:

$$E_g = 1.010 + 0.626x - 0.167x(1-x) \qquad (1.10)$$

Currently, the demonstrated champion cells based on chalcopyrite materials have a Ga/(In+Ga) ratio of 0.3, which corresponds to a band gap of 1.15 eV. [1-11] Different from the doping mechanism in silicon (using extrinsic dopants to manipulate conductivity) intrinsic defects in CIS lattice contribute its p-type doping. Copper vacancies ($V_{cu}$) from the lattice are the main acceptor defects contributing p-type doping, with an energy level ~30 meV above VBM.[1-12]Selenium vacancy ($V_{Se}$) is a typical n-type compensating donor in p-type CIS materials. So the growth condition for CIS is, in practice, a chalcogen rich environment, with a slightly Cu-poor stoichiometry. Device quality CIS films have a carrier concentration around $10^{16}$ $cm^{-3}$. [1-13]

### 1.4.2 Device structure

For thin film solar cells based on a p-type absorber layer, the following device structure in Figure 1-6 is normally adopted.
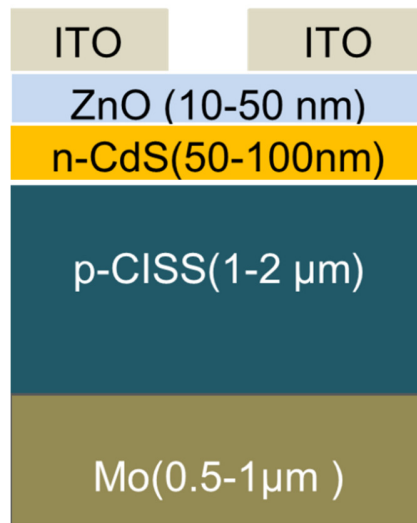
**Figure 1-6** Schematic device structure of a standard CISS thin film solar cell.

Mo is used for the back contact to provide an ohmic contact with CIS. The thermal and chemical stability of Mo allows the subsequent processing of a CIS absorber layer to yield a chemically pure film. The similarity of thermal expansion coefficient between Mo and chalcopyrite CIS also enables the heating process involved. For a CIS absorber layer, 1-2 um is enough for light absorption. The n-type CdS is a heavily doped emitter that extends most of the depletion region in CIS absorber layer, favorable for carrier collection in p-type region. A buffer layer of undoped high-resistivity (HR) ZnO is deposited before sputter deposition of the TCO layer. One practical reason for using an HR ZnO buffer layer is to add protection for the interface region from sputter damage induced during deposition of the TCO layer, which typically requires more harsh conditions. Finally, transparent top contact ITO is used to collect carriers extracted from the p-n junction. High conductivity and transparency are the two main properties of the TCO which contribute to high performance solar cells.[1-14]

[1-1]  "NREL champion cell chart," can be found under
       http://www.nrel.gov/ncpv/images/efficiency_chart.jpg, **n.d.**

[1-2]  M. A. Green, K. Emery, Y. Hishikawa, W. Warta, E. D. Dunlop, *Progress in Photovoltaics: Research and Applications* **2012**, *20*, 12–20.

[1-3]  G. Li, R. Zhu, Y. Yang, *Nature Photonics* **2012**, *6*, 153–161.

[1-4]  O. Morton, *Nature* **2006**, *443*, 19–22.

[1-5]  P. J. Dale, K. Hoenes, J. Scragg, S. Siebentritt, *2009 34th IEEE Photovoltaic Specialists Conference (PVSC)* **2009**, 002080–002085.

[1-6]  D. Ginley, N. Renewable, *MRS Bulletin* **2008**, *33*, 355–373.

[1-7]  M. A. Green, *Progress in Photovoltaics: Research and Applications* **2009**, *17*, 183–189.

[1-8]  W. Shockley, H. J. Queisser, *Journal of Applied Physics* **1961**, *32*, 510.

[1-9]  A. Shah, *Science* **1999**, *285*, 692–698.

[1-10] B. J. Stanbery, *Critical Reviews in Solid State and Materials Sciences* **2002**, *27*, 73–117.

[1-11] I. Repins, M. A. Contreras, B. Egaas, C. DeHart, J. Scharf, C. L. Perkins, B. To, R. Noufi, *Progress in Photovoltaics: Research and Applications* **2008**, *16*, 235–239.

[1-12] W. N. Shafarman, L. Stolt, *Cu ( InGa ) Se 2 Solar Cells*, **2003**.

[1-13] B. Lei, C.-H. Chung, B. Bob, W. Hou, S.-H. Li, W. Yang, Y. Yang, in *2011 37th IEEE Photovoltaic Specialists Conference*, IEEE, **2011**, pp. 001298–001301.

[1-14] I. Repins, S. Glynn, J. Duenow, T. J. Coutts, W. K. Metzger, M. A. Contreras, in *Proceedings of SPIE* (Eds.: A.E. Delahoy, L.A. Eldada), Spie, **2009**, p. 74090M–74090M–14.

# Chapter 2. Solution processing of CISS solar cells

## 2.1 Introduction

CIGS materials show the capability to be deposited on cheap substrates through a variety of deposition approaches. This materials system has achieved environmental stability and high durability without involving toxic elements. As its laboratory demonstrated cell efficiencies are currently beyond 20%,[2-1][2-2] and module efficiencies are now over 17%,[2-3]increasing emphasis has been focused on CIGS based materials. On the industrial production level, giga-watt production has been achieved by the company Solar Frontier,[2-4] which is currently the closest competitor to the CdTe-based thin-film PV module manufacturer First Solar.[2-5]

In an effort to pave the way toward cost effective module production, a variety of solution processing techniques have been developed targeting the removal of expensive vacuum processing equipment.[2-6] Non-vacuum based approaches include electrochemical deposition, spray pyrolysis, and nanoparticle deposition. The trade-off between low cost processing and reduced material quality leads to some intrinsic limitations on those approaches,[2-7] mainly including: (i) incorporation of carbon, oxygen, and other impurities from the precursors or starting solutions; (ii) the need for multistep processing (e.g., a typical nanoparticle process involves making metal oxide nanoparticles, depositing the oxides as films, reducing the films to metals using a high temperature reduction step, followed by high-temperature selenization); (iii) the requirement for a high-temperature selenization/sulfurization step using toxic gases (e.g., $H_2Se$) [2-8]and/or a post-deposition cyanide-bath etch to achieve adequate grain growth and improve phase purity.

Hydrazine based molecular solution processing provides an ideal route to substantially simplify the fabrication processes for CISS films.[2-9][2-10][2-11] The route is based on a molecular precursor consisting of metal chalcogenide anions separated by volatile hydrazinium cations and hydrazine molecules. Hydrazine is able to drive the unique chemistry required to dissolve a number of metal chalcogenide compounds.[2-12][2-13][2-14] [2-15][2-16] In a hydrazine environment, excess sulfur or selenium breaks the three-dimensional metal-chalcogenide solid frameworks, and form lower dimensional soluble molecular complexes. The resulting homogenous solutions enable the deposition of high quality uniform precursor films. An intermediate heat treatment causes the dissociation and decomposition of hydrazine/hydrazinium species into gaseous products. It thus has the advantages, compared with other solution approaches, to generate a chemically clean CIS film at low temperatures. [2-17]

In this chapter, the mechanism to dissolve $Cu_2S$ and $In_2Se_3$ into hydrazine was explored by identifying the molecular species in solution. The resulting molecular structures also inspired the discovery of a route to dissolve the previously insoluble $Cu_2Se$ compound in hydrazine. The dissolution strategies adopted here provide a mechanism to expand the realms of materials that hydrazine can process as a molecular solution. An approach to introduce sodium from precursor will also be introduced here to assist with the passivation of defects in the CISS absorber layer. Based on this solution processed absorber layer, a transparent device structure is demonstrated with the potential to build tandem devices to harvest sunlight more efficiently and potentially achieve even higher performance.

## 2.2 Experimental details

### 2.2.1 Precursor solution preparation

Solution preparation was done inside a N2 filled drybox with oxygen and moisture levels both below 1 ppm. *Caution: hydrazine is highly toxic and should be handled with appropriate protecting equipment to prevent contact with either the vapors or liquid.* In order to prepare Cu2S solutions with controlled S/Cu2S ratios, 1 mmol of Cu2S (American Elements, 99.999%) was combined with an appropriate amount of elemental sulfur in 4 mL of hydrazine. The Cu-precursor became a transparent yellow solution after stirring for one week.

To prepare In2Se3 solutions with similarly controlled Se/In2Se3 ratios, 1 mmol of In2Se3 (American Elements, 99.999%) was combined with appropriate amounts of elemental selenium in 4 mL of hydrazine. A transparent solution was yielded after continuous stirring for several days. It is observed that In-precursor has a significantly larger viscosity compared with Cu-solution.

The CuIn(Se,S)2 precursor solutions were prepared by combining a Cu2S solution with an S/Cu2S ratio of 0.33 with an In2Se3 solution of Se/In2Se3 ratio 1 in equal proportions (Figure 2-1).  Both the Cu-/In-precursor solution and the mixed solution were stable for several months in an inert atmosphere without any observable precipitation.
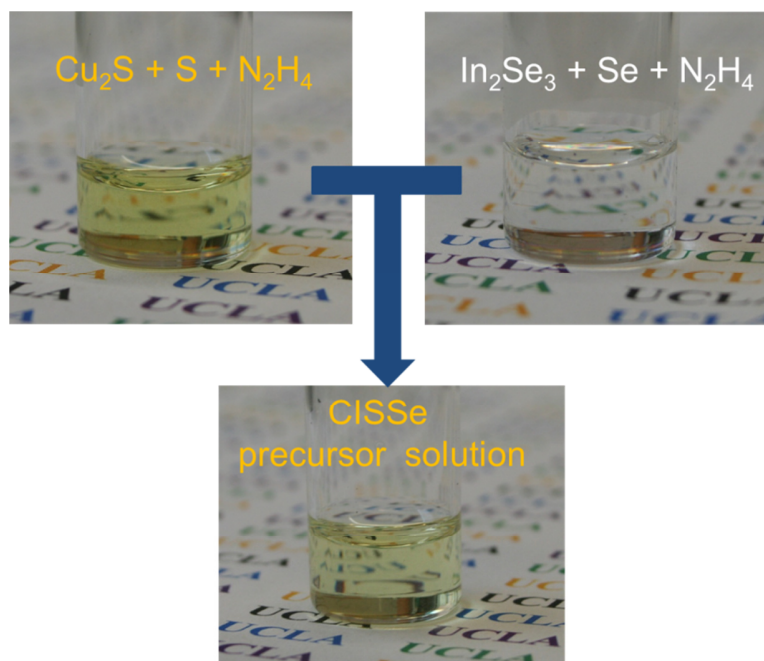
**Figure 2-1** The final CIS-precursor is formed by mixing Cu-and In-solution with the flexibility to control Cu/In ratio through the use of different volume ratios. Cu-precursor solution was prepared by combining Cu2S with excess elemental sulfur in hydrazine, yielding a transparent yellow solution. In-precursor solution was prepared by mixing 1 mmol In2Se3 with 1 mmol Se in 4 ml hydrazine, yielding a viscous transparent solution.
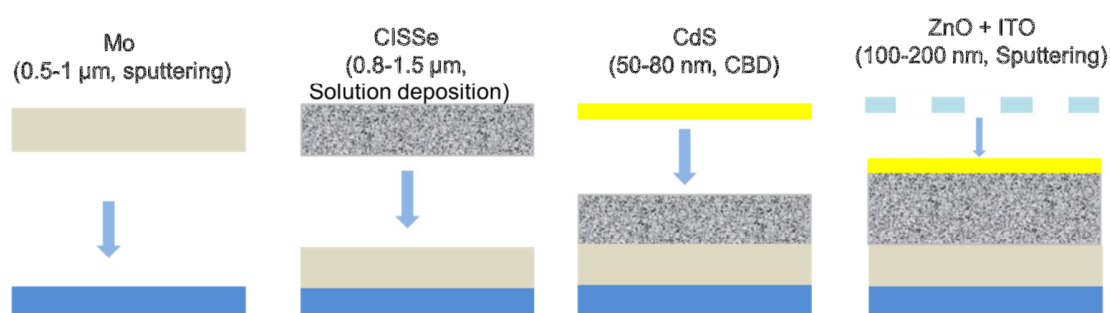


**Figure 2- 2** Device fabrication process for CISS solar cells with the structure of ITO(~100 nm)/ZnO(~20 nm)/CdS(50-80 nm)/CISS(1-2 µm)/Mo(0.5-1 µm)/Soda lime glass substrate.

### 2.2.2 Device Fabrication and characterization

A schematic flow diagram to fabricate CISS solar cells is shown in Figure 2-2. The p-type CISS layer was deposited by spin coating inside a glove box onto Mo-coated soda lime glass substrates. To reach the targeted thickness of the CISS absorption layer, several layers of CISS were deposited onto the substrates and annealed at 290 $^{o}$C alternatively before a final thermal treatment at 390 $^{o}$C. The following n-type cadmium sulfide (CdS) layer, 50-80 nm, was deposited through chemical bath deposition, followed by RF-sputtered 30 nm intrinsic zinc oxide (ZnO) and 80-120 nm indium tin oxide (ITO). In transparent devices, the Mo-contact is replaced with a transparent conducting oxide, normally ITO.

XRD patterns were collected on a PANalytical X'Pert Pro X-ray Powder Diffractometer using Cu-Kα radiation (λ=1.54060 Å). Raman-shift Spectroscopy was performed on a Renishaw inVia Raman Microscope using a 514 nm probe laser. Optical absorption measurement of CISS thin film from mixed precursors was carried out on Hitachi 4100 Spectrophotometer. The photovoltaic performance of devices was characterized in air without encapsulation under AM1.5G testing conditions using a Newport Oriel 92192 Solar Simulator. Incident Photo Conversion Efficiency (IPCE) was measured on a system designed by Enli Tech.

### 2.3 Solution chemistry in CIS precursor solutions

The molecular structure has been identified for several compounds, revealing the dissolution pathway produced by the action of hydrazine on certain metal chalcogenides.

For example, the $SnS_2$ solution has been found to contain anionic dimers of edge-sharing SnS4 tetrahedra $[Sn_2S_6]^{4-}$ alternating with hydrazinium cations $N_2H_5^+$.[2-14] The crystal isolated from Cu-solution has a 2-D Cu-S layered structure separated by $N_2H_5^+$ spacers.[2-18] However, the structure derived from dried crystals may not necessarily represent the molecular species present in solution. In addition, in some cases it is difficult to obtain the crystalline molecular structure in order to understand the dissolution process. For the In-precursor, the solid product exists in an amorphous status. Raman analysis on molecular vibrations present in solution would provide a direct observation method to probe the solution-phase structural evolution. In this section, solution-phase Raman analysis on both the Cu-solution and In-solution reveals the molecular status in solution.

Figure 2-3 shows the Raman spectrum of a 0.25M $Cu_2S$ precursor solution in which the S/Cu2S molar ratio has been adjusted to 2. Two distinct Raman shift peaks are visible at 335 and 2560 $cm^{-1}$, respectively. The peak located at 335 $cm^{-1}$ associated with the Cu-S bond of $Cu_xS_y$ species dissolved in hydrazine,[2-19] while the peak at 2560 $cm^{-1}$ is the S-H stretching mode of $(N_2H_5)_2S$ [2-20]molecules formed by the elemental sulfur present in the solution. The S-H signal indicates that excess sulfur (the portion that does not incorporate into Cu-S molecular complexes) introduced in the precursor is partially incorporated into solution bonded to H-atoms in the form of $H_2S$ or $(N_2H_5)_2S$ molecules. Thus, it is most probable that the elemental sulfur in solution has formed $(N_2H_5)_2S$ molecules according to the following chemical reaction :

$$2S + 5 N_2H_4 \rightarrow 2 (N_2H_5)_2S + N_2 \qquad (2.1)$$
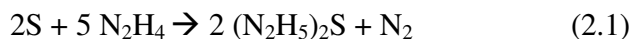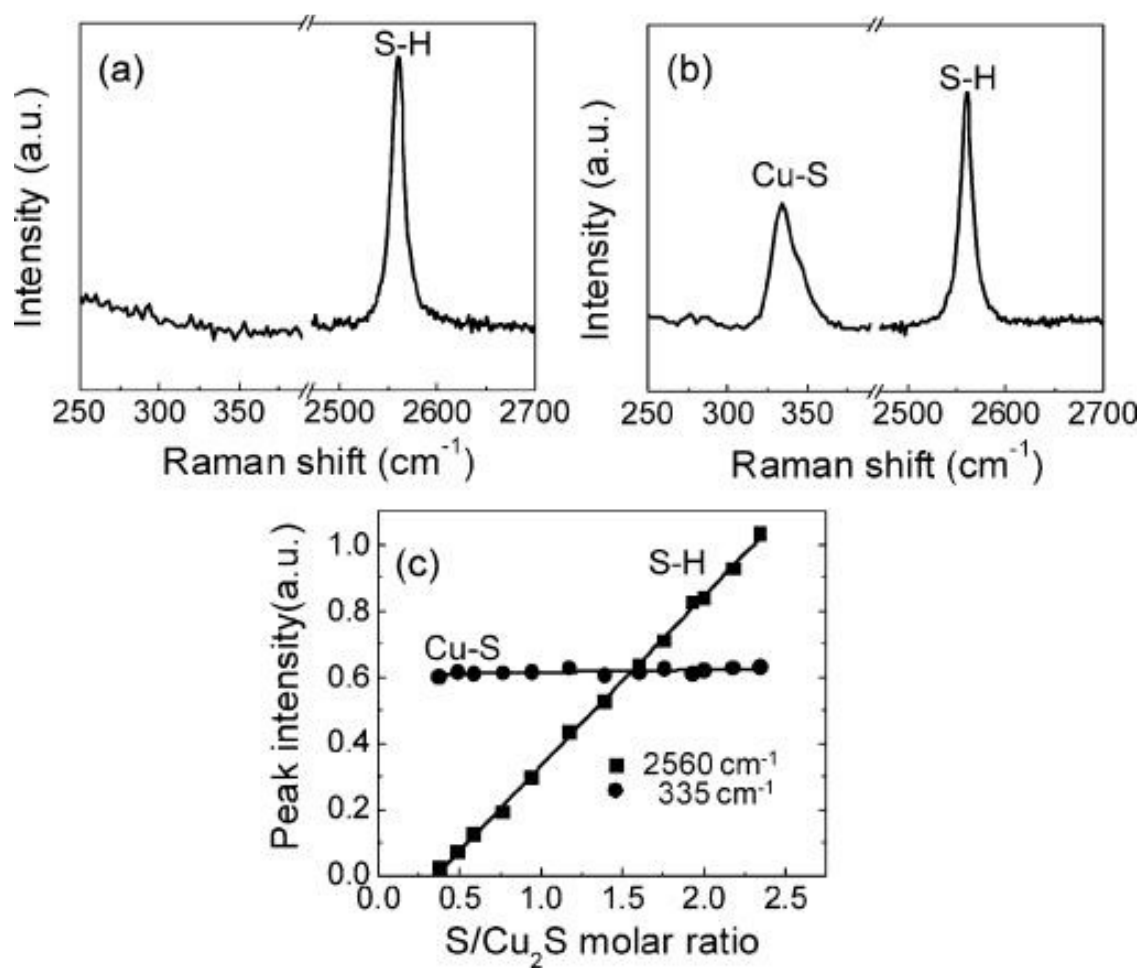
**Figure 2-3** Raman spectra of (a) the 0.5 M sulfur solution and (b) the 0.25 M $Cu_2S$ precursor solution having an $S/Cu_2S$ ratio of 2. (c) The integrated intensities of the peaks located at 335 and at 2560 $cm^{-1}$ as a function of $S/Cu_2S$ ratio obtained from the 0.25M $Cu_2S$ precursor solutions.

To investigate the stoichiometry of the $Cu_xS_y$ complex in hydrazine solution, the relative intensities between the S-H and Cu-S vibration peak as a function of S/ $Cu_2S$ molecular ratios was investigated. Figure 2-2c shows the intensities of the Cu-S and S-H peaks as a function of the S/$Cu_2S$ molecular ratio. The concentration of $Cu_2S$ was fixed to be 0.25 M, while the concentration of elemental sulfur was varied in order to adjust the S/ $Cu_2S$ ratio in the solutions. The intensity of the Cu-S peak remained constant versus the S/$Cu_2S$ ratio, indicating that the $Cu_2S$ powder was fully dissolved in each sample. In contrast, the intensity of the S-H peak increased linearly with the S/ $Cu_2S$ ratio and can be traced back to its x-intercept at an S/$Cu_2S$ value of approximately 0.33. At S/ $Cu_2S$ values smaller than 0.33, we observed black precipitates in the solution, which are presumably undissolved $Cu_2S$. From this information, we propose that $[Cu_6S_4]^{2-}$ ions are formed by the following overall chemical reaction in hydrazine:

$$6Cu_2S + 2S + 5\,N_2H_4 \rightarrow 2[Cu_6S_4]^{2-} + 4\,N_2H_5^+ + N_2 \qquad (2.2)$$
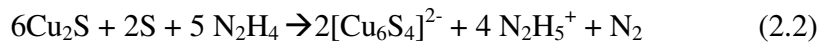
In an analogous analysis approach, the molecular status in $In_2Se_3$ precursor solution is explored. Unlike sulfur dissolving in hydrazine and forming S-H bonds, selenium dissolved in hydrazine exists in the form of Se-rings, with the Raman vibration mode at 260 cm$^{-1}$.[2-21] The Se-clusters have absorption in visible range, so giving the resulting solution a green color.[2-22] Raman spectra for In-solution show an obvious peak at 192 cm$^{-1}$ corresponding to the In-Se vibration mode.[2-23] Based on the relative intensity between the Se-ring vibration and the In-Se mode, we can calculate the maximum ratio between In/Se in the In-solution to be approximately 2/4. As shown in **Figure 2-**4, from the colorless In-solution as the starting point, we gradually introduce excess Se into the
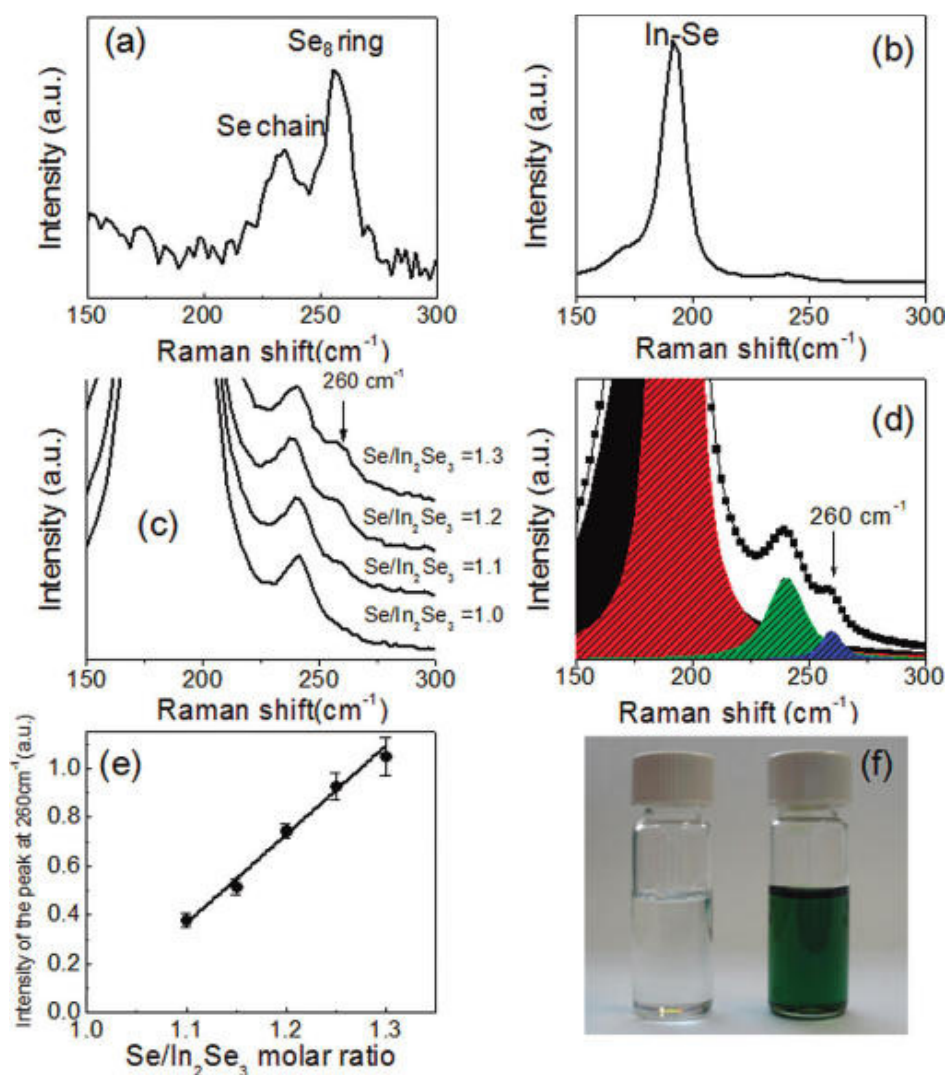
**Figure 2-4** Raman spectra of (a) the 0.1 M selenium solution, (b) the 0.25 M In$_2$Se$_3$ precursor solution with an Se/In$_2$Se$_3$ ratio of 1, and (c) several Se-rich 0.25 M In$_2$Se$_3$ precursor solutions with various Se/In$_2$Se$_3$ ratios. (d) Deconvolution of the peaks obtained from the In$_2$Se$_3$ precursor solution with an Se/In$_2$Se$_3$ ratio of 1.3. (e) The integrated intensity of the peak located at 260 cm-1 as a function of the Se/In$_2$Se$_3$ ratio in Se-rich 0.25 M Se/In$_2$Se$_3$ precursor solutions. (f) A picture of the Se/In$_2$Se$_3$ precursor solutions containing an equal molar amount of elemental selenium and In$_2$Se$_3$ (left) and with an Se/In$_2$Se$_3$ ratio of 1.1 (right). at an Se/In$_2$Se$_3$ ratio of approximately unity.

solution. The signal increases linearly with the Se/In$_2$Se$_3$ ratio and can be traced back to its x-intercept. The intercept on x-axis represents the point that all dissolved selenium is incorporated into the complex structure with no excess selenium in the form of Se-rings. Thus the following reaction route was proposed to present the overall reaction:

$$2In_2Se_3 + 2Se + 5 N_2H_4 \rightarrow 2[In_2Se_3]^{2-} + 4 N_2H_5^+ + N_2 \qquad (2.3)$$
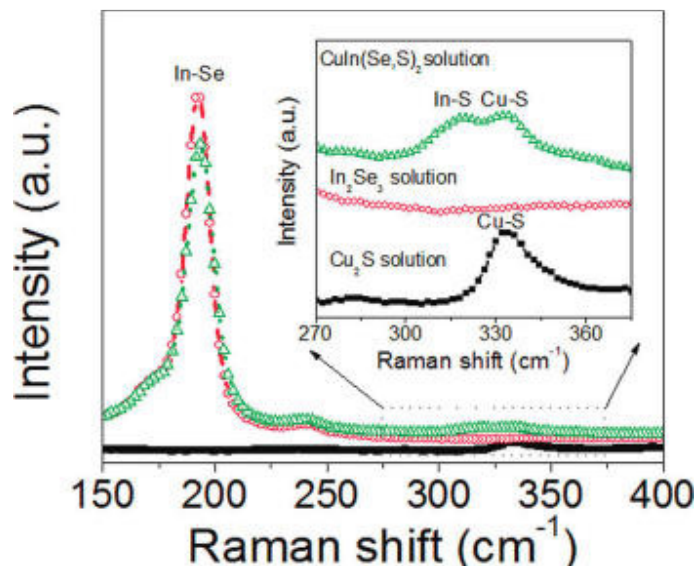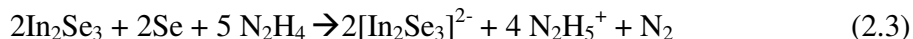


**Figure 2-5**. Raman spectra of the 0.125 M Cu$_2$S solution in which the S/ Cu$_2$S ratio is 0.33, the 0.125 M In$_2$Se$_3$ solution in which the Se/In$_2$Se$_3$ ratio is unity, and the CuIn(Se,S)$_2$ precursor solution prepared by mixing a 0.25 M Cu$_2$S solution and 0.25 M In$_2$Se$_3$ solution in equal proportion.

The mixed Cu-and In-solution produces a new vibration peak around 310 cm$^{-1}$. From the empirical calculation of Raman vibrations, and using the position of the Cu-S vibration peak, it can be ascribed to the In-S vibration.[2-24] The creation of In-S bonds in the

CuIn(Se,S)$_2$ precursor solution provides strong evidence for the mixing of copper, indium, sulfur, and selenium at a molecular level even prior to deposition. The presence of the new vibration mode and the relative reduced In-Se intensity in the mixed solutions suggest the possibility that anion exchange to a certain degree may happen between [Cu$_4$S$_6$]$^{4-}$ and [In$_2$Se$_4$]$^{4-}$.The intermixing on atomic level enables the formation of chalcopyrite phase without long range diffusion process. Without the necessity of overcoming diffusion barriers, it thus provides advantages for the low temperature deposition of CIS films. [2-17]

## 2.4  CIS Solar Cells from Hydrazine Processed Copper Selenide

### 2.4.1 Copper precursor from dissolving Cu$_2$Se

The possible exchange between S$^{2-}$ and Se$^{2-}$ inspired another strategy to process metal chalcogenides. Excess S could be incorporated into the In-Se complex forming [In(S,Se)$_4$]$^{2-}$ and allowing for finer control of the band gap of resulting CISS films. More importantly, previously insoluble precursor compounds could be processed this way. Cu$_2$Se with excess Se or In$_2$S$_3$ with excess S is found to still have limited solubility compared to their sulfide and selenide analogues.[2-22]In the following section, previously insoluble Cu$_2$Se was successfully incorporated into solution with the introduction of extra sulfur into the solution.

Copper selenide was dissolved by mixing 2 mmol Cu$_2$Se and 4 mmol S with 4 ml anhydrous hydrazine. After continuous stirring at room temperature for several days, it produced a clear dark green solution. Relating to the fact that excess selenium in

hydrazine is not able to dismantle the framework of Cu-Se into soluble molecular species, the incorporation of sulfur into the lattice likely initiates the dissolution related to an ion-exchange process. In order to analyze the evolution of the precursor, X-ray diffraction (XRD) analysis was carried out on the powder derived from precursor solution annealed at 200 $^{o}$C under an inert atmosphere. The x-ray diffraction spectrum of the product obtained from the $Cu_2Se$ precursor solution, as shown in **Figure 2-6,** indicates a good quality of crystalline Berzelianite (JCPDF 01-071-0044); systematic peaks of chalcogen (selenium or sulfur) were not observed. The larger 2θ value compared to the standard Berzelianite related to a smaller d-spacing of lattice in the crystalline product, indicating that sulfur was partially incorporated into the copper-selenide lattice. The coexistent CuSe phase, according to the equilibrium phase diagram of Cu-Se system,[2-25] suggests that the product derived from soluble species had a chalcogen-rich composition compared to stoichiometric $Cu_2Se$. Compared with chalcocite (JCPDF 33-0490) produced by heating the $Cu_2S$ precursor solution, powder produced from the $Cu_2Se$ solution shows a totally different lattice diffraction pattern when heat treated at the same temperature (**Figure 2-6 (b)**). It is thus indicated that in the process to dissolve $Cu_2Se$ into hydrazine solvent, extra sulfur was incorporated into Cu-Se system, but did not completely replace the occupancy of selenium.
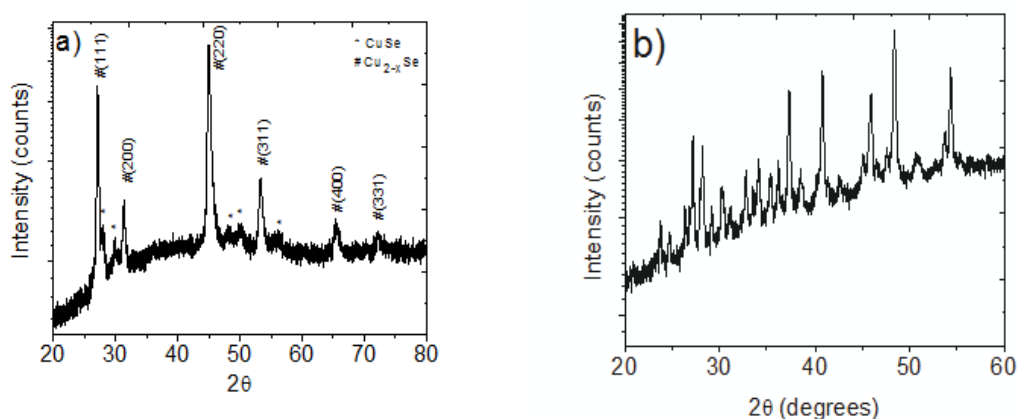
**Figure 2-6** Powder X-ray diffraction of a) product from {Cu$_2$Se, S, hydrazine} solution, identified as Berzelianite Cu$_2$Se (JCPDF 01-071-0044) b) product from {Cu$_2$S, S-hydrazine}, as chalcocite Cu$_2$S (JCPDF 33-0490) Sample powder was prepared by evaporating the related solution in an inert atmosphere at 200 $^\circ$C.
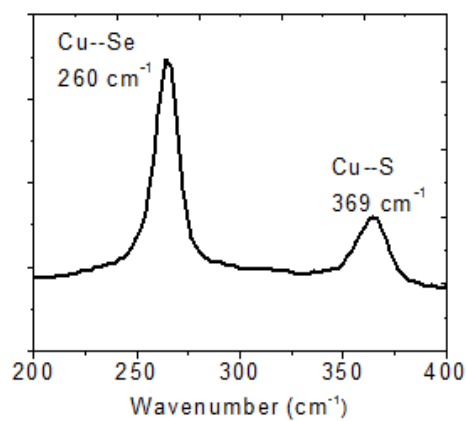


**Figure 2- 7** Raman spectroscopy of Cu$_2$Se powder derived from the Cu$_2$Se, S, hydrazine precursor solution at 200 $^\circ$C in an inert environment.

To verify the incorporation of sulfur during the process to form the $Cu_2Se$ precursor solution, Raman spectroscopy was utilized to detect the bonding status of the molecular species. Samples were prepared with annealing temperatures not beyond 100 $^{o}$C in a glove box to evaporate excess solvent while preventing the variation of molecular species via the sublimation of S or Se from the precursor. Then it was encapsulated between glass slides for Raman analysis to avoid possible oxidation and other reactions when contacting air.[2-24] As shown in **Figure 2-7**, the main peak at 260 cm$^{-1}$ relates to the vibration frequency of Cu-Se bonds; the peak at 369 cm$^{-1}$ corresponds to the Cu-S bond vibration. This Raman analysis verifies the existence of Cu-S bonds in the soluble molecular species from the $Cu_2Se$, S, hydrazine solution system, which is in agreement with the 2θ shift in the XRD diffraction spectra. Partial substitution with extra sulfur appears to play a unique role in dismantling the framework of copper selenide. The incorporation of sulfur into copper selenide terminated Cu-Se-Cu bridges, reduces the connectedness and dimensionality of the Cu-Se framework. The consequent discrete metal chalcogenide units obtained through the dissolution process can then be dissolved and stabilized by the system of hydrazine with extra chalcogen ligands.[2-12] As for the stability issues of as-prepared $Cu_2Se$ solutions, the copper selenide solution system was stable for several weeks in an inert atmosphere, compared to the precipitation of $Cu_2Te$ in few hours[2-11]. The precise functions of each chalcogen atom that are together able to dissolve and stabilize normally insoluble metal chalcogenides remains to be investigated.

### 2.4.2 CISS film and devices using $Cu_2Se$ precursor

In order to examine the effects of mixed chalcogenides in a given precursor solution, three types of CISS were formed using Cu2(S,Se) and In2Se3 and dissolved in a

prescribed ratio of excess sulfur or selenium. The Type I CISS powder sample for XRD was formed by annealing the mixed precursor solution produced from the copper selenide and indium selenide precursors, using the same annealing recipe for the CISS absorber layer in device. Type II CISS powder was prepared similarly except using $Cu_2S$ as a copper precursor rather than $Cu_2Se$. The XRD pattern is shown in **Figure 2-8 (a),** indicating the high quality crystallization of the chalcopyrite phase from the original precursor solutions. It also indicates that the ordered defect compound (ODC) $CuIn_3Se_5$ coexists with the chalcopyrite $CuInSe_2$ phase, as the asterisk marked peaks indicate besides the CISS main peaks of (112), (220/204) and (316/332). Other than that, no obvious impurity or secondary phase appeared in XRD pattern. The ODC phase, derived from $CuInSe_2$ with an ordered array of defect pairs ($2V_{Cu}^- + In_{Cu}^{2+}$), can be formed from a highly copper-poor stoichiometry in the pseudo-binary phase diagram of Cu2Se–In2Se3.[2-26]

Compared with the main CISS diffraction peak of (112), as shown in **Figure 2-8 (b)**, Type I chalcopyrite exhibits a smaller $2\theta$ value, which indicates that less sulfur was incorporated into the final CISS product. Excess sulfur could be evaporated during the final heat treatment of the $Cu_2S$ precursor solution;[2-17] even less sulfur was incorporated into final product using other chalcogen (e.g. Te) to replace it.[2-11] Without varying the Se/S ratio intentionally by adding extra chalcogen, type I CISS demonstrated a relatively higher Se/S ratio. By employing $Cu_2Se$ rather than $Cu_2S$ as Cu precursor, more selenium has been incorporated into the final chalcopyrite product without adding extra selenium or employing post-deposition selenization procedures.
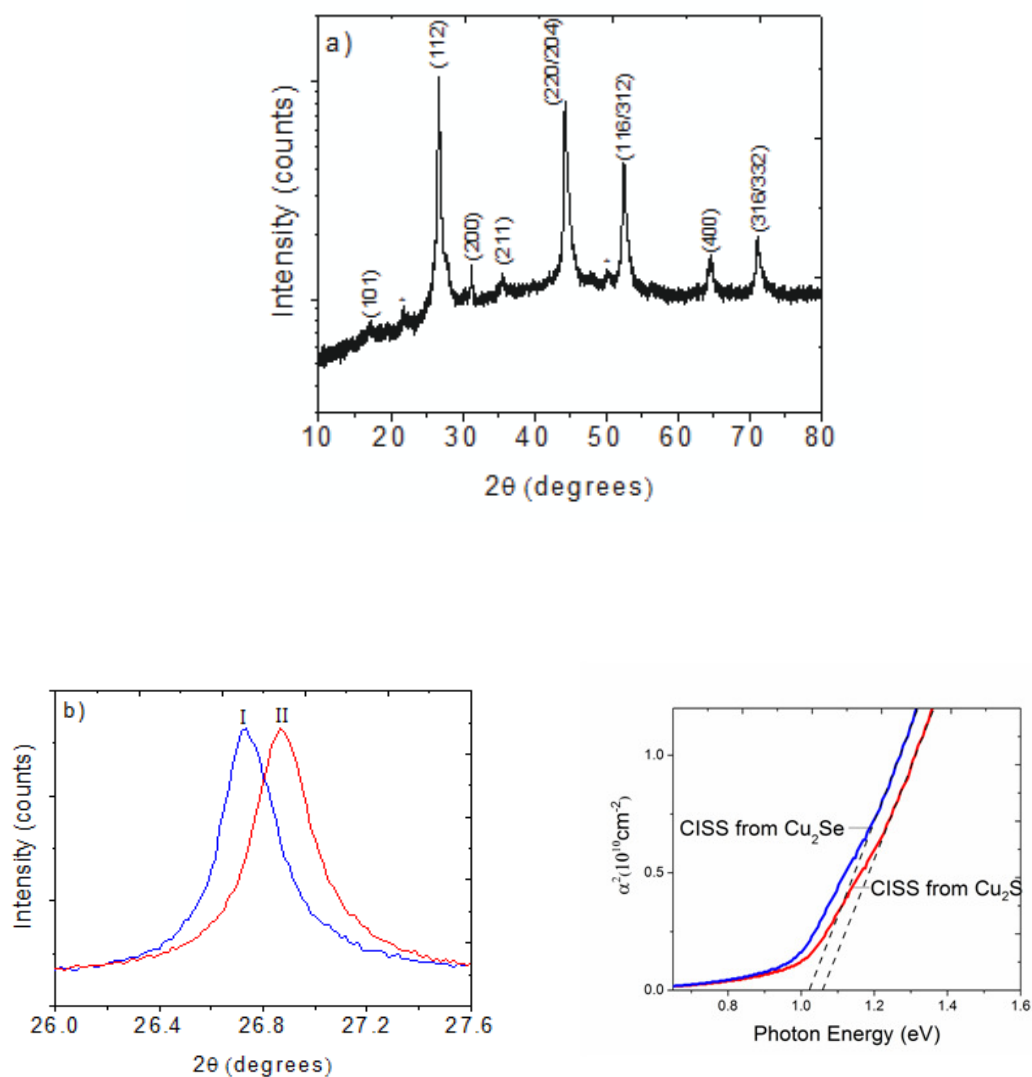
**Figure 2-8** a) X-ray diffraction of CISS powder from $Cu_2Se$ and $In_2Se_3$ precursor, b) (112) X-ray peak of CISS produced from type I solution (In-precursor and Cu-precursor of $Cu_2Se$) and type II solution (In-precursor and Cu-precursor of $Cu_2S$). The peak intensity was normalized to facilitate comparison between samples. c) Absorption of CISS film prepared from type I and type II solution on glass substrate. The Cu/In ratio was kept the same by mixing the same ratio of Cu-precursor and In-precursor.

Optical absorption of the chalcopyrite film on glass also verifies the difference in Se/S ratio. **Figure 2-8(c)** shows the absorption spectra of type I and type II films from $Cu_2Se$ and $Cu_2S$, respectively. It can be seen that the absorption edge shifts to lower photon energy for CISS films deposited using $Cu_2Se$ precursor solutions. The smaller band gap indicates that more selenium was incorporated into the final film, corresponding well with XRD analysis. The estimated bandgaps of type I and type II were approximately 1.05 eV and 1.08 eV, which agrees with the reported value.[2-9] In indium-rich CIS, the coexistence of $CuInSe_2$ and ordered vacancy compound $CuIn_3Se_5$ results in composition fluctuations manifested as strong band-tailing in their combined optical absorption.[2-26] The phenomenon is a consequence of the native defect structure of these materials, and not an artifact of polycrystallinity, preparation.[2-26,2-27] The band gap can also be seen from the cut off wavelength around 1250 nm in IPCE measurement of the final device, which will be discussed in detail later. Band gap engineering toward larger values has been realized by incorporating gallium or excess sulfur into the final product.[2-9,2-28] Toward lower values, however, the smallest band gap from hydrazine solution process is higher than that achieved using other deposition methods, since a small amount of S always exists in the film.[2-7,2-17,2-29] By employing the newly soluble $Cu_2Se$ as the Cu precursor, the lower limit for the band gap in the hydrazine processed CIGSS system can be further reduced. This strategy can potentially be employed to increase the tunability of the optical properties in $Cu_2ZnSn(S,Se)_4$ materials as well. Smaller band gap CZTS with a Se-rich composition was found to show beneficial defects properties and thus higher conversion efficiencies compared to its sulfur-rich counterpart.[2-30,2-31] The realization of soluble Cu-Se building blocks in CISS precursor

31
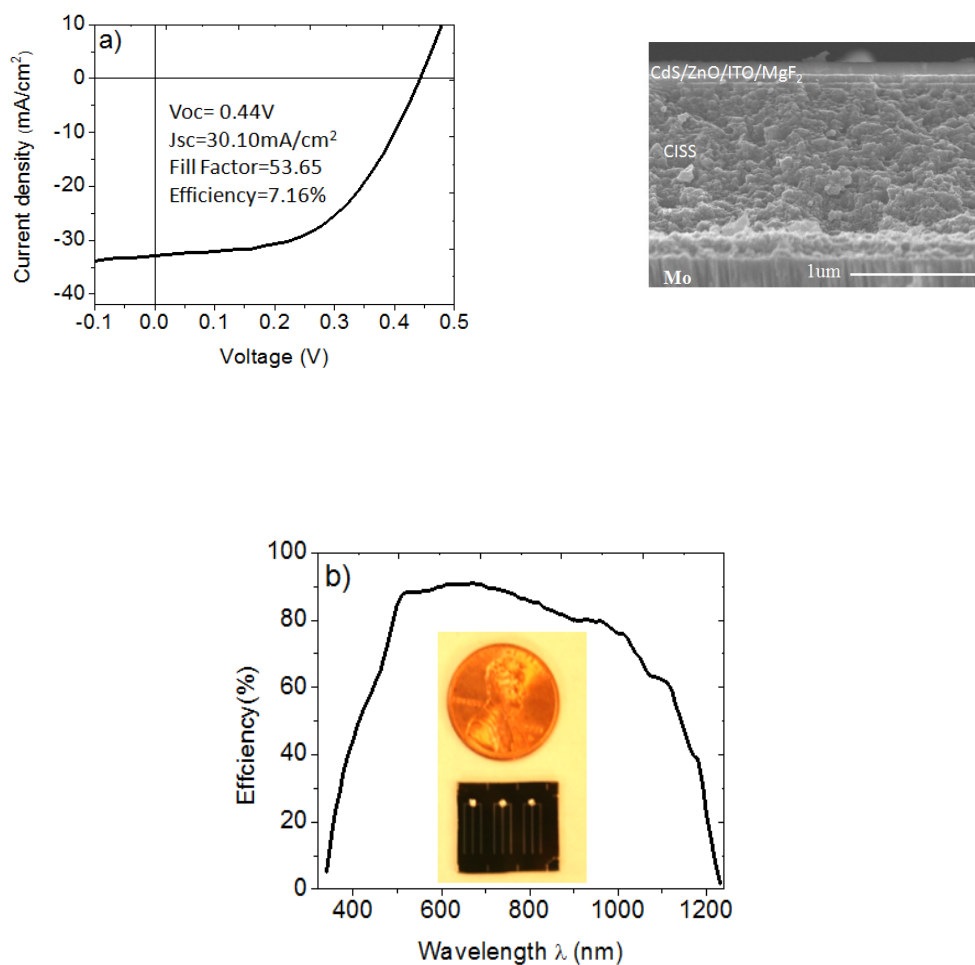
**Figure 2-9** a) I-V characterization of CISS photovoltaic device from precursor solutions containing $Cu_2Se$ and $In_2Se_3$, under AM1.5G simulated light. b) Incident photon conversion efficiency (IPCE) characterization of the CISS device fabricated from $Cu_2Se$ precursors. Image of a completed CISS device and SEM cross sectional image are listed as reference. The top layer with smooth morphology was an antireflection coating of $MgF_2$, the layers with small column grains are ITO/ZnO/CdS respectively.

solutions thus provides an opportunity to explore selenium-rich multinary compound and likely achieve desirable device performance.

The first demonstration of CISS solar cell based on $Cu_2Se$ precursors was fabricated using temperatures not in excess of $400^oC$. The inset of **Figure 2-9b** shows the completed device with finger area of $0.5$ $cm^2$. Cross sectional SEM image of a CISS device from the new Cu-precursor was taken and shown in **Figure 2-9c**. The absorber film is composed with small grains below 100 nm, producing scattering centers which likely impeded carrier collection. Under AM1.5G condition, the initial CISS device fabricated using the $Cu_2Se$ precursor demonstrated a power conversion efficiency of 7.16%. It yielded short circuit current ($J_{sc}$), open circuit voltage ($V_{oc}$), and Fill Factor (FF) values of $30.10mA/cm^2$, 0.44V, and 53.65% respectively. To verify the short circuit current, incident photon conversion efficiency (IPCE) was carried out. The integration of IPCE data over the wavelength led to a higher short circuit current ($J_{sc}$) exceeding 35.0 $mA/cm^2$. IPCE results showed an effective utilization of the solar spectrum in the IR range, with values beyond 60% even at wavelengths around 1100nm.

## 2.5 Semi-transparent CISS devices

For single junction, photons with energy greater than the band gap are partially dissipated into thermal energy, leading to a chemical potential loss or open circuit voltage loss in the device. Photons with less energy than band gap are not able to contribute to photocurrent. The trade-off between $V_{oc}$ and $J_{sc}$ determines the optimized band gap at 1.5 eV to best utilize the solar spectrum.[2-32] To harvest the spectrum more efficiently, it is necessary to split the solar spectrum, that is to selectively absorb photons with different energies.

Tandem cells with different band gap absorbers stacked together provide a practical model to realize the improvement.[2-33] A wider band gap material on top filters high energy photon to generate a higher voltage, while less energetic photons pass through to smaller band gap materials while still contributing to photocurrent. The $Cu(In,Ga)(Se,S)_2$ material system can be tuned over a band gap range from 1.04 eV to beyond 2 eV.[2-26] To achieve the tandem structure, it is a prerequisite to have a transparent top cell. In the following, transparent CIS devices will be explored. The transparent CIS device replaces the traditional Mo-contact with an ITO contact. The typical device structure is shown in **Figure 2-10.** Devices constructed on top of transparent substrates have the same configuration and similar processing procedures to those of previously discussed CIS devices.
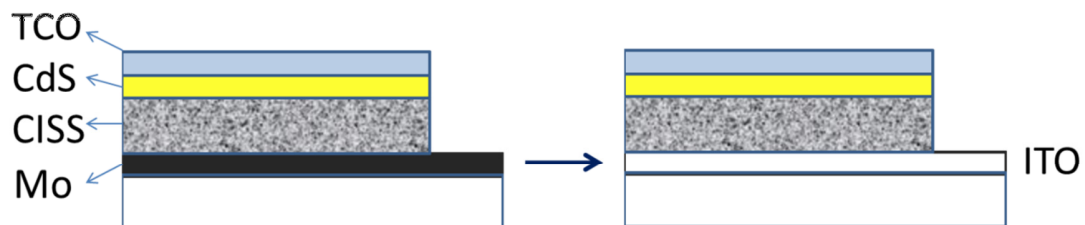


**Figure 2-10** Device structure for transparent CIS solar cells.

**Figure 2-11** shows the I-V characteristics for transparent CIS solar cells. Compared with Mo-back contact devices, almost every parameter in ITO based devices shows somewhat reduced values. The intuitive source of efficiency loss lies at the interface of the absorber layer and back contact. It is well known that Mo provides a good contact with CIS due to its relatively large work function. In high temperature processed devices, the formation of a $MoS_2$ or $MoSe_2$ interfacial layer even contributes to forming an ohmic contact for improved carrier injection and transport.[2-34] The high series resistance in transparent devices indicates that the contact between ITO and CIS likely introduces a significant Schottky barrier.

Another major difference is the reverse saturation current $I_o$, with a difference of 3-4 orders of magnitude compared to the Mo-based device. $I_o$, determined in part by the minority carrier life time or diffusion length, represents the severity of recombination processes in the device.[2-33] It is heavily influenced by the passivating effects of sodium in the CIS absorber layer.[2-35] Sputtered Mo has a columnar-morphology that allows for the vertical diffusion along grain boundaries from the soda lime glass substrate into the absorber material. ITO has a dense morphology which might limit the amount of sodium that is able to diffuse through to the CISS layer and assist with forming a high quality absorber material.

**Figure 2-11** IV characteristics for transparent CISS device using ITO and Mo back contact.
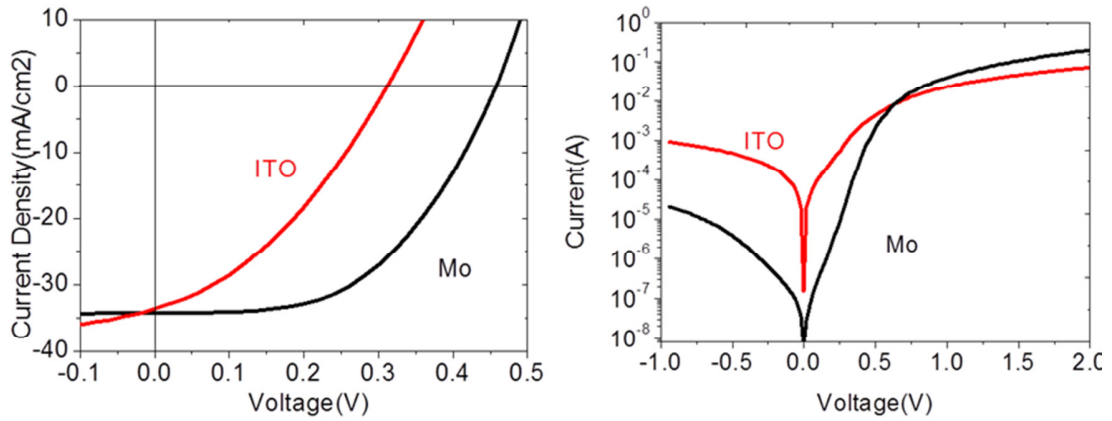


Table 2- 1. Device parameters comparison between CISS device using ITO back contact, modified contact, and conventional Mo-back contact.

| | $R_s(\Omega)$ | $R_{sh}(\Omega)$ | n | $I_0$ (A) | Jsc (mA/cm2) | Voc (V) | FF (%) | $\eta$ (%) |
|---|---|---|---|---|---|---|---|---|
| **Mo/substrate** | 30.0 | $1.61\times10^5$ | 1.44 | $9.85\times10^{-9}$ | 34.3 | 0.46 | 51.7 | **8.12** |
| **ITO/ substrate** | 45.1 | $1.05\times10^3$ | 3.42 | $3.40\times10^{-5}$ | 33.6 | 0.31 | 35.7 | **3.75** |
| **Mo/ITO/Substrate** | 46.4 | $3.74\times10^4$ | 1.90 | $1.49\times10^{-6}$ | 33.3 | 0.39 | 32.7 | **4.2** |

A thin layer of Mo (5-30 nm) was deposited on ITO to provide Ohmic contact. It was observed that the $V_{oc}$ increased from 0.31 to 0.39 V after introducing the Mo contact layer. The modification of the back contact in this way is effective in improving device performance, and its substantial effect on $R_{shunt}$ indicates that ITO produces unfavorable shunt pathways through the junction when used alone. In the fabrication of transparent top cell for tandem device usage, a discontinuous layer of Mo such as nano-patterned meshes would improve light transmission to the bottom cell while still providing favorable contact properties to the CIS layer.

## 2.6 Sodium effect on CISS material properties

Optimized sodium incorporation was found to be beneficial to CIS device performance as soda-lim glass was chosen as substrates. Electronically, the beneficial effects may be primarily summed from: increased p-type conductivity and grain boundary passivation on CIS absorber layer.[2-35 to 2-37] Mechanisms that have been proposed to explain the enhancement of conductivity include the substitution of Na for In generating $Na_{In}$ antisite defect acceptors in the lattice, and energetically favorable $Na_{Cu}$ defect reducing the compensating $In_{Cu}$ antisite defect.[2-26] Several known methods of sodium introduction into CIS thin films include: prior evaporation of a sodium compound precursor layer before CIS deposition, and post deposition of sodium source which is then thermally diffused into the CIS layer.[2-38 to 2-40] However, these methods of Na incorporation, typically employed in evaporation based routes, lead to more complicated fabrication procedures. The solution-phase molecular precursor system discussed here provides a

perfect platform to introduce extrinsic dopants to tune material properties. In the present work, we report an elegant approach for Na incorporation through precursor solution. Compared with others, this approach provide provides striking advantages: (i) simple processing without involving additional evaporation or annealing procedures (ii) precise control of the amount of dopants compared with diffusing sodium from SLG substrates or (iii) without introducing anionic impurities as with the evaporation of NaF.

### 2.6.1 Sodium solution preparation

The most intuitive method is to dissolve metallic Na into hydrazine to form a molecularly dispersed solution. Hydrazine was observed to react violently upon contact with small amount of sodium, indicated by fuming followed by vigorous bubbling. Finally, a colorless Na-hydrazine solution could be obtained. *Caution: Large quantities of sodium are apparently able to induce an explosive reaction with hydrazine even in an inert glove box with moisture and water level well controlled below 0.1 ppm.* To avoid the danger of explosion, the alternative approach is to employ sodium chalcogenide. Since the initial status of sodium is as sodium ion, this strategy circumvents the violent redox reaction with hydrazine.

The sodium solution was prepared by placing 1 mmol of $Na_2Se$ in a screw cap glass vial. 0.5 mL of hydrazine ($N_2H_4$) solution was then added drop-wise with a micropipette to the vial containing the sodium. Adding excess selenium was found to increase the solubility of $Na_2Se$. An interesting color change was observed for the $Na_2Se$ solution, from pink without excess selenium to red and dark red as the amount of excess selenium gradually increased. Precursor solutions with Na-dopant were then prepared by mixing the CIS and Na-solutions in various ratios from 0.01 to 1 atomic % sodium.

## 2.6.2 The effects of Sodium in CIS devices

XPS was used to analyze the CIS films extra sodium additives. Two kinds of samples were prepared for characterization: Type I are CIS films on ITO-coated glass substrate, type II are CIS films on ITO-glass with excess Na incorporated in the precursor solution. Sodium tends to segregate on the surface as surface analysis indicates in **Figure 2-12.** The sample made from the Na-containing CIS precursor shows much higher sodium levels accumulated on surface. The high-resolution scan in **Figure 2-12** shows the relative ratio between Na and main element of Cu on surface.

To probe the bulk films, $Ar^+$ ion (1000 KeV) was used to etch the CIS surface. The amount of sodium incorporated inside the films was significantly smaller than that present on the surface. For CIS films without extra induced sodium, sodium is below the detection limit (0.1 atomic %). Using Na-containing precursor solution, small but noticeable amounts of sodium were detected. The effective concentration of sodium in the CIS film is able to produce electronic benefits in the resulting devices. Considering the limited solubility of Na in chalcopyrite lattices, it is thus reasonable to conclude that sodium mainly accumulates at grain boundaries. Due to the fine grain structure, the relatively large number of grain boundaries are able to accommodate a substantial amount of sodium, as indicated in **Figure 2-12.** The accumulation of sodium at grain boundaries effectively passivates electronically active defects. With excess sodium incorporated into the CISS film, device performance improved, mainly in the form of enhanced fill factor. From dark I-V characterization, the reverse bias current was reduced around 1-2 orders of magnitude. The reverse saturation current $I_o$ indicates that the recombination was effectively reduced with extra sodium incorporated.
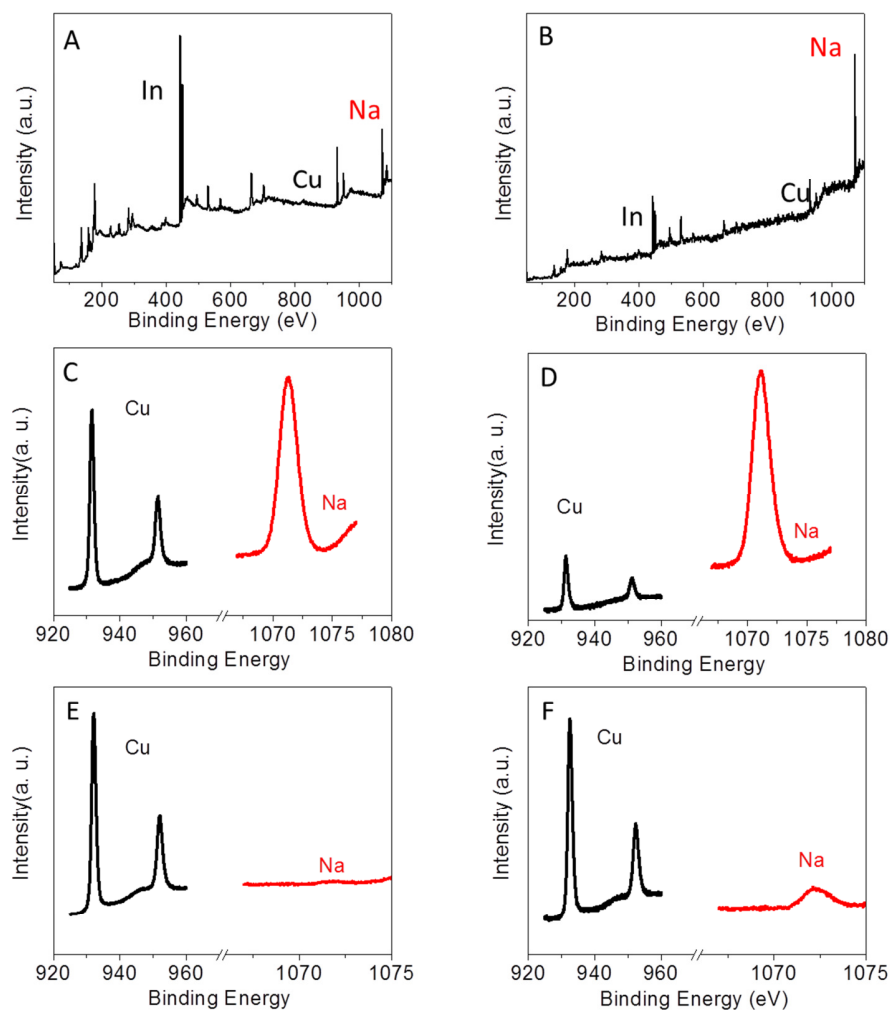
**Figure 2-12** X-ray photoelectron spectroscopy (XPS) analysis on solution deposited CIS films after heat treatment at 400 °C. Fast scan on the surface of the CIS film a) without and b) with extra sodium introduced into the precursor solution. High resolution scan of the Cu and Na signal on the CIS surface c) without and d) with extra sodium introduced. High resolution scan for Cu and Na signal inside the CIS film e) without and f) with extra sodium introduced. To probe the composition in bulk film, $Ar^+$(3 keV) etching was applied on CIS samples.

**Figure 2-13** I-V characteristics for CIS devices modified by extrinsic sodium, compared with a control device without extra Na introduced.
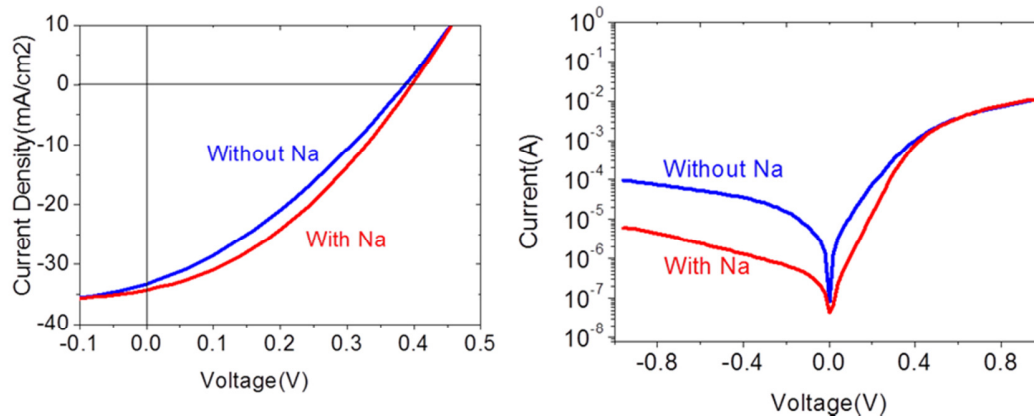


Table 2- 2. CISS device parameters comparison for film with/without sodium modified.

| Structure | $V_{oc}$ (V) | $J_{sc}$(mA/cm$^2$) | H (%) | FF (%) | $R_s$ ($\Omega$) | $R_{sh}$ ($\Omega$) | n | $I_0$ (A) |
|---|---|---|---|---|---|---|---|---|
| TCO/CIS Mo/ITO/glass | 0.39 | 33.27 | 4.20 | 32.67 | 46.35 | $3.74 \times 10^4$ | 1.90 | $1.49 \times 10^{-6}$ |
| TCO/CIS:Na/ Mo/ITO/glass | 0.40 | 34.30 | 4.94 | 36.23 | 62.77 | $1.10 \times 10^6$ | 1.53 | $\mathbf{8.07 \times 10^{-8}}$ |

**2.7 Summary**

In this chapter, a systematic study was performed on hydrazine-based solution processed CIS solar cells. First from the precursor solution, Raman studies on the precursor solution reveals the molecular structures of soluble precursors. By probing the structural evolution in precursor solution, the dissolution mechanisms are proposed. The removal of long range diffusion by intermixing on the atomic level between the Cu and In precursor complexes also provides an explanation for the success of low temperature processing by this molecular solution approach.

The identification of the interaction between precursor molecules also allowed for the successful dissolution of selenide based copper precursors. The newly dissolved Cu2Se has enlarged the family of metal chalcogenides that hydrazine can process directly from solution. The chalcopyrite product deposited using $Cu_2Se$ and $In_2Se_3$ precursors exhibited less sulfur content than that deposited using $Cu_2S$, which extended the lower limitation of the band gap acquired by hydrazine processing. The effective current generation even at IR wavelengths provides a promising bottom cell to fabricate chalcopyrite-based tandem cells.

Finally transparent device structures were exploited by replacing Mo with the transparent conducting oxide ITO. The contact between the CISS absorber layer and electrode is vital to maintaining comparable device performance with Mo-based devices. Sodium incorporation is also a critical strategy to achieve high quality CIS films and passivating the many intrinsic defects formed at grain boundaries. A simple approach to introduce Na-sources into molecular solution offered a route to control the quantity of incorporated

sodium. This method makes the use of sodium independent from diffusion out of substrate, and as a result provides a universal route for CISS device fabrication on rigid, flexible, and non-sodium containing substrates.

Reference

[2-1]    P. Jackson, D. Hariskos, E. Lotter, S. Paetel, R. Wuerz, R. Menner, W. Wischmann, M. Powalla, *Progress in Photovoltaics: Research and Applications* **2011**, *19*, 894–897.

[2-2]    I. Repins, M. A. Contreras, B. Egaas, C. DeHart, J. Scharf, C. L. Perkins, B. To, R. Noufi, *Progress in Photovoltaics: Research and Applications* **2008**, *16*, 235–239.

[2-3]    M. A. Green, K. Emery, Y. Hishikawa, W. Warta, E. D. Dunlop, *Progress in Photovoltaics: Research and Applications* **2012**, *20*, 12–20.

[2-4]    H. Sugimoto, H. Hiroi, N. Sakai, S. Muraoka, T. Katou, S. F. K. K, **2011**, *4*, 2997–3000.

[2-5]    "First Solar Achieves 5GW Photovoltaic Production Milestone (NASDAQ:FSLR)," can be found under http://investor.firstsolar.com/releasedetail.cfm?releaseid=624675, **n.d.**

[2-6]    C. J. Hibberd, E. Chassaing, W. Liu, D. B. Mitzi, D. Lincot, A. N. Tiwari, **2009**, DOI 10.1002/pip.

[2-7]    D. B. Mitzi, M. Yuan, W. Liu, A. J. Kellock, S. J. Chey, V. Deline, A. G. Schrott, *Advanced Materials* **2008**, *20*, 3657–3662.

[2-8]    N. G. Dhere, *Solar Energy Materials and Solar Cells* **2006**, *90*, 2181–2190.

[2-9]    D. B. Mitzi, M. Yuan, W. Liu, A. J. Kellock, S. J. Chey, L. Gignac, A. G. Schrott, *Thin Solid Films* **2009**, *517*, 2158–2162.

[2-10]  T. K. Todorov, O. Gunawan, T. Gokmen, D. B. Mitzi, *Progress in Photovoltaics: Research and Applications* **2012**, *21*, 82–87.

[2-11]  D. B. Mitzi, M. Copel, C. E. Murray, *Advanced Materials* **2006**, *18*, 2448–2452.

[2-12]  M. Yuan, D. B. Mitzi, *Dalton transactions (Cambridge, England : 2003)* **2009**, 6078–88.

[2-13]  D. B. Mitzi, *Advanced Materials* **2009**, *21*, 3141–3158.

[2-14]  D. B. Mitzi, L. L. Kosbar, C. E. Murray, M. Copel, A. Afzali, *Nature* **2004**, *428*, 299–303.

[2-15]  D. B. Mitzi, *Inorganic chemistry* **2005**, *44*, 7078–86.

[2-16]  D. J. Milliron, S. Raoux, R. M. Shelby, J. Jordan-Sweet, *Nature materials* **2007**, *6*, 352–6.

[2-17]  W. W. Hou, B. Bob, S. Li, Y. Yang, *Thin Solid Films* **2009**, *517*, 6853–6856.

[2-18]  D. B. Mitzi, *Inorganic chemistry* **2007**, *46*, 926–31.

[2-19]  C. R. Andrew, H. Yeom, J. S. Valentine, B. G. Karlsson, G. van Pouderoyen, G. W. Canters, T. M. Loehr, J. Sanders-Loehr, N. Bonander, *Journal of the American Chemical Society* **1994**, *116*, 11489–11498.

[2-20]  S.-Y. Tang, C. W. Brown, *Journal of Raman Spectroscopy* **1974**, *2*, 209–215.

[2-21]  S. N. Yannopoulos, K. S. Andrikopoulos, *The Journal of chemical physics* **2004**, *121*, 4747–58.

[2-22]  D. J. Milliron, D. B. Mitzi, M. Copel, C. E. Murray, *Chemistry of Materials* **2006**, *18*, 587–590.

[2-23]  S. S. Dhingra, M. G. Kanatzidis, *Inorganic Chemistry* **1993**, *32*, 1350–1362.

[2-24]  C.-H. Chung, S.-H. Li, B. Lei, W. Yang, W. W. Hou, B. Bob, Y. Yang, *Chemistry of Materials* **2011**, *23*, 964–969.

[2-25]  V. M. Glazov, A. S. Pashinkin, V. A. Fedorov, **2000**, *36*, 641–652.

[2-26]  B. J. Stanbery, *Critical Reviews in Solid State and Materials Sciences* **2002**, *27*, 73–117.

[2-27]  S. Zhang, S.-H. Wei, A. Zunger, H. Katayama-Yoshida, *Physical Review B* **1998**, *57*, 9642–9656.

[2-28]  W. Liu, D. B. Mitzi, M. Yuan, A. J. Kellock, S. J. Chey, O. Gunawan, *Chemistry of Materials* **2010**, *22*, 1010–1014.

[2-29]  J. A. M. AbuShama, S. Johnston, T. Moriarty, G. Teeter, K. Ramanathan, R. Noufi, *Progress in Photovoltaics: Research and Applications* **2004**, *12*, 39–45.

[2-30]  D. B. Mitzi, O. Gunawan, T. K. Todorov, K. Wang, S. Guha, *Solar Energy Materials and Solar Cells* **2011**, *95*, 1421–1436.

[2-31]  S. Bag, O. Gunawan, T. Gokmen, Y. Zhu, T. K. Todorov, D. B. Mitzi, *Energy & Environmental Science* **2012**, *5*, 7060.

[2-32]  W. Shockley, H. J. Queisser, *Journal of Applied Physics* **1961**, *32*, 510.

[2-33]  Nelson, "The Physics of Solar Cells," can be found under http://books.google.com/books/about/The_Physics_of_Solar_Cells.html?id=s5NN34HL WO8C, **n.d.**

[2-34]  T. Wada, N. Kohara, S. Nishiwaki, T. Negami, **2001**, 118–122.

[2-35]  B. L. Kronik, D. Cahen, H. W. Schock, **1998**, 31–36.

[2-36]  S.-H. Wei, S. B. Zhang, A. Zunger, *Journal of Applied Physics* **1999**, *85*, 7214.

[2-37]  G. Hanna, T. Glatzel, S. Sadewasser, N. Ott, H. P. Strunk, U. Rau, J. H. Werner, *Applied Physics A* **2005**, *82*, 1–7.

[2-38]  L. M. Mansfield, I. L. Repins, J. W. Pankow, M. R. Young, C. Dehart, R. Sundaramoorthy, C. L. Beall, B. To, M. D. Carducci, D. M. Honecker, **2011**.

[2-39]  S. Ishizuka, A. Yamada, P. Fons, S. Niki, *Journal of Renewable and Sustainable Energy* **2009**, *1*, 013102.

[2-40]  F. Kessler, D. Rudmann, *Solar Energy* **2004**, *77*, 685–695.

# Chapter 3 Novel Solution Processing of High Efficiency Earth Abundant Cu$_2$ZnSn(S,Se)$_4$ Solar Cells

## 3.1    Introduction

Kesterite copper zinc tin chalcogenide (CZTS) exhibits optical and electronic properties comparable to those of the Cu(In,Ga)(S,Se)$_2$ (CIGS) and CdTe material systems while consisting entirely of nontoxic constituents that avoid the scarcity and cost issues associated with indium and tellurium.[3-1] Developing a reliable fabrication route for producing single phase kesterite material is essential for an in-depth exploration of its intrinsic materials properties and ultimately the identification of avenues toward further improvement. Conventional vacuum-based high temperature approaches typically suffer from the high volatility of several elemental constituents as well as the narrow compositional stability window of the CZTS phase.[3-1,3-2] Non-vacuum deposition techniques are able to take advantage of the increased stability of each elemental constituent at atmospheric pressure, and films deposited from hydrazine-based slurries containing both liquid and solid phases currently hold the highest reported efficiency for this material system at 11.1%.[3-3]    In the present letter, we present a novel solution-based approach to process CZTS absorbers using fully dissolved CZTS precursor complexes in which each of the elemental constituents are mixed on a molecular scale.

In contrast to particle and slurry-based processing, the solution phase molecular precursors enable very precise stoichiometric control and eliminate the need for the long range diffusion of precursors during the formation of the CZTS phase.

As direct band gap semiconductors, the cost of raw materials for most chalcogenide systems is significantly reduced, as they require less material to achieve sufficient for light absorption. The remarkable tolerance for structural defects in many of these absorber materials also leads to reduced requirements on material quality and generally reduces processing costs compared with crystalline silicon solar cells.[3-4,3-5] With a highest demonstrated cell efficiency of 17.3%, CdTe-based photovoltaic technology has achieved 0.75 $/W at GW level production.[3-6,3-7] Chalcopyrite CIGS solar cells, without introducing the toxicity issues related to the use of cadmium and with an even higher demonstrated efficiency of 20.3%, are expected to reach GW level production in the near future.[3-8 to 3-10] The eventual cost of these technologies, and their ability to contribute to large scale PV power markets are inexorably tied to availability of indium, which is almost exclusively produced as a by-product of zinc mining and purification.[3-11] With indium effectively replaced by zinc and tin, kesterite CZTS consists solely of earth abundant, non-toxic, and inexpensive elements. As an absorber material, CZTS has an absorption coefficient of $\sim 10^4$ cm$^{-1}$ throughout much of the visible region, and an adjustable band gap that can be varied from 1 to 1.5 eV to favorably match the solar spectrum.[3-1]

Significant research attention has already been focused on the CZTS material family, and a number of successful devices have been demonstrated using a number of processing approaches. For vacuum-involved deposition approaches, 9.1% power conversion efficiencies of CZTSe have been achieved using co-evaporation which allows real-time control of the sample composition and reaction path,[3-12] efficiencies between 8~9% have

been reported by several groups through the selenization or sulfurization of precursor materials evaporated at low temperatures,[3-13 to 3-15] sputtered CZTS devices have reached 9.3% from the co-sputtering of binary compound targets and post sulfurization.[3-16] For solution-based approaches, a number of promising power conversion efficiencies have been reported using nanoparticle inks post-annealed under chalcogen vapor: 7.2% using a CZTS nanocrystal ink,[3-17] 8.4% from inks containing CZTGS nanocrystals,[3-18] and 8.5% (9.6% active area) from inks composed of binary and ternary chalcogenide nanocrystals.[3-19] The annealing of electrodeposited precursors has also produced devices with efficiencies around 7.3%.[3-20] Finally, hydrazine-based slurries containing both soluble and particulate precursors have deposited the absorber materials that currently hold the highest reported efficiency for this material system beyond 10%.[3-3, 3-21 to 3-23]

The advantages of the kesterite material system come at a price: consisting of a minimum of four distinct elements, kesterite materials are $I_2$-II-IV-$VI_4$ compounds, a fact that dramatically increases the complexity of their phase diagrams and introduces the possibility of forming a variety of electronically active defect structures.[3-24, 3-25] The rich defect chemistry of the CZTS material system ultimately brings about a number of difficulties that must be addressed during any deposition procedure. Perhaps the most challenging aspect of kesterite deposition, especially when compared with CIGS materials, is that single-phase kesterite exists within a much smaller stoichiometry range, and thus sophisticated compositional control is a prerequisite to achieving single-phase CZTS.[3-2] Careful control of the chemical potential of each reactant, which is effected by a variety of parameters including precursor concentration, processing conditions, etc., is very important in growing good-quality crystals with no secondary phase formation and

low-defect density.[3-25] A second challenge is presented by the volatile nature of tin chalcogenide compounds and the continuous changes in film composition that take place during the course of deposition and material formation. The potential decomposition of the CZTS phase induced by the loss of tin is a source of additional difficulties for composition and phase control, especially for processing techniques involving high vacuum and elevated temperatures.[3-26] Based on the complexity of the kesterite material system, we can expect that the ultimate success of a specific deposition method will come from its ability to reliably produce high quality films with excellent uniformity over all spatial dimensions. In this report, we explore one option for highly uniform and controllable CZTS film deposition at atmospheric pressure using fully dissolved molecular precursors based on the hydrazine solvent system.

## 3.2    Experiment details

### 3.2.1    Solution preparation

All hydrazine based solutions were prepared in a nitrogen filled glove box where oxygen and moisture levels are both below 1 ppm. *Note: Hydrazine is highly toxic, appropriate protective equipment should be used to prevent direct contact with the liquid or vapor.* To form the copper precursor solution, 1 mmol $Cu_2S$ and 2 mmol sulfur were combined with 1 ml $N_2H_4$, following the procedures describe elsewhere;[3-28] Similarly, the tin precursor solution was prepared in a separate vessel, by mixing and stirring 1 mmol of $SnS_2$ and 2 mmol excess sulfur in 1 ml $N_2H_4$.[3-30] To synthesize the chelated zinc precursor, the complexing agent hydrazinocarboxylic acid ($NH_2NHCOOH$) was first

49

prepared by adding hydrazine to a vial containing solid state carbon dioxide. It was

observed that the viscosity of the solution increases significantly as $NH_2NHCOOH$ is
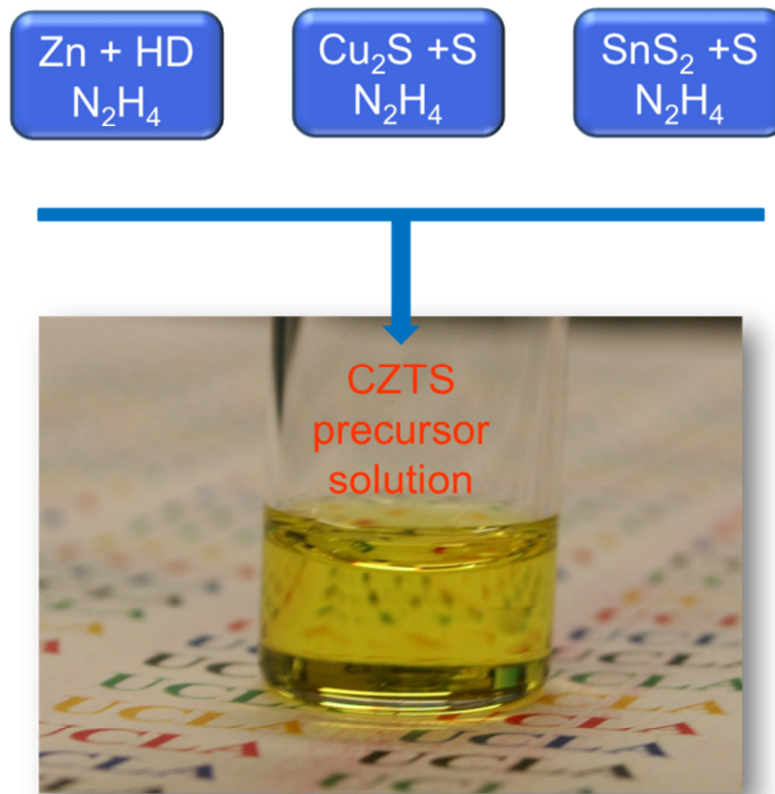


Figure 3-1. CZTS precursor solution preparation schematic and photograph of a solution

with the target ratio of Zn/Sn =1.2, Cu/(Zn+Sn) = 0.8. The zinc precursor was

synthesized through the reaction of metallic zinc and hydrazinocarboxylic acid (HD)

derived from hydrazine and carbon dioxide.

gradually formed in the system. *Note: the reaction between carbon dioxide and hydrazine is highly exothermic; the synthesized product has a corrosive effect on stainless steel.* 2 mmol zinc nanopowder was added into 1 ml $H_2NHCOOH$ saturated hydrazine solution, producing a moderately vigorous reaction with the continuous generation of fine bubbles in the mixture. This reaction was typically conducted on the scale of several tens of milliliters in one iteration. The solution was stirred for several hours to enable the full reaction of zinc powder with the complexing agent. The final CZTS precursor solution was prepared by mixing each constituent solution with a final ratio of Zn/Sn = 1.2 and Cu/(Zn+Sn) = 0.8.

### 3.2.2 Device fabrication and characterization

CZTS based photovoltaic devices were fabricated with the structure of glass/Mo/CZTSSe/CdS/ZnO/ITO. The p-type CZTS films were deposited via spin coating from the as prepared precursor solution in a glove box on molybdenum coated soda lime glass substrates. To reach the targeted thickness of the absorption layer, several successive layers were coated following an intermediate heat treatment between 250-350 $^o$C. A final annealing was conducted on a ceramic hot plate at 500 $^o$C verified by an infrared thermometer with different chalcogen vapor supply including pure selenium vapor, sulfur vapor and mixed vapor treatment. The n-type layer CdS was deposited via a standard chemical bath deposition method described previously.[3-28] Intrinsic ZnO and ITO were deposited using RF-sputtering with argon flow as the transparent electrode. The current-voltage (I-V) performance was measured under an AM1.5G filter at 100 mW/cm$^2$ using a Newport Oriel 92192 solar simulator. External quantum efficiency (EQE) was measured using a system designed by Enli Tech.

### 3.2.3. Materials characterization

For XPS, XRD, and Raman analysis, films were deposited via spin coating onto molybdenum coated glass, while power was prepared by evaporating the solvent from the precursor solution itself. Both the films and powder samples were annealed at the desired temperature on a hot plate with temperature verified by IR thermometer. The XPS measurements were performed using an Omicron XPS/UPS system, with base pressure is lower than $10^{-9}$ mBar. A monochromatic Al $K_\alpha$ (1486.6 eV) X-ray source was used for excitation and the spectra were collected with a pass energy of 50 eV. To exclude the influence from surface absorbed oxygen and carbon, $Ar^+$ ion (3 KeV) etching for 3 mins was performed before collecting X-ray generated electrons. RBS analysis was conducted by Evans Analytical Group, with the spectra acquired at a backscattering angle of $160^o$ and a grazing angle at $110^o$, using $He^{++}$ ion beam with the energy of 2.275 MeV. XRD patterns were collected on a PANalytical X'Pert Pro X-ray Powder Diffractometer using Cu-$K_\alpha$ radiation ($\lambda$ = 1.54060 Å). Raman shift spectroscopy was carried out using a Renishaw inVia Raman Microscope using an excitation laser with a wavelength of 514 nm. The cross-sectional scanning electron microscope (SEM) images were taken on a JEOL JSM-6700F.

### 3.3    Results and Discussion

The targeted processing method is based on a homogeneous CZTS precursor solution, similar to the hydrazine-based solution-processable precursors that have been demonstrated to produce high quality CIGS films.[3-27 to 3-29] The chalcogenides of copper, tin, and a number of other metals ($Cu_2S$, $In_2Se_3$, $SnS_2$, etc. )[3-30 to 3-32] readily dissolve in

hydrazine in the presence of excess chalcogen to form metal chalcogenide complexes coexistent with hydrazinium species. Unlike the various soluble chalcogenide compounds, zinc compounds such as ZnS and ZnSe, together with most other transition metals and metal chalcogenides typically show negligible solubility in hydrazine-based solvent systems.[3-33] Here we present a way to incorporate soluble zinc constituents into hydrazine in a completely dissolved form, stable in the presence of dissolved copper and tin complexes.  By forming complexes using a hydrazine derivative, zinc can be efficiently incorporated into hydrazine-based precursor solutions as a soluble reactant.

To synthesize the zinc precursor, the complexing agent hydrazinocarboxylic acid ($NH_2NHCOOH$) was prepared by adding hydrazine to a vial containing excess solid state carbon dioxide.[3-46]
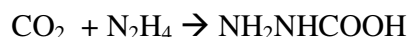
$$CO_2 + N_2H_4 \rightarrow NH_2NHCOOH$$

*Note: The reaction between carbon dioxide and hydrazine is highly exothermic; the synthesized product is capable of corrosive action on stainless steel.* 2 mmol zinc nanopowder was then added into 1 ml $H_2NHCOOH$ saturated hydrazine solution and subjected to stirring for several hours to enable the full reaction of zinc powder with the complexing agent. The completed CZTS precursor solution is then prepared by mixing hydrazine-based copper and tin precursor solutions, prepared through previously reported methods,[3-27,3-28,3-30]with the newly formed zinc precursor keeping an appropriate ratio between the metals, as shown in figure 3-1. After continued stirring, the result is a clear solution consisting of soluble copper, zinc, and tin precursor complexes. Detailed study of the structure and dissolution mechanism of the zinc complex will be described in Chapter 5. The molecular scale homogeneity of the precursor solution enables (i) the

53

freedom to independently adjust and precisely control the ratio of Zn/Sn, Cu/(Zn+Sn), and S/Se by simply varying the ratio of each type of precursor, (ii) enhanced spatial uniformity in subsequently deposited films, and (iii) the capacity to form a homogeneous kesterite CZTS phase without the need for long range diffusion between different precursor phases, as might be expected in a slurry system, layered precursor films, or other initially inhomogeneous precursor systems.

The unique hydrazinocarboxylic acid ligand system leads to the formation of high purity kesterite films. The solution-phase processing of metal chalcogenides using a hydrazine-based solvent system has the unique advantages of avoiding potential impurities such as C, O, or Cl, as are commonly encountered when using organic solvents or metal salt precursors. As a result, high quality semiconducting films and electronic devices can be achieved such as high mobility transistors based on $SnS_2$ or $In_2Se_3$ and high performance CISS and CIGS solar cells with efficiencies up to 15.2%.[3-30, 3-32, 3-34] Although the undesirable elements of carbon and oxygen were introduced into the precursor solution in order to induce the formation of the zinc precursor, the chosen hydrazinocarboxylic acid complexing agent yields a comparatively pure absorber film without significant amounts of impurities elements. Similar to the weakly coordinating hydrazinium complexes formed in typical hydrazine precursor solutions,[3-35] the volatile hydrazinocarboxylic acid species is able to easily decompose back into to gaseous species after moderate thermal treatment without leaving behind carbon and oxygen impurities in the deposited film. In its coordinated form, where hydrazinocarboxylic acid acts as a bidentate ligand,[3-36] chelated metal complexes yield metal powder upon annealing, without leaving behind any impurity elements such as carbon, oxygen, or nitrogen.

54

Reported examples of hydrazinocarboxylic acid complexes that decompose to produce pure metal upon annealing include chelated compounds of copper, zinc, nickel, and cobalt.[3-37 to 3-39]

In this study, X-ray Photoelectron Spectroscopy (XPS) characterization was employed to check the concentrations of impurity elements within the CZTS film after heat treatment at 500 $^o$C. The main peaks of Cu ($2p_{3/2}$), Zn ($2p_{3/2}$), Sn ($3d_{5/2}$), and S ($2p_{3/2}$) are labeled in figure 3-2A, no evidence of other elements was detected (all remaining unlabeled peaks represent other electron transitions associated with the four elemental film constituents). A high resolution scan (figure 3-2B) around the O (1s) peak detected no trace of oxygen (the detection limit of XPS is < 0.1%), while the intensity of C (1s) is about three orders lower than that of Cu($2p_{3/2}$), suggesting a low impurity concentration of less than 0.5 atomic %. Rutherford Backscattering Spectroscopy (RBS) analysis on annealed thin film samples indicates that the carbon composition throughout the entire depth of the film is below the system detection limit. Compared with other CZTS deposition approaches utilizing organic solvents and ligands, which normally leave behind a carbon-rich layer at the backside of device, the additive introduced here has the advantages of achieving a chemically cleaner film. With appropriate additives and complexing agents, the capacity for hydrazine solution processing could be effectively be extended to new materials of interest beyond the current realm of metal chalcogenides that are currently soluble in the hydrazine-chalcogen system.[3-35]
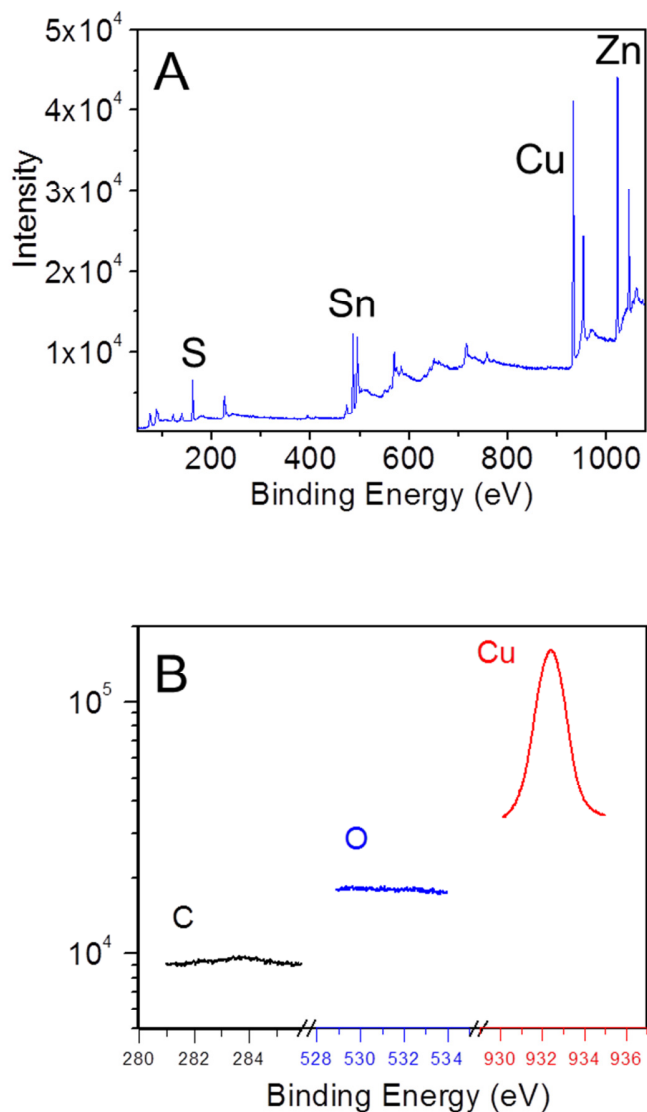
Figure 3-2. X-ray photoelectron spectroscopy (XPS) analysis on solution deposited CZTS films after heat treatment at 400 °C. Prior to the analysis, a sputter cleaning step was applied using $Ar^+$ ions (3 KeV) to remove adsorbed oxygen and carbon from the air. (A) Fast scan of the CZTS surface showing the main peaks of Cu, Zn, Sn, S. (B) Isolated signal from possible impurities (C/O) compared with signal from a main element (Cu) obtained from a high resolution scan using the same set of parameters.

The formation of the kesterite phase from CZTS precursor solutions takes place at low temperatures, suggesting a kinetically viable transformation that does not rely on the long-range motion of precursor constituents. Figure 3-3A shows the thermogravimetric analysis (TGA) data for dried CZTS precursor preheated to 100 $^{\circ}$C to evaporate any excess hydrazine solvent. The low temperature weight loss regime (below 200 $^{\circ}$C) corresponds to the dissociation of hydrazine and other volatile complexing agents present in the film. Figure 3-3B shows the XRD pattern of the sample after 250 $^{\circ}$C annealing, exhibiting the main diffraction peaks (112) (220) (312) of kesterite CZTS. Calculated from the full-width at half-maximum (FWHM), the estimated overall grain sizes are around 15-20 nm. Due to the strong overlap between the main diffraction peaks of CZTS, ZnS, and $Cu_2SnS_3$ and the low signal arising from the characteristic (110) peak of CZTS at this level of crystallinity, Raman spectroscopy was used to further investigate the formation and purity of the CZTS phase. The Raman spectrum shown in figure 3-3C more concretely verifies the formation of the kesterite CZTS phase, with the characteristic peak at 338 cm$^{-1}$ corresponding to A1 vibration mode of CZTS lattice where the group VI atoms (S or Se) vibrate while the rest of atoms remain fixed.[3-40] The rapid phase evolution even at relatively low temperatures suggests a small activation energy for the decomposition of the original precursor complex. The observed low reaction temperatures can be correlated to the unique chemistry of hydrazine and its derivatives: weakly coordinating and highly volatile hydrazine and hydrazinium complexes spontaneously decompose into gaseous species after only a gentle heat treatment, leading to the direct formation of the chalcogenide products. These results agree well with the decomposition of other hydrazinium precursor systems: the CISS
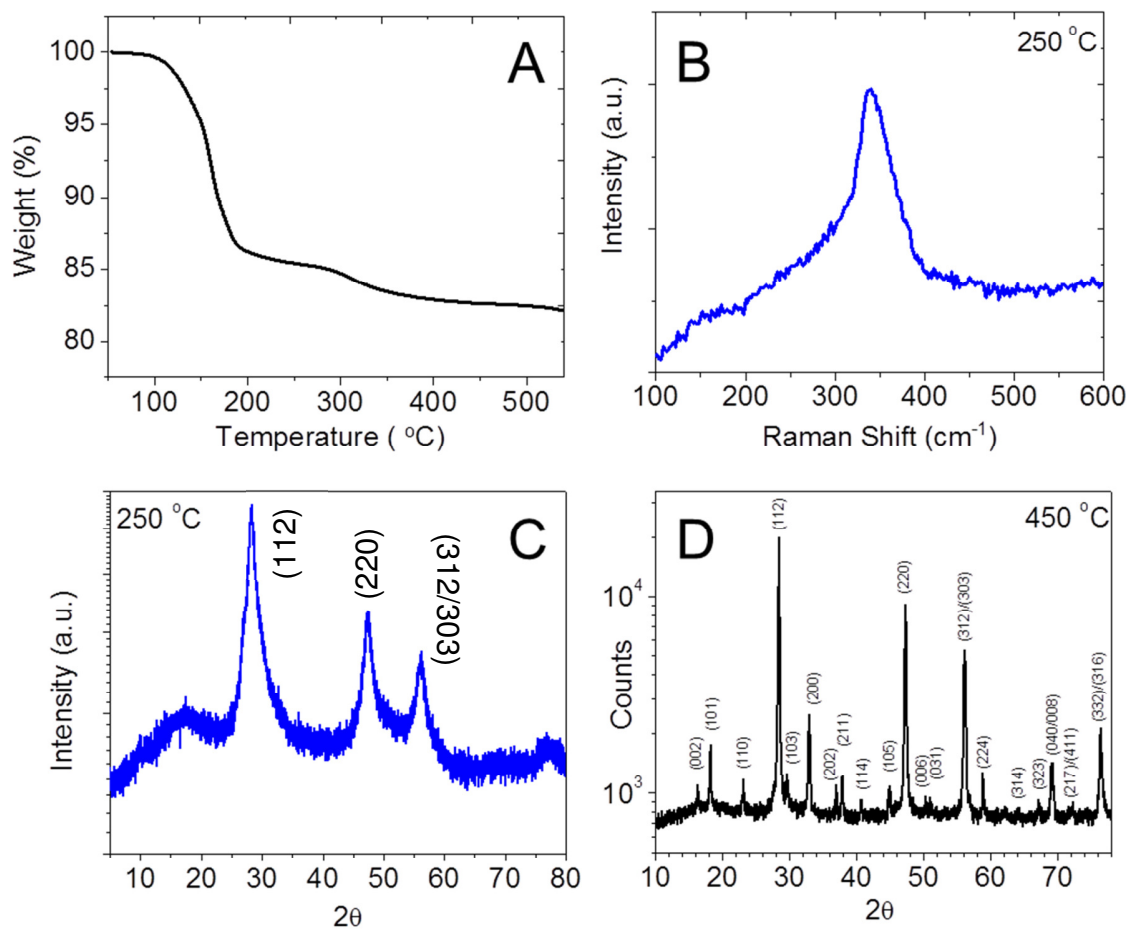
Figure 3-3. Thermal analysis and phase evolution of the CZTS precursor materials. (A) Thermogravimetric analysis of a powder sample at a heating rate of 2 $^{o}$C/min in flowing argon. The sample was pre-annealed at 100 $^{o}$C in an inert atmosphere from the precursor solution in figure 3-1 to evaporate excess solvent. (B), (C) Raman spectra and X-ray diffraction pattern of the sample after going through the first main step of weight loss at 250 $^{o}$C under an inert atmosphere, showing the main diffraction peak of (112), (220), (312)/(303). (D) XRD pattern of powder with a maximum annealing temperature of 450 $^{o}$C in an inert atmosphere, identified as kesterite $Cu_2ZnSnS_4$, JCPDF 00-026-0575.

phase has been previously reported to form from dried Cu-In-S-N$_2$H$_4$ precursor films upon annealing at temperatures as low as 100 $^{\circ}$C.[3-28]

After the first stage of weight loss centered around 150 $^{\circ}$C in the TGA data, further annealing up to 450 $^{\circ}$C does not lead to significant structural variations in the material, but induces a general increase in grain size throughout the film. Based on the analogous transformation in hydrazine processed CuIn(S,Se)$_2$, the weight loss transition between 300 and 350 $^{\circ}$C likely corresponds to the loss of extra sulfur loosely held within the film, but not actually incorporated into the CZTS lattice.[3-41] The diffraction spectrum of the final product (Figure 3-3D), annealed at 450 $^{\circ}$C, shows good crystallinity in the desired kesterite phase (JCPDF 00-026-0575), with the lattice constants a = b = 5.4270 Å and c = 10.8480 Å. There are neither unidentified peaks nor peaks from secondary phases such as tin sulfide or copper sulfide in the spectrum. The single phase product indicates the capability of the current approach to obtain the CZTS phase while maintaining the flexibility for facile compositional adjustment. The gradual weight loss visible in the final stage of the TGA data at temperatures beyond 500 $^{\circ}$C corresponds to the slow decomposition of the kesterite CZTS phase associated with Sn losses at high temperatures by forming volatile secondary phases likely related to SnS and S dissociation.[3-26] The addition of excess chalcogen vapor and optionally small amounts of tin is recommended during high temperature annealing in order to promote grain growth while minimizing the presence of detrimental impurity phases associated with the decomposition of kesterite at high temperatures.
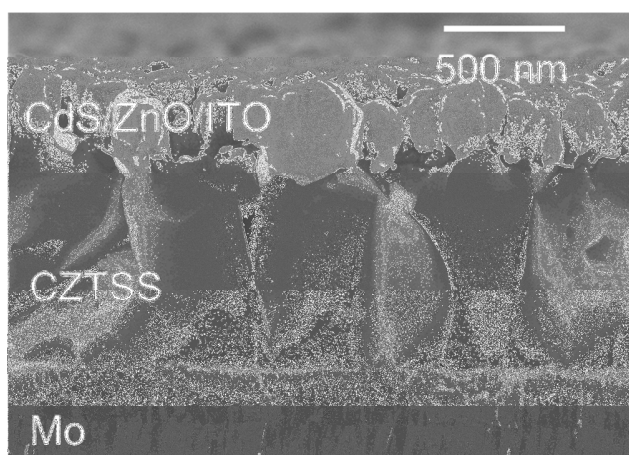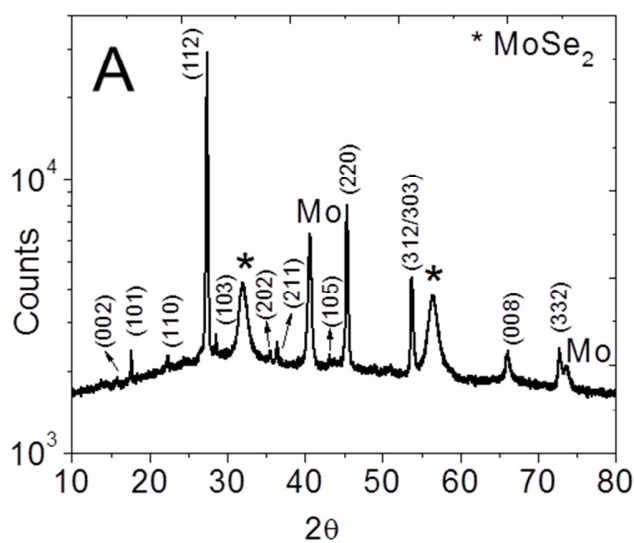
Figure 3-4. (A) XRD pattern of a CZTS film on Mo/glass substrate after heat treatment at 500 °C under selenium vapor, identified as kesterite $Cu_2ZnSnSe_4$ (JCPDF 00-052-0868) with the tetragonal lattice constants a = b = 5.6930 Å, c = 11.3330 Å. Peaks arising from the Mo substrate and the $MoSe_2$ interlayer are noted. (B) Cross-sectional SEM images of a typical CZTSS device, with the structure Mo/CZTSS/CdS/ZnO/ITO. A layer of $MoSe_2$ showing a slightly different morphology with the underlying Mo is noted at the interface between the CZTSS and Mo layers.

CZTS film deposition for device fabrication was conducted using spin coating in a nitrogen-filled glove box. Thermal treatment with peak processing temperatures between 400 and 540 $^{\circ}$C for each deposited film was performed on a hotplate in the presence of chalcogen vapor. Figure 3-4A shows the XRD patterns of CZTS thin films deposited onto Mo-coated glass after heat treatment with added selenium vapor. The diffraction peaks from molybdenum and $MoSe_2$ are detectable from the substrate and interfacial layers directly under the CZTS film. The structure is identifiable as (JCPDF 00-052-0868), a = b = 5.6930 Å, c = 11.3330 Å, with a preferred orientation in the (112) direction. Replacement of S atoms by Se leads to a unit cell volume expansion around 15% from 319 Å$^3$ for the pure sulfide to 367 Å$^3$ for pure selenide. The grain expansion effectively shrinks the inner voids normally formed after liquid-phase deposition and post annealing, resulting in a morphology composed of close-packed large grains. Cross-sectional SEM imaging, as shown in figure 3-4B, indicates that the CZTSe film consists of large crystallites with diameters beyond the layer thickness, with no obvious voids between. The detected $MoSe_2$ phase in the diffraction pattern corresponds to the interlayer between the molybdenum and CZTSe showing a slightly different columnar morphology from the molybdenum substrate in the SEM image. Note that the presence of a carbon layer frequently found in films prepared from organic solvents based precursor is not observed in this case at the back side of the device between the CZTS absorber and Mo back contact. The capability for the current approach to obtain a film free of non-volatile impurities is a benefit of the unique chemistry of hydrazine and its derivatives and agrees well with the previously shown compositional analysis.

The ability to tune the properties of the absorber material, especially the band gap, to a target value is critical in achieving high efficiency photovoltaic devices. Based on theoretical calculations, roughly 1.5 eV can be considered an optimal band gap value for single junction solar cells.[3-42] Experimentally, large band gap chalcopyrite materials (typically gallium-rich or sulfur-rich CIGS) show deteriorated performance due to increasingly active deep level recombination centers as the position of the conduction band minimum increases.[3-43] In the kesterite materials system, large band gap CZTS similarly shows reduced performance compared with selenium-rich material. Here we demonstrate the capability to control the S/Se ratio and resulting electronic band gap value by employing different chalcogen vapor compositions during the annealing process. Type I absorbers are pure CZTSe material formed by annealing under selenium vapor, type II absorbers are formed under combined sulfur and selenium vapor, and type III CZTS films are annealed under only sulfur vapor.

The (112) diffraction peaks of the three types of film are shown in Figure 3-5A. The diffraction peak shifts to smaller $2\theta$ values as the selenium content increases, indicating an increase in lattice constant due to the replacement of sulfur with selenium. Raman spectroscopy (Figure 3-5B) on the films shows the same trend with varying S/Se ratio. For the sulfide film, the major peaks appear at 338 cm$^{-1}$, 287 cm$^{-1}$ and 368 cm$^{-1}$, consistent with previously reported CZTS values.[3-44] For selenide films, the main peaks shift to 196 cm$^{-1}$, 172 cm$^{-1}$ and 238 cm$^{-1}$, agreeing well with the reported values for
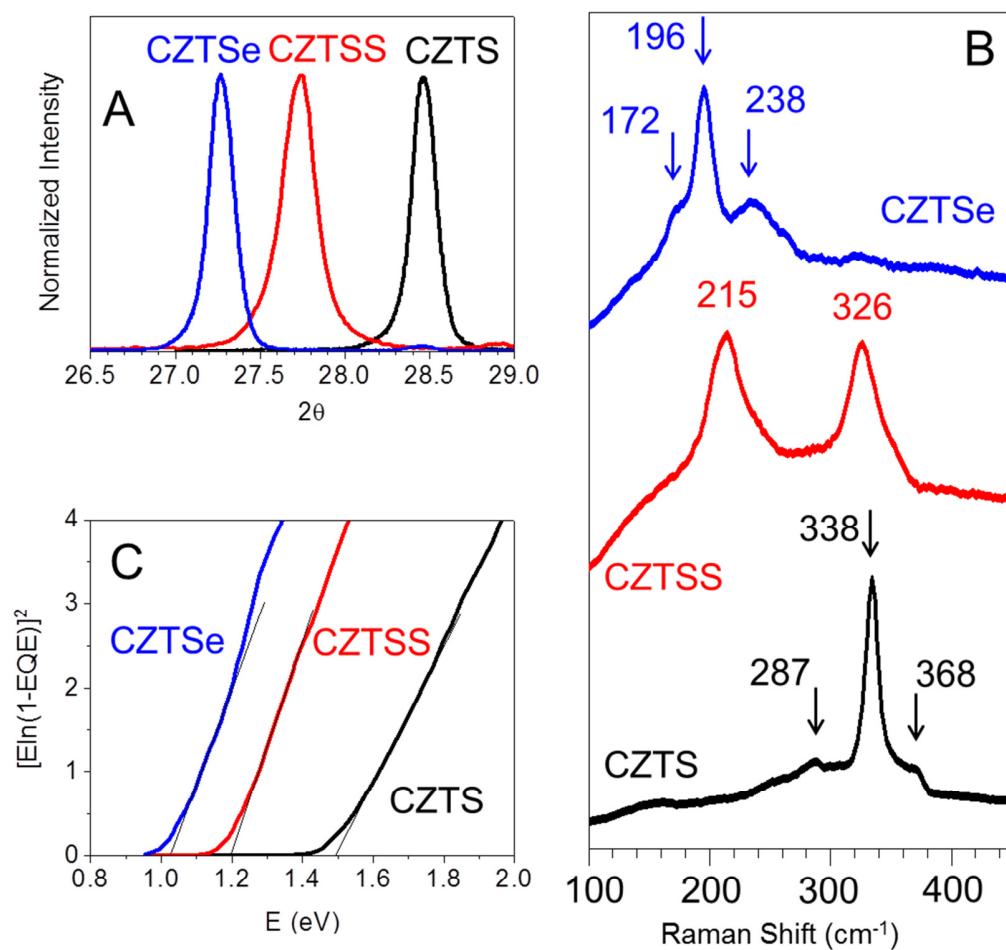
Figure 3-5. Structural and optoelectronic properties of solution deposited $Cu_2ZnSnS_{4-x}Se_x$ absorber layers with varying S/Se content incorporated from an annealing step at 500 $^o$C under different chalcogen vapor compositions. (A) Shifts in the (112) diffraction peak with increasing Se content in absorber layer. The small peaks visible around 28.5$^o$ and 29$^o$ in the selenium-rich films belong to the (103) diffraction peaks of CZTSe and CZTSS. (B) Raman spectra of CZTSS films with varying S/Se ratio and appropriately shifted vibration modes. (C) Band gap values calculated from the external quantum efficiency (EQE) measurements of devices with the varying S/Se content.

CZTSe.[3-45] For films with intermediate S/Se content, the main peaks from both sulfide and selenide are present, and shift toward one other, following the same trend as previously reported for CZTSSe with an intermediate S/Se ratio.[3-2] The major peaks in each Raman spectra arise from the vibrational modes where chalcogen atoms oscillate while other atoms remain fixed.[3-40] Raman spectroscopy is also able to detect possible secondary phases such as ZnS and $Cu_2SnS_3$ that cannot be distinguished by diffraction techniques due to their similar structure to kesterite. No evidence of other possible binary phases ($Cu_2S$, $Cu_2Se$, ZnS, ZnSe) appears in the Raman spectrum for films under any of the previously mentioned heat treatments. The external quantum efficiency (EQE) measurements of photovoltaic devices can be used to determine the absorber layer band gap by fitting a plot of $[E \ln(1-EQE)]^2$ vs. E near the band edge. The calculated band gap values are 1.02 eV, 1.2 eV, and 1.5 eV for type I, II, and III absorbers respectively as shown in figure 3-5C. These results agree well with band gap values determined using other approaches,[3-2] and demonstrate that by judiciously adjusting the chalcogen vapor supply during post-annealing, the resulting band gap value can be adjusted controllably throughout the range of 1.02 to 1.5 eV.

The final test of any film formation method is the fabrication of a completed device. Precursor solutions with the target ratios Zn/Sn = 1.2 and Cu/(Zn + Sn) = 0.8 were using for photovoltaic device fabrication. Copper-poor and zinc-rich stoichiometry has been reported to be beneficial in both vacuum-based and solution-processed approaches for the CZTS material system.[3-1,3-21] The cross-sectional SEM of a completed device with the commonly employed structure of glass/Mo/CZTS(Se)/CdS/i-
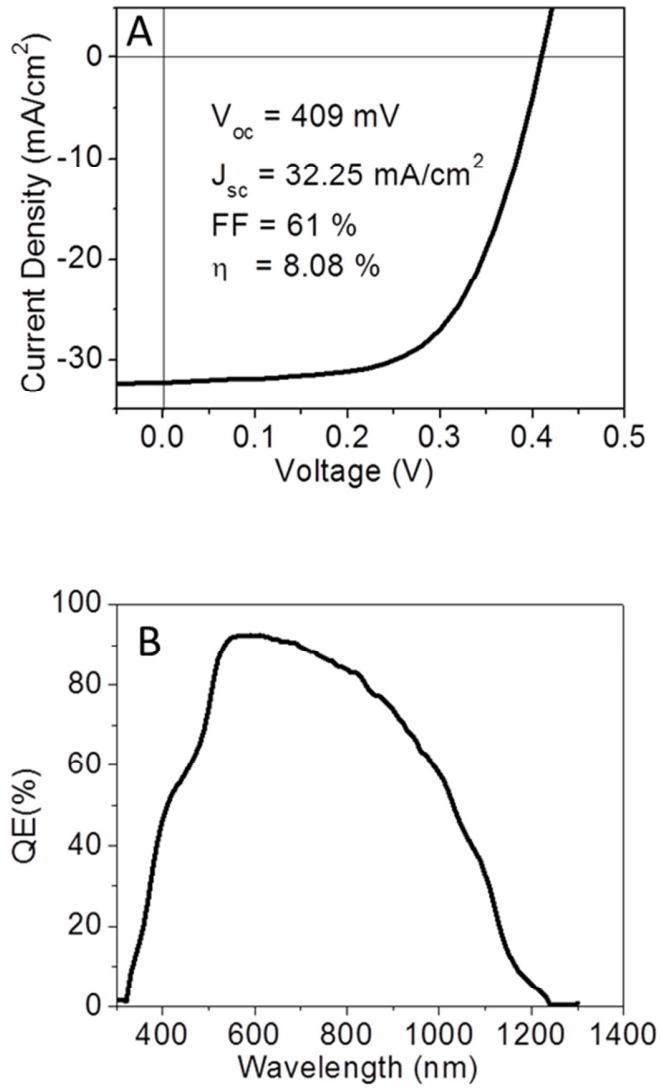
Figure 3-6. Device electrical characterization. (A) Current-Voltage (I-V) characteristics of one of the best CZTSS device achieved to date using the solution-processing approach under Air Mass 1.5 illumination, 100 mW/cm$^2$. (B) External quantum efficiency (EQE) spectrum of the device without any applied bias.

ZnO/ITO is shown in figure 3-4B. Illuminated Current-Voltage (I-V) characteristics for one of the best devices achieved to date are shown in Figure 3-6A, with a 120 nm-thick MgF$_2$ antireflection layer. Under simulated AM1.5 light, the device produces a short-circuit current density (J$_{SC}$), open-circuit voltage (V$_{OC}$), fill factor, and power conversion efficiency of 32.3 mA/cm$^2$, 409 mV, 61.0%, and 8.08% respectively. The device area of 0.12 cm$^2$ is determined by mechanically scribing the finished device in order to separate the upper layers from the rest of the 1.5 x 1.5 cm$^2$ substrate. Besides the best performing device shown in Figure 3-6A, a number of other devices fabricated under slightly differing conditions have also been demonstrated with efficiencies above 7%. The continued refinement of compositional and phase control may allow this method to compare competitively with vacuum-based approaches as a platform for both large scale film production and for the exploration of materials properties in order to further advance our understanding of this material system.

The integrated short circuit current density extracted from EQE measurements, shown in Figure 3-6B for a CZTSSe device, agrees well with that obtained under simulated sunlight. The incomplete current collection in the infrared region, especially beyond 800 nm, indicates the need for a thicker absorber with enhanced minority carrier transport. Perhaps the largest room for improvement compared with chalcopyrite devices with similar band gap values is in open circuit voltage. Possibilities include the existence of charge transportation barriers either at the back contact arising from interfacial MoSe$_2$, or parasitic recombination at the interface between the absorber and buffer layers. Compared with its analogue CIGS materials, the minority carrier life time in the CZTS device is one order smaller that mainly corresponds to the deficit of V$_{oc}$.[3-47] With further

optimization of the device components, we believe the CZTS photovoltaic devices based on the current processing approach could reach power conversion efficiencies well above 10 percent.

By introducing hydrazine derivatives, zinc compounds have been successfully incorporated into hydrazine solution to enable the formation of a CZTS precursor solution that is homogeneous on the molecular scale. Solutions produced in this manner provide a robust way to tune the metallic stoichiometry, allowing for films to fall within the relatively narrow window for the formation of the CZTS phase with minimal secondary phases present. High quality single phase films can be achieved using this approach, with the capacity for the continuous adjustment of the material's band gap from 1.0 to 1.5 eV through the use of annealing treatments in chalcogen vapor of varying composition. The rapid decomposition of the employed precursor species is able to favorably form kesterite CZTS at low temperatures, which circumvents one of the challenges faced by vacuum-based approaches involving the loss of volatile components such as tin and tin(II) sulfide. The homogeneous nature of this processing approach enables potentially scalable high-throughput film production, compatible with the TW target provided by the earth abundant raw materials of this absorber system. Furthermore, the chemical and structural purity of the final product, formed by incorporating hydrazine derivatives into the solvent, expands the metal chalcogenide materials that can be incorporated into hydrazine-based precursor solutions that are homogeneous on a molecular level for use in semiconducting thin film deposition.

**References**

[3-1] H. Katagiri, K. Jimbo, W. S. Maw, K. Oishi, M. Yamazaki, H. Araki, A. Takeuchi, Thin Solid Films **2009**, 517, 2455.

[3-2] D. B. Mitzi, O. Gunawan, T. K. Todorov, K. Wang, S. Guha, Solar Energy Materials and Solar Cells **2011**, 95, 1421-1436.

[3-3] D. B. Mitzi, High-Performance Photovoltaics from Earth-Abundant Thin-Film Absorbers, IEEE Photovoltaics Specialists Conference 38 (**2012**).

[3-4] B. J. Stanbery, Critical Reviews in Solid State and Materials Sciences, 27(2):73–117 (**2002**).

[3-5] I. Visoly-Fisher, S.R. Cohen, A. Ruzin, D. Cahen, Adv. Mater., 16 (**2004**) 879–883.

[3-6] http://investor.firstsolar.com/releasedetail.cfm?releaseid=593994.

[3-7] First Solar press release, Second Quarter 2010 Financial Results, http://investor.firstsolar.com

[3-8] I. Repins, M. A. Contreras, B. Egaas, C. DeHart, J. Scharf, C. L. Perkins, B. To, R. Noufi, Prog. Photovolt.: Res. Appl. **2008**,16, 235.

[3-9] P. Jackson, D. Hariskos, E. Lotter, S. Paetel, R. Wuerz, R. Menner, W. Wischmann, M. Powalla, Prog. Photovolt: Res. Appl. **2011**; 19:894·C897.

[3-10] http://www.solar-frontier.com/brochure_EU_Asia.php.

[3-11] http://energy.gov/sites/prod/files/DOE_CMS2011_FINAL_Full.pdf.

[3-12] I. Repins, et al., Co-evaporatedCu2ZnSnSe4 films and devices, Solar Energy Materials and Solar Cells (**2012**), doi:10.1016/j.solmat.2012.01.008.

[3-13] B. Shin, Y. Zhu, N. A. Bojarczuk, S. J. Chey, S. Guha, High-Efficiency Cu2ZnSnSe4 Solar Cells with a TiN Diffusion Barrier on the Molybdenum Bottom Contact, Proc. IEEE Photovoltaics Specialists Conference 38 (**2012**).

[3-14] B. Shin, O. Gunawan, Y. Zhu, N. A. Bojarczuk, S. J. Chey, S. Guha, Prog. Photovolt: Res. Appl. (**2011**), DOI: 10.1002/pip.1174.

[3-15] H. Sugimoto, H. Hiroi, N. Sakai, S. Muraoka, T. Katou, Over 8% Efficiency Cu2ZnSnS4 Submodules with Ultra-Thin Absorber, Proc. IEEE Photovoltaics Specialists Conference 38 (**2012**).

[3-16] V. Chawla, B. Clemens, Effect of Composition on High Efficiency CZTSSe Devices Fabricated Using Co-sputtering of Compound Targets, Proc. IEEE Photovoltaics Specialists Conference 38 (**2012**).

[3-17] Q. Guo, G. M. Ford, W. C. Yang, B. C. Walker, E. A. Stach, H. W. Hillhouse, R. Agrawal, J. Am. Chem. Soc., **2010**, 132 (49), pp 17384–17386.

[3-18] Q. Guo, G.M. Ford, H.W. Hillhouse, R. Agrawall, A generalized and robust method for efficient thin film photovoltaic devices from multinary sulfide nanocrystal inks, Proc. IEEE Photovoltaics Specialists Conference 37 (**2011**).

[3-19] Q. Guo, Y. Cao, J. V. Caspar, W. E. Farneth, A. S. Ionkin, L. K. Johnson, M. Lu, I. Malajovich, D. Radu, K. R. Choudhury, H. D. Rosenfeld, W. Wu, A Simple Solution-based Route to High-Efficiency CZTSSe Thin-film Solar Cells, Proc. IEEE Photovoltaics Specialists Conference 38 (**2012**).

[3-20] S. Ahmed, K. B. Reuter, O. Gunawan, L. Guo, L. T. Romankiw, H. Deligianni, Adv. Energy Mater. **2012**, 2, 253–259.

[3-21] T. Todorov, K.B. Reuter, D.B. Mitzi, Adv. Mater. **2010**, 22, 1–4.

[3-22] D. A. R. Barkhouse, O. Gunawan, T. Gokmen, T. K. Todorov, D. B. Mitzi, Prog. Photovolt:Res. Appl. (**2011**), DOI: 10.1002/pip.1160.

[3-23] S. Bag, O. Gunawan, T. Gokmen, Y. Zhu, T. K. Todorov, D. B. Mitzi, Energy Environ. Sci., DOI: 10.1039/c2ee00056c.

[3-24] Repins, I.; Vora, N.; Beall, C.; Wei, S. H.; Yan, Y.; Romero, M.; Teeter, G.; Du, H.; To, B.; Young, M.; Noufi, Kesterites and Chalcopyrites: A Comparison of Close Cousins. MRS Proceedings, 1324, mrss11-1324-d17-01 doi:10.1557/opl.2011.844.

[3-25] S. Chen, J. H. Yang, X. G. Gong, A. Walsh, S. H. Wei, Phys. Rev. B 81, 245204, (**2010**)

[26] A. Redinger, D. M. Berg, P. J. Dale, S. Siebentritt, J. Am. Chem. Soc. **2011**, 133, 3320–3323.

[3-27] D. B. Mitzi, M. Yuan, W. Liu, A. J. Kellock, S. J. Chey, V. Deline, A. G. Schrott, Adv. Mater., **2008**, 20, 3657–3662 .

[3-28] W. W. Hou, B. Bob, S. Li, Y. Yang, Thin Solid Films, 517 (**2009**), 6853–6856.

[3-29] B. Bob, B. Lei, C. Chung, W. Yang , W. Hsu, H. Duan, W. W. Hou, S. Li, Y. Yang, Adv. Energy Mater., **2012**, DOI: 10.1002/aenm.201100578.

[3-30] D. B. Mitzi, L. L. Kosbar, C. E. Murray, M. Copel, Nature **2004**, 428, 299

[3-31] D. B. Mitzi, Inorg. Chem. **2007**, 46, 926-931.

[3-32] D. B. Mitzi, M. Copel, S. J. Chey, Adv. Mater., **2005**, 17, 1285.

[3-33] D. B. Mitzi, T.K. Todorov, O. Gunawan, M. Yuan, Q. Cao, W. Liu, K.B. Reuter, M. Kuwahara, K. Misumi, A.J. Kellock, S.J. Chey, T. Goislard de Monsabert, A. Prabhakar, V. Deline, K. E. Fogel, Towards marketable efficiency solutionprocessed kesterite and chalcopyrite photovoltaic devices, in: Proceedings of the 35th IEEE Photovoltaics Specialist Conference (**2010**) 640–645.

[3-34] T. K. Todorov, O. Gunawan, T. Gokmen, D. B. Mitzi, Prog. Photovolt: Res. Appl. (**2012**), DOI: 10.1002/pip.1253.

[3-35] M. Yuan, D.B. Mitzi, Dalton Trans., **2009**, 6078-6088.

[3-36] A. Jesiha, A. Rahtena, P. Benkic, T. Skapina, L. Pejov, V. M. Petrus evski, Journal of Solid State Chemistry 177 (**2004**) 4482–4493.

[3-37] J. Macek, A. Rahten, Thermochimica Acta, 144 (**1989**) 257-266.

[3-38] B. N. Sivasankar and S. Govindarajan, Journal of Thermal Analysis, 46 (**1996**)117-127.

[3-39] N. Arul Dhas, C. Paul Raj, A. Gedanken, Chem. Mater. **1998**, 10, 1446-1452.

[3-40] M. Himmrich,  H. Haeuseler, Specmchimica Acta, Vol. 47A, No. 7, pp. 933-942.**1991**.

[3-41] D.J. Milliron, D.B. Mitzi, M. Copel, C.E. Murray, Chem. Mater. 18 (**2006**) 587.

[3-42] Nelson, J. The Physics of Solar Cells; Imperial College Press: London, **2003**.

[3-43] S. Siebentritt, U. Rau, Wide-gap Chalcopyrites, ISBN-10: 3540244972, **2006**.

[3-44] K. Wang, O. Gunawan, T. Todorov, B. Shin, S. J. Chey, N. A. Bojarczuk, D. Mitzi, S. Guha, Appl. Phys. Lett. 97, 143508 (**2010**).

[3-45] A. Redinger, K. Hönes, X. Fontané, V. I. Roca, E. Saucedo, N. Valle, A. P. Rodríguez, S. Siebentritt, Appl. Phys. Lett. 98, 101907 (**2011**).

[3-46] E. W. Schmidt, *Hydrazine and Its Derivatives: Preparation, Properties, Applications*, John Wiley & Sons, 2nd edn, 2001.

[3-47] O. Gunawan, T. K. Todorov, D. B. Mitzi, *Applied Physics Letters* **2010**, *97*, 233506.

# Chapter 4 CZTS Defect Properties and Electronic Properties

## 4.1    Introduction

The early-stage rapid developments on CZTS via various approaches show a promising future for kesterite photovoltaics.[4-1 to 4-6]A large $V_{oc}$ deficit currently limits the performance of devices based on Kesterite CZTS materials, especially compared to the analogous CIGS materials system.[4-7] The limiting on open circuit voltage is likely caused by the severe interface recombination, possibly on p-n junction interface or grain boundary interface belonging to CZTS itself. The intrinsic complex point defect and local structure fluctuation is also likely to introduce tail band of defects. Sophisticated electronic characterization on defect properties is critical to identify the device favorable properties and understand the cause of limiting factors from the point view of materials. The understanding on defect physics and recombination mechanisms is thus urgently needed for further improvement of the cell characteristics to a level comparable with Cu(In,Ga) (S,Se)$_2$ (CIGS) and CdTe.

## 4.2    Solar cell performance with different chalcogen content

The band gap control through the S/Se ratio is found to be critical on device performance relating to carrier recombination. Figure 4-1 shows the illuminated current density-voltage (J-V) characteristic curves for devices with different amounts of selenium and sulfur, with the corresponding external quantum efficiency (EQE) curves shown in the inset. The cell parameters deduced from J-V measurements, as well as the bandgap deduced from the long-wavelength cutoff of the EQE[4-8] are summarized in Table 4-1.
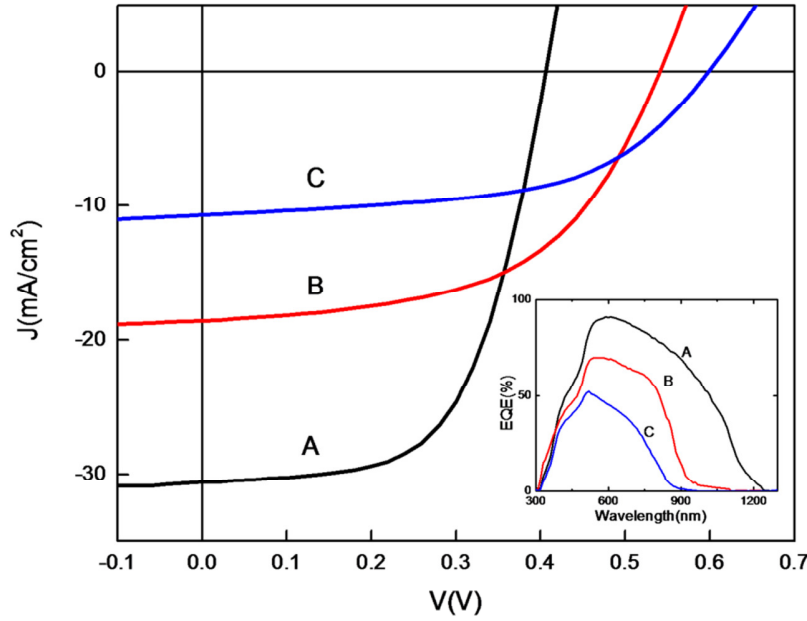
**Figure 4-1.** Light J-V data of CZTSSe devices with various sulfur contents. Low sulfur device (A) shows the highest efficiency ~7.4%. Inset: corresponding external quantum efficiency.

**Table 4-1. Device parameters for CZTSSe cells at room temperature using different S contents in absorber layer.**

| Sample [S]/( [S]+ [Se]) | | Eff(%) | $V_{oc}$(V) | $E_g$(eV) | $V_{oc}$ deficit $E_g$-q$V_{oc}$ | $J_{sc}$(mA/cm$^2$) | FF(%) |
|---|---|---|---|---|---|---|---|
| A | 0.35 | 7.4 | 0.406 | 1.15 | 0.74 | 30.5 | 59.55 |
| B | 0.8 | 5.3 | 0.541 | 1.35 | 0.81 | 18.5 | 53.57 |
| C | 1.0 | 3.5 | 0.599 | 1.5 | 0.90 | 10.7 | 54.28 |

The devices A, B, and C correspond to three different S contents of $[S]/([S]+[Se]) \approx 0.35$, 0.8 and 1, respectively. CZTSSe films were deposited through hydrazine solution processing. X-ray diffraction and Raman data indicate the presence of only the kesterite phase in the films, and are discussed in detail in a separate publication.[4-9]

The device with high sulfur content has a higher open-circuit voltage (~0.6V), consistent with its large bandgap (~1.5eV). The device with low sulfur content has relatively small open-circuit voltage (0.406V) but has much larger short-circuit current density ($J_{sc}$), mainly due to improved carrier collection at longer wavelengths. To exclude the effect of band gap on $V_{oc}$, the deficit of $V_{oc}$ ($E_g - V_{oc}$) indicates the device quality. Among the three devices, Se-rich sample shows a relative less deficit and S-rich one shows larger deficit. Low sulfur content device (sample A) also gives the highest power conversion efficiency of 7.4%. In EQE data measured at 0V (Figure 4-1(b)), the high sulfur content device (sample C) has a lower peak value than the others. This reveals that the S concentration in the alloy not only changes the bandgap but also gives rise to stronger recombination losses.

## 4.3    Sulfur role in CZTS defects

Impedance/admittance spectroscopy provides a useful method to understand the defect physics in photovoltaic devices. When semiconductor doped by its own crystalline defects, the energy levels and spatial distributions are extremely important factors to determine the electrical properties and photovoltaic properties. According to the classical diode model and semiconductor theories, both the defects and the doping properties can be linked to a quantifiable parameter – capacitance. For example, the voltage dependence

74

of capacitance can be related to charge density and depletion width, which in turn gives the spatial distribution of dopants. The frequency dependence of capacitance could suggest the response time of a charge trap at a certain temperature, when combined with the Arrhenius plot obtained at variable temperatures, the energy level of a defect can be characterized.[4-10] Using a combination of capacitance-based characterization techniques, both the spatial and energetic distribution of defect states can be determined**.**

### 4.3.1 Admittance spectroscopy

Admittance spectroscopy (AS) measurements, which are commonly used to estimate the energy level of defects inside the band gap, were taken on each of the three types of samples. Capacitance-Frequency (CF) scans taken in the temperature range 160K to 300K are shown in **Figure 4-2**. CF scans were measured in the dark from $10^2$ to $10^6$ Hz. An AC voltage of 30mV was used and DC bias was kept at zero during the measurement. Using the model implied by the work of Kimerling,[4-11] the capacitance at high frequency represents the response of the free carrier density, while the capacitance at low frequency represents the response of the sum of free carriers and deep traps. In Figure 4-2c, the capacitance of the device with high sulfur content shows a larger variation as a function of frequency, while the capacitance of the devices with low sulfur content show small changes between high and low frequencies (Figure 4-2a).The significant frequency dependence of the capacitance in the high sulfur content device indicates larger trap densities in the absorber. The similar trend has been reported recently for devices in which bandgaps fall in the range 1.0 to 1.5eV, but are fabricated by two different processes.[4-12] The carrier freeze-out behavior in the absorber was

proposed to explain the high series resistance of the devices measured at low temperatures, which might be due to the lack of the shallow acceptors (such as copper vacancies) as well as deep dominant acceptors in CZTSSe. Also, it is visible that capacitance data in Figure 4-2b and 2c converge at high frequency, where the capacitance might simply be from the geometric capacitance in the devices due to the carrier freeze-out.[4-13]
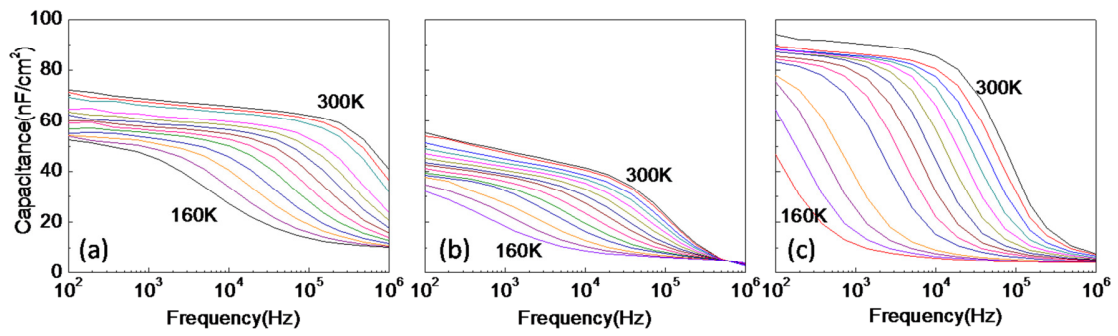


**Figure 4-2.**Admittance spectra of devices with various sulfur content, measured at temperature between 160K and 300K with a step of 10K. The y-axis of three plots have been scaled to be the same.

Form the temperature dependent step frequency, defects energy level could be calculated according to the frequency response of defects:

$$\omega_0 = 2\pi\nu_0 T^2 \exp(\frac{-E_a}{kT}), \qquad (4.1)$$

where $\omega_0$ is the step frequency, $E_a$ is the energetic depth of the defect relative to the corresponding band edge, and $\nu_0$ is the pre-exponential factor comprising all temperature independent terms, such as defect capture cross section for holes $\sigma_p$, effective density of

states in the valence band $N_V$, and thermal velocity $\upsilon_{th}$. **Figure 4-3** shows the Arrhenius

plot for the inflection points in the three admittance spectra in Figure 4-2. The step
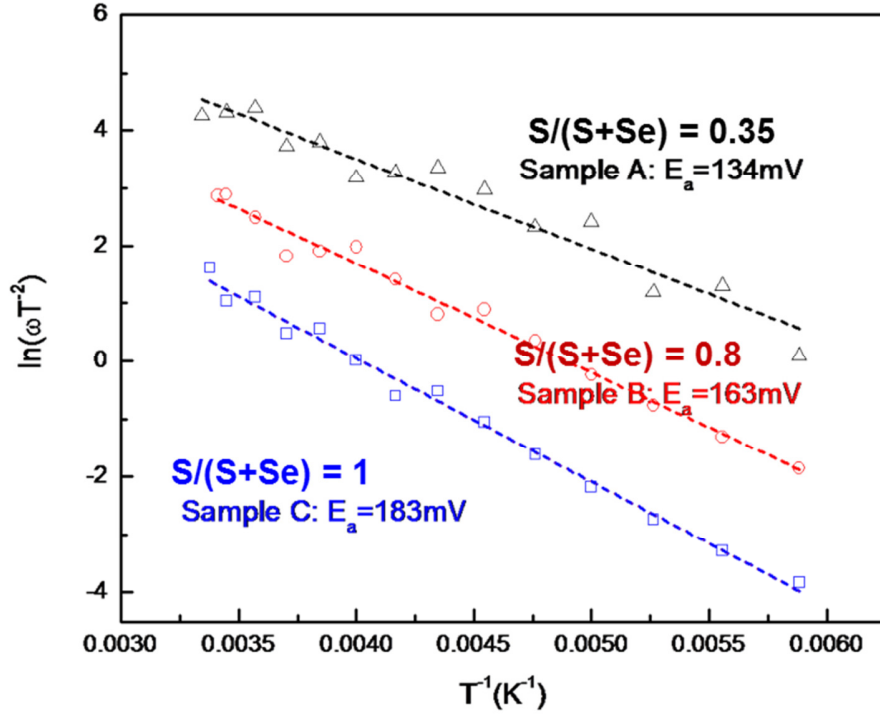


**Figure 4-3.** Arrhenius plot of the inflection frequencies determined from the derivative of admittance spectra.

frequency $\omega_0$ (or inflection point frequency) for each AS curve is determined by using the

angular frequency point at the maximum of the $\omega^*dC/d\omega$ plot. In this case, the activation

energy $E_a$ determined by the Arrhenius plot is approximately the energy difference

between defect level and valence band edge. Assuming that their energy levels are within

a small range, the $E_a$ value deduced from the Arrhenius plot can also represent the

average value of activation energies of a band of defects in the bandgap. The activation

energy $E_a$ is around 0.134eV, 0.163 eV and 0.183 eV for devices A, B and C (from low to

high sulfur content), respectively. Sulfur rich devices have a relative deeper level of

defects which counts to a more severe recombination center that limiting carriers separation. The distribution of defects level as S/Se ratio suggests Se-rich device has a relative benign performance. Defects properties agree well with the device performances in our system, also for film fabricated from other approaches. Currently the champion cell for Se-rich CZTS has achieved beyond 11% while sulfide based CZTS between 8-9 %. [4-1]

### 4.3.2 DLCP—carrier concentration

Traditional capacitance-voltage (CV) scans can provide the space defect density, but it is unable to distinguish between the bulk and interface defects, since both types of defects respond to this type of measurement. In order to identify different types of defects in the film (bulk defects, interface defects, and free carriers), Drive-Level Capacitance Profiling (DLCP) measurements were employed by using the technique of Heath at el,[4-14]. Compared to CV measurements, DLCP gives a more accurate assessment of the free carrier density in the film, while CV measurements are more sensitive to interface states which commonly exist in chalcopyrite-based cells. DLCP measurements were performed with DC bias from -0.5 to 0 volts with the AC amplitude varying from 0.01V to 0.1V, and temperature range from 160K to 300K. The measurement frequency of 11kHz was selected. Under such conditions we estimated that in the low sulfur device (S/[S+Se]=0.35), DLCP response at 160 K corresponds to $E_a$ (activation energy) of 0.12 eV while 300 K for 0.25 eV. AS for all three devices indicate defects with characteristics energy between 0.1–0.2 eV; thus our range of profiling spans the energy response of these defects at all three absorber compositions. The charge density was determined by the

78

relevant relation described in literature, [4-20] as shown in Figure 4-4 (the horizontal axis is $<x> = \varepsilon A/C_0$ , the average location away from p-n junction where charges response to AC signal, where $C_0$ is from a quadratic fit of measured capacitance $dQ/dV$ , $\varepsilon$ is the permittivity of the CZTSSe absorber layer, [4-21] and $A$ is the device area = 0.12 cm$^2$).

Because of the high n-type doping concentration of the CdS layer, we assumed that the entire depletion region is mainly in the CZTSSe absorber layer. Therefore $N_{DL,}$ measured by DLCP, represents the charge density of the CZTSSe layer. DLCP is capable of observing the response mainly from free carrier and deep defects. At sufficiently low temperatures only free carriers contribute to the DLCP signal. Thus, the difference of $N_{DL}$ between high temperature and low temperature is closely correlated to the defect density in the absorber.[4-14] The $N_{DL}$ points at $V_{dc}= 0$ were chosen to estimate the defect density. The estimated values for each condition are listed in Table 4-2. The high sulfur content device possesses a larger bulk defect density than the low sulfur content one. This trend is consistent with the AS data, where the high sulfur content device exhibited a larger capacitance variation, as a function of frequency.

From the difference between high and low temperature $N_{DL}$, the free carrier density derived from DLCP generally corresponds to the density of fully ionized dopants,[4-14]indicating the dependence of doping concentration on sulfur content as seen Table 4-2. It is known that the semiconductors with high doping concentration have greater recombination, resulting in shorter minority carrier lifetimes as well as shorter diffusion lengths. Thus, the dependence of doping concentration on sulfur content is consistent
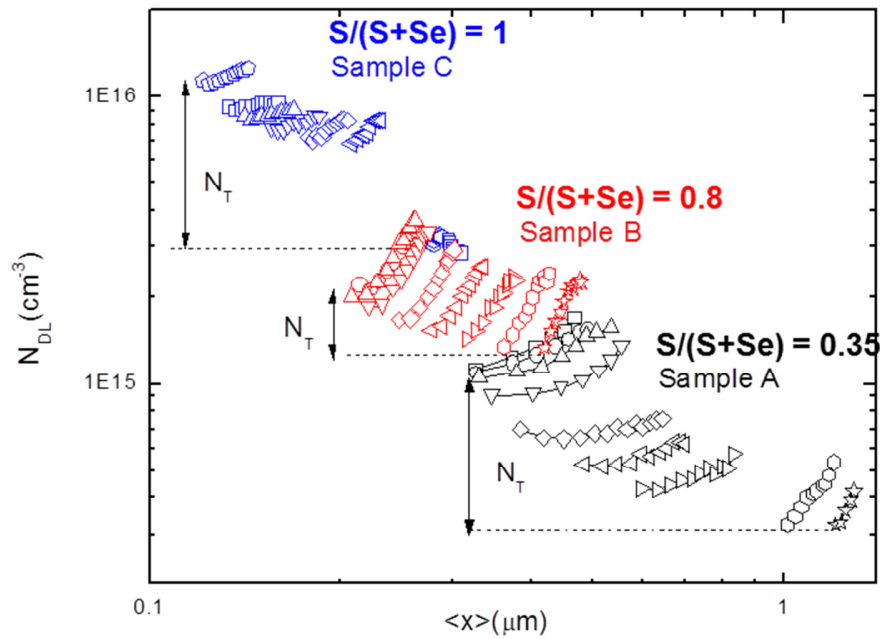
**Figure 4-4**: Drive-Level Capacitance Profiling (DLCP)  response of: various sulfur content devices at different temperatures. The measurement frequency was 11 kHz, the D.C bias range was 0V to -0.5V, and the temperature range was 160K to 300K. In each sample, higher temperature related to larger charge density

**Table 4-2. Summary of resulted derived from DLCP measurements**

| Sample [S]/( [S]+ [Se]) | Free carriers density (cm$^{-3}$) | Trap  density (cm$^{-3}$) | Interface state response (relative values) |
|---|---|---|---|
| A   0.35 | $3.22 \times 10^{14}$ | $8 \times 10^{14}$ | $1.17 \times 10^{16}$ |
| B    0.8 | $1.33 \times 10^{15}$ | $9 \times 10^{14}$ | $1.07 \times 10^{16}$ |
| C    1.0 | $3.15 \times 10^{15}$ | $8.22 \times 10^{15}$ | $1.81 \times 10^{16}$ |

with previous reports showing that CZTSe (almost no sulfur content in the device) has longer carrier lifetime (10 ns) than CZTSSe (low sulfur content, 3 ns).[4-6] The trend of the doping defects also explains the high recombination losses in the high sulfur content device as a result of its high doping concentration. The defect concentration is expected to be a major determinant of open circuit voltage ($V_{oc}$), and the voltage shortfall, $E_g$-$qV_{oc}$, and defect density can be correlated in the relation:[4-15]

$$E_g - qV_{oc} \propto A \ln N \qquad (4.2)$$

The defect density measured from AS (Figure 4-2) and from DLCP (Figure 4-4) both correlate with the voltage shortfall shown in Table 4-1. This correlation shows that the open circuit voltage losses result from high bulk defect concentrations in absorber materials that have higher sulfur content.

## 4.4    CZTS Transistor

Transistor device using a CZTS channel layer make this way would probe the carrier transportation behavior across the film. In addition, the single layer without introducing p-n junction interface, provides an independent information about electronic properties of CZTS layer.

### 4.4.1   CZTS Transistor fabrication

CZTS transistor was fabricated on thermally oxidized silicon substrate with a 300 nm SiO$_2$ film on heavily doped Si using as gate electrode. Si-substrate was cleaned following a 'piranha' process, with hydrogen peroxide:sulfuric acid 1:4 volume ratio. CZTS channel layer was deposited onto substrate using spin coating, dried on a preheated hot plate in glove box with oxygen and moisture level below 1ppm. A final annealing step

with temperature ranged for 400-550 $^{\circ}$C was subjected to the film. Electrode was deposited on to CZTS layer by thermal evaporation using shadow mask. TFTs using ultra-thin channel layer of CZTS films deposited this way have been demonstrated in the architecture shown in **figure 4-5,** using thermally evaporated gold as source and drain electrodes.
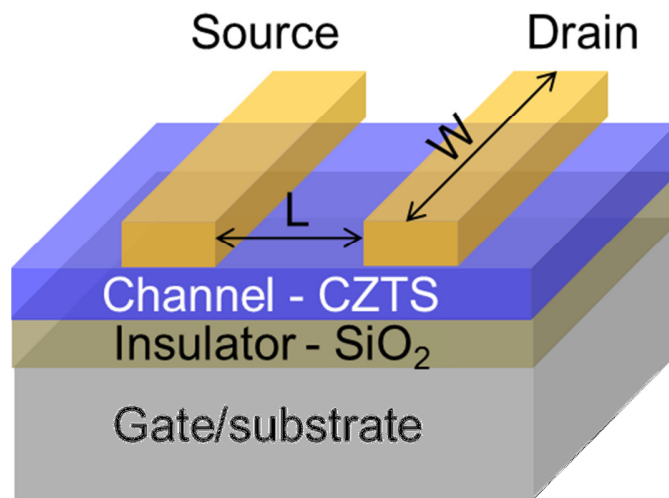


**Figure 4-5** schematic of transistor structure using CZTS film as channel layer, gold as source and drain electrode on SiO2/Si substrates using heavily doped Si as gate terminal.

For AFM and RBS analysis, CZTS thin film samples were deposited on $SiO_2$/Si substrate subjected to 400 $^{\circ}$C annealing. The AFM images were taken using a Nanoscope IIIa (Veeco Instruments) scanning probe microscope, operated in tapping mode with an etched silicon cantilever. RBS spectra was acquired at a backscattering angle of 160$^{\circ}$ and a grazing angle at 110$^{\circ}$, using He$^{++}$ ion beam with the energy of 2.275 MeV. Signal from Zn and Cu atom were differentiated from K-line characteristic X-ray coupled into RBS analysis chamber. Agilent 4155C was employed to measure transistor in atmosphere.

82
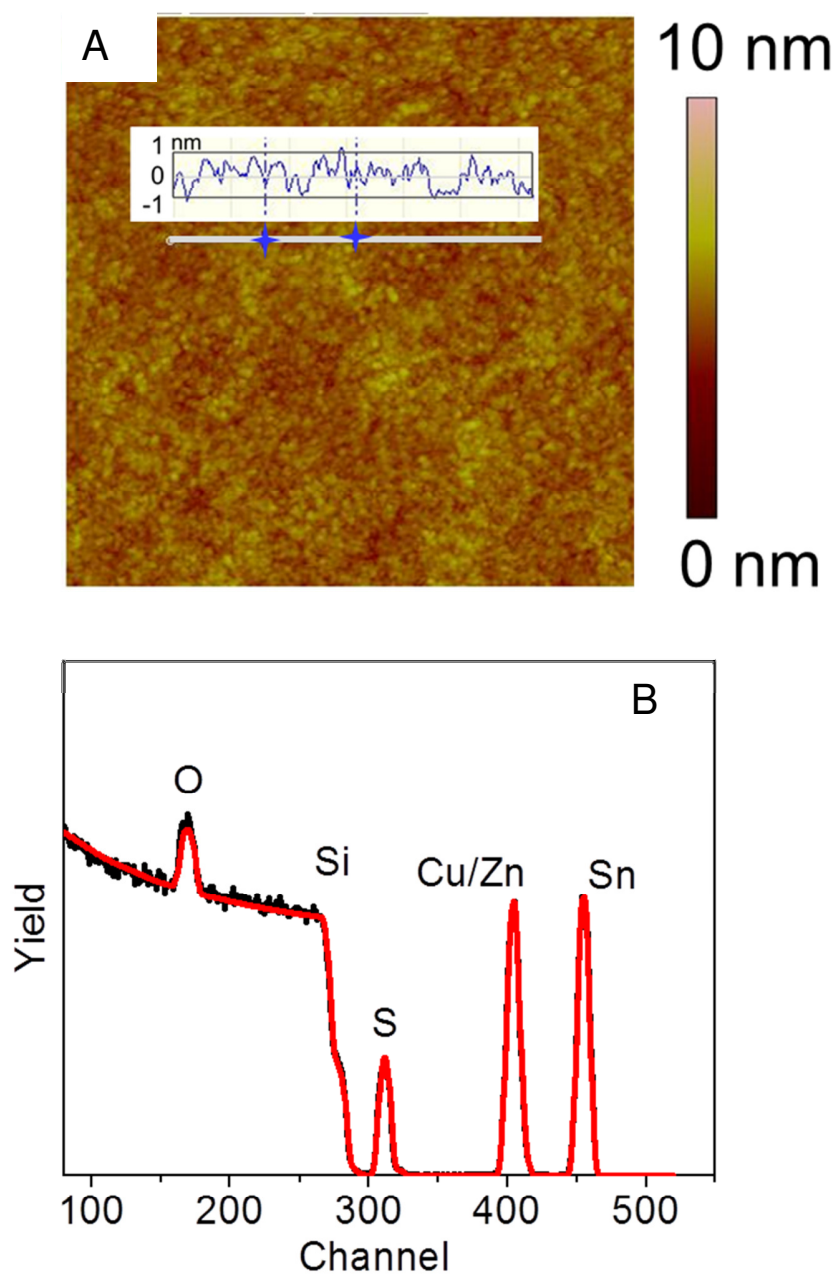
**Figure 4-6**(A) Atomic Force Microscopy (AFM) shows the roughness of less than 2 nm

for CZTS films deposited on Si/SiO$_2$ substrate subjected thermal treatment under 400 $^o$C.

(B) composition analysis on CZTS film by Rutherford Back Scattering (RBS). The

possible impurity of carbon is under the detection limitation of RBS.

The crystalline semiconducting films were spin coated from CZTS molecular precursor solution, which allows the deposition of a continuous smooth film thinner than 10 nm. From atomic force microscope (AFM) in Figure 4-6A, the roughness of the film is within the range of 2nm. The volatile nature of hydrazinium cation and hydrazine derivative enables the formation of chemically clean highly crystalline CZTS phase below $250^{o}$C. Upon 400 $^{o}$C annealing, the chemical composition analysis (Figure 4-6B) on films by RBS indicates negligible carbon impurity left in the resulting films. The demonstrated film uniformity realized from all the components of CZTS phase on the molecular level, enables the deployment of potential scaled-up deposition of large area films on both rigid and flexible substrates at relatively low temperature**.**

### 4.4.2 CZTS electronic properties from transistor device

The representative output of drain current vs drain voltage as a function of applied gate voltage is plotted in Figure 4-7A with a CZTS channel layer. The device functioned as a p-channel transistor, operating at accumulation mode under the field provided by a negative applied gate voltage, while positive gate voltage depletes the channel layer and turns the device off. The current-voltage curve shows typical transistor behavior with a linear $I_d/V_d$ dependence initially and saturated as channel layer was pinched off. A typical transfer curve with the relation of gate bias $V_g$ dependent drain current $I_d$ was shown in Figure 4-7B, indicating an on/off ratio of $10^2$. The relatively low on/off ratio is related to the kesterite CZTS phase which exists only in a very narrow stoichiometric window and small deviations of composition usually generates detrimental secondary phases.[4-16]
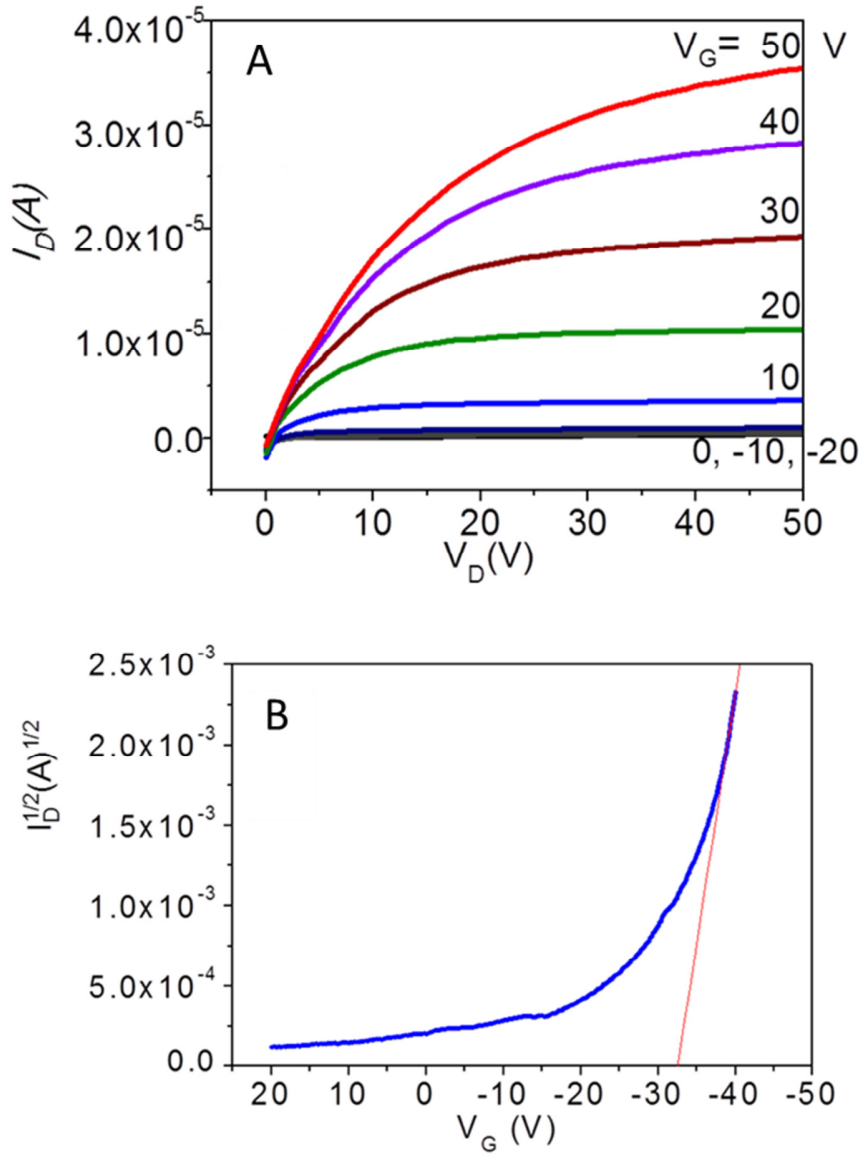
**Figure 4-7.** (A) a typical source drain output of CZTS transistor plotted of $I_{sd}$ (drain current) as a function $V_{sd}$ (drain voltage) when applying different $V_g$ (gate voltage), (B) gate voltage dependent drain current at saturation region ($V_d = 40$ V).

Previously reported mobility and carrier density located in the high range of carrier density ($10^{18}$/cm$^3$) and mobility (beyond $10\ cm^2/(V \cdot s)$) may be partially due to the contribution of resulting impurity phases.[4-17] To exclude possible non-shut off current contributed from impurity conductive phase in the channel layer, the saturation region mobility is calculated from the linear relation of $I_d$ vs $V_g$, yielding the value of $1.3.cm^2/(V \cdot s)$

$$I_D = \frac{\mu}{2} C_{ox} \frac{W}{L} \left(V_g - V_{th}\right)^2$$
(4.3)

The mobility of CZTS is comparable with CISS materials processed using similar hydrazine deposition.[4-18] It is thus demonstrated that CZTS materials have intrinsic properties comparable to chalcopyrite CISS materials, indicating the strong potential toward higher performance for PV devices.
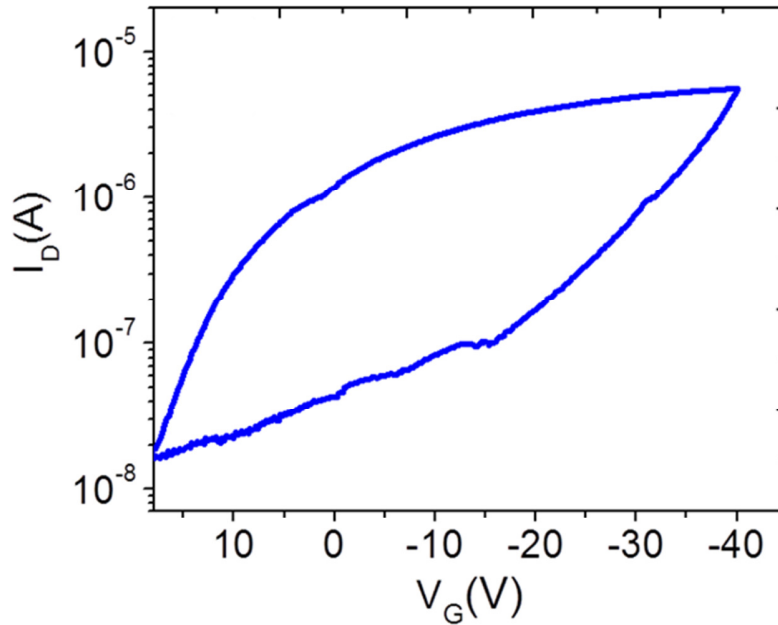


**Figure 4-8** Hysteresis effect of CZTS channel layer based transistor.

The hysteresis effect shown in Figure 4-8, normally found in polycrystalline thin films but extremely obvious in the CZTS system, suggest a large number of hole traps at grain boundaries and interfaces between the channel layer and substrate or electrode. The current problem limiting the transistor performance is analogue with the large $V_{oc}$ deficit in CZTS solar cells mainly caused by dominant interface recombination and/or sub-band defects status. Future work to passivate electrically active defects at the grain boundary or interface, such as introducing potential elements from the convenient precursor solution processing platform, is expected to further advance the property of CZTS material system. The defects engineering to minimize the hysteresis effect and optimize transistor behavior would also be critical to inspire the breakthrough on photovoltaic performance catching up its analogue CIGS materials system.

**Reference**

[4-1]  T. K. Todorov, J. Tang, S. Bag, O. Gunawan, T. Gokmen, Y. Zhu, D. B. Mitzi, *Advanced Energy Materials* **2012**, n/a–n/a.

[4-2]  W. Yang, H.-S. Duan, B. Bob, H. Zhou, B. Lei, C.-H. Chung, S.-H. Li, W. W. Hou, Y. Yang, *Advanced materials (Deerfield Beach, Fla.)* **2012**, *24*, 6323–6329.

[4-3]  I. Repins, C. Beall, N. Vora, C. DeHart, D. Kuciauskas, P. Dippo, B. To, J. Mann, W.-C. Hsu, A. Goodrich, R. Noufi, *Solar Energy Materials and Solar Cells* **2012**, *101*, 154–159.

[4-4]  Q. Guo, G. M. Ford, W.-C. Yang, B. C. Walker, E. a Stach, H. W. Hillhouse, R. Agrawal, *Journal of the American Chemical Society* **2010**, 17384–17386.

[4-5]  Y. Cao, M. S. Denny, J. V Caspar, W. E. Farneth, Q. Guo, A. S. Ionkin, L. K. Johnson, M. Lu, I. Malajovich, D. Radu, H. D. Rosenfeld, K. R. Choudhury, W. Wu, *Journal of the American Chemical Society* **2012**, *134*, 15644–7.

[4-6]  S. Bag, O. Gunawan, T. Gokmen, Y. Zhu, T. K. Todorov, D. B. Mitzi, *Energy & Environmental Science* **2012**, *5*, 7060.

[4-7]  I. Repins, N. Vora, C. Beall, S. Wei, Y. Yan, M. Romero, G. Teeter, H. Du, B. To, M. Young, **2011**.

[4-8]  D. B. Mitzi, O. Gunawan, T. K. Todorov, K. Wang, S. Guha, *Solar Energy Materials* **2011**, *95*, 1421–1436.

[4-9]  W. Yang, H.-S. Duan, B. Bob, H. Zhou, B. Lei, C.-H. Chung, S.-H. Li, Y. Yang, *Advanced Materials* **2012**, DOI 10.1002/adma.201201785.

[4-10] T. Walter, R. Herberholz, C. Müller, H. W. Schock, *Journal of Applied Physics* **1996**, *80*, 4411.

[4-11] L. C. Kimerling, *Journal of Applied Physics* **1974**, *45*, 1839–1845.

[4-12] O. Gunawan, T. Gokmen, C. W. Warren, J. D. Cohen, K. Teodor, D. A. R. Barkhouse, S. Bag, J. Tang, B. Shin, D. B. Mitzi, *Applied Physics Letters* **2012**, *253905*, 14–17.

[4-13] J. Lee, J. D. Cohen, W. N. Shafarman, *Thin Solid Films* **2005**, *480-481*, 336–340.

[4-14] J. T. Heath, J. D. Cohen, W. N. Shafarman, *Journal of Applied Physics* **2004**, *95*, 1000–1010.

[4-15] G. Hanna, A. Jasenek, U. Rau, H. W. Schock, *physica status solidi (a)* **2000**, *179*, R7–R8.

[4-16] S. Chen, J.-H. Yang, X. G. Gong, A. Walsh, S.-H. Wei, *Physical Review B* **2010**, *81*, 245204–.

[4-17] D. B. Mitzi, O. Gunawan, T. K. Todorov, K. Wang, S. Guha, *Solar Energy Materials and Solar Cells* **2011**, *95*, 1421–1436.

[4-18] D. J. Milliron, D. B. Mitzi, M. Copel, C. E. Murray, *Chemistry of Materials* **2006**, *18*, 587–590.

[4-20] J. T. Heath , J. D. Cohen , W. N. Shafarman , *J. Appl. Phys.* **2004** , *95* , 1000 .

[4-21] H. Zhao , C. Persson , *Thin Solid Films* **2011** , *519* , 7508 – 7512 .

# Chapter 5 Solution Chemistry for molecular solution processing

## 5.1    Introduction

Successful implementation of molecular solution processing from a homogeneous and stable precursor system would provide a robust approach for the processing of semiconducting multinary compounds. The controllable deposition of chemically pure, high-quality crystalline films requires careful molecular structure design and solvent selection with regard to both precursor solubility and the presence of possible impurities. Hydrazine ($N_2H_4$) serves as a unique and powerful medium, particularly for the incorporation of selected metals and chalcogens into stable solutions as metal chalcogenide complexes (MCCs),[5-1 to 5-5] which are homogeneous down to a molecular level. However, not all elements and compounds can be easily dissolved in this manner.[5-5 to 5-7] In this manuscript, we demonstrate a method to incorporate previously insoluble transition metal elements into molecular solution as hydrazine derivative complexes. The viability of this technique is demonstrated by the synthesis of $Zn(NH_2NHCOO)_2(N_2H_4)_2$ molecules in solution from a metallic zinc precursor. Investigation into the evolution of the resulting molecular structures reveals a potential roadmap to significantly enrich the variety of building blocks suitable for creating soluble molecules. The new molecular structures will ideally serve as archetypes for the solvation of other elements of interest, and ultimately initiate the widespread use of molecular solutions to tremendously simplify the processing of multinary compounds.

The solution processing of kesterite materials has drawn significant research interest because of its potential for the low cost, high throughput production of high quality

films.[5-8] The use of metal salts (e.g. chlorides and nitrates) can be considered one of the easiest and most intuitive ways to introduce the various constituent elements into a CZTS precursor solution, since these salts offer good solubility in water and alcohol.[5-9,5-10] The synthesis of binary, ternary, or even quaternary nanoparticles enables a variety of synthetic approaches to control composition and phase formation without involving high temperature (>500 $^{o}$C) reaction conditions, above which the CZTS phase tends to decompose.[5-11 to 5-14] Unfortunately, nanoparticle-based approaches generally cannot avoid impurities in the form of long-chain carbon ligands that stabilize the NC-based inks used to deposit uniform films over large areas.

Fully soluble metal chalcogenide complexes such as $[Sn_2S_6]^{4-}$, usually prepared from metal sulfide precursors dissolved in hydrazine in the presence of excess chalcogen, may open the door for chemically clean precursor systems without introducing unnecessary impurities.[5-15 to 5-17] Since the introduction of molecular solution approaches involving MCCs, high quality semiconducting films have been achieved for a variety of chalcogenide materials. For example, solar cells with CIGS absorbers deposited from molecular solutions of MCC precursors have yielded the highest performance of any purely solution-based CIGS deposition technique, with a power conversion efficiency of 15.2 %.[5-18,5-19] Currently, no one has been able to design Zn-based MCC structures that are sufficiently soluble in hydrazine-based solutions. As a result, mixed slurries containing nanoparticles of hydrazinium zinc chalcogenide and soluble MCCs of the Cu- and Sn-constituents are used as a compromise when zinc species are required. This technique currently holds the most successful solution based approach to fabricate

90

kesterite CZTS photovoltaic devices, with a reported efficiency of 11.1%.[5-7,5-20,5-21] However, the formation of the slurry is highly sensitive to processing conditions and the stability of the MCC-ligands and particle systems have not yet been fully addressed.

A fully dissolved homogenous molecular solution capable of yielding chemically pure films is the most simple and effective way to process films of a multinary system, as each elemental component is independently adjustable to fully control both composition and phase. However, the limited solubility of zinc-based materials constrains this concept to only a few materials, excluding Zn/ZnS/ZnSe and other transition metal chalcogenides of interest. We have previously demonstrated a method for forming solution processed CZTS with a fully soluble zinc constituent using hydrazine derivatives (HDs).[5-22] To fully understand the underlying mechanism and in hopes of expanding its applications to other material systems, we investigated the evolution of the Zinc-HD molecular structures during the dissolution process, the stability of the resulting solutions, and the phase evolution that occurs as the Cu-, Sn-, and Zn- constituents react to form kesterite CZTS. The identification of the molecular structure of the newly soluble zinc species will hopefully serves as a guideline to form stable molecular solutions of a variety of other elements of interest and to explore compatible solvents beyond hydrazine.

## 5.2    Molecular structure identification

By introducing carbon dioxide into hydrazine, the zinc constituent was fully dissolved in a tin sulfide solution in hydrazine containing excess sulfur. Figure 5-1A shows the Zn/Sn precursor solution containing the Zn- and Sn- constituents. To form the solution,

elemental zinc was combined with hydrazinocarboxylic (hyc) acid in hydrazine. Some

bubbling is generally observed upon the mixing of the reactants. The metallic zinc lattice

was dismantled and chelated by $NH_2NHCOO^-$ through the following reaction:

$$Zn + NH_2NHCOOH \rightarrow [Zn(NH_2NHCOO)_3] + H_2\,(g) \quad (1)$$
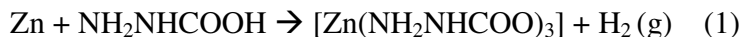
To investigate the resulting molecular structure, a crystal was grown from the Zn and

$NH_2NHCOOH$ species in an $H_2O$ based solution by slowly evaporating the solvent until

the concentration saturated and precipitation began. Figure 5-1B shows the molecular

structure of the observed $Zn(hyc)_3$ structure as resolved by single crystal X-ray

crystallography. In this structure, the zinc atom is chelated by three hyc bidentate ligands

through Zn-N and Zn-O bonding interactions. The resulting negatively charged ionic

complex is electrically neutralized by nearby hydrazinium cations $N_2H_5^+$, and the solvent

molecule $H_2O$ does not chemically bond to the zinc atom, but acts as a neutral spacer

between neighboring complexes. The $Zn(hyc)_3$ complex, shown in Figure 5-1B, still

exhibits limited solubility in hydrazine, existing as a white paste even after extended

stirring. It was discovered that adding the tin chalcogenide complex $[Sn_2S_6]^{4-}$ (1 mmol)

and excess sulfur (0.5 mmol) to the chelated zinc paste (1 mmol) greatly improves the

solubility, forming the mixed Zn/Sn precursor that is used extensively in this study.

$$[Zn(NH_2NHCOO)_3]^- + [Sn_2S_6]^{4-} + S + N_2H_4$$

$$\rightarrow Zn(NH_2NHCOO)_2(N_2H_4)_2 + [Sn_2S_7]^{6-} \qquad (2)$$
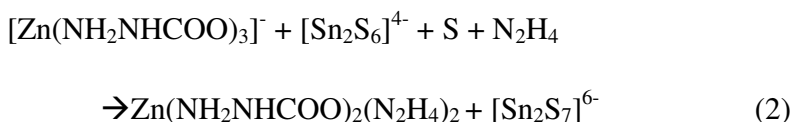
To ascertain the molecular structure of the newly soluble compound, X-ray

crystallography was applied to analyze a crystal grown from the completed Zn/Sn

solution, as shown in Figure 5-1C. The crystal was obtained by slowly diffusing $H_2O$
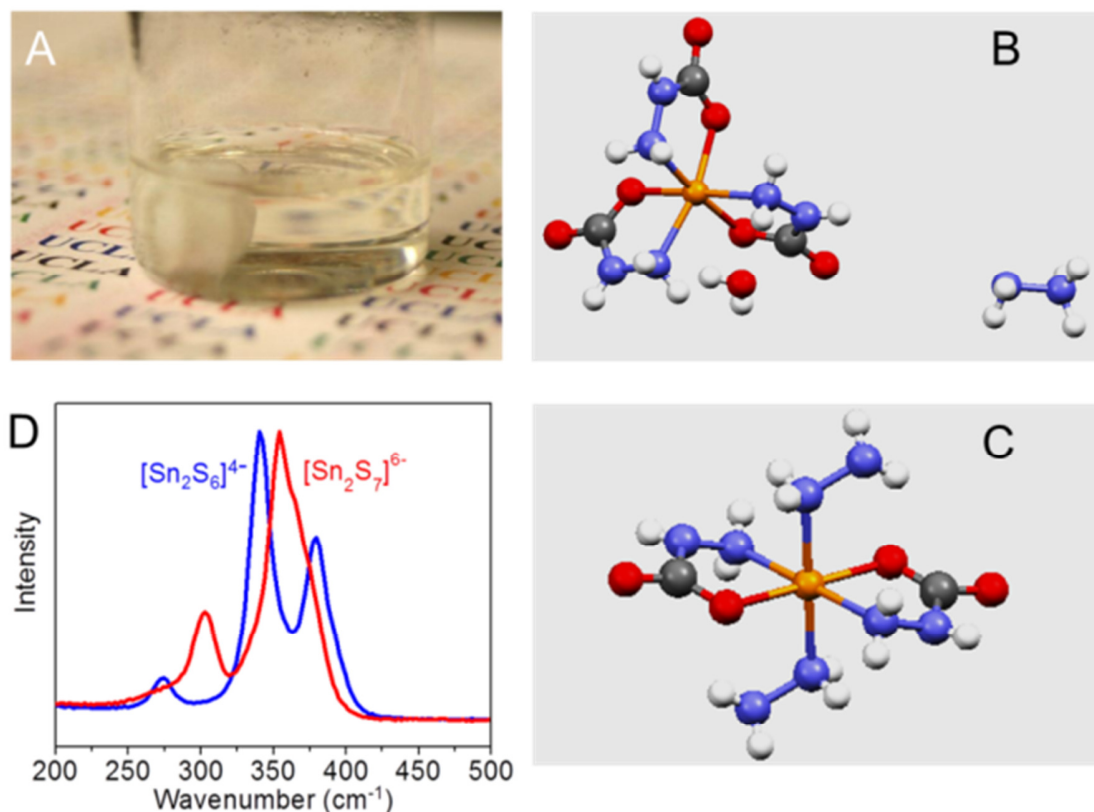
Figure 5-1. (A) Zn/Sn solution in hydrazine, obtained by combining the zinc precursor produced by reacting metallic zinc, hydrazinocarboxylic acid and one equivalent of $SnS_2$ dissolved in hydrazine in the presence of extra sulfur. (B) The crystal structure of $N_2H_5[Zn(NH_2NHCOO)_3] \cdot H_2O$ derived from the reaction of Zn and $NH_2NHCOOH$ in water. (C) The crystal structure of $Zn(NH_2NHCOO)_2(N_2H_4)_2$, the soluble zinc complex present in the Zn/Sn solution in Figure 5-1A. (D) Solution phase Raman spectroscopy of the various Sn-S species present in the $SnS_2$ and Zn/Sn solutions.

vapor into the Zn/Sn solution in a sealed vial. In this structure, the zinc atom is chelated by two $NH_2NHCOOH$ and $NH_2NH_2$ molecules. The incorporation of hydrazine into the original zinc complex forms $Zn(NH_2NHCOO)_2(N_2H_4)_2$, which exhibits greatly improved solubility compared to $Zn(hyc)_3$.

The evolution of the primary tin species from $[Sn_2S_6]^{4-}$ to a more sulfur rich structure during the reaction was revealed by Raman spectroscopy of the molecular species in solution, as shown in figure 5-1D. Before mixing with the Zn-constituent, the Sn-solution with the molecular structure of $[Sn_2S_6]^{4-}$ shows the bridging mode (Sn-S-Sn) and stretching mode at 344 cm$^{-1}$ and 367 cm$^{-1}$ respectively, as well as the $Sn_2S_2$ ring vibration mode at 280 cm$^{-1}$.[5-25] In the mixed Zn/Sn solution, the disappearance of the $Sn_2S_2$ ring vibration mode at 280 cm$^{-1}$ and the appearance of peaks around 300 cm$^{-1}$ and 351 cm$^{-1}$ suggest that excess sulfur terminates the symmetric Sn-S-Sn bridges in $Sn_2S_6$ to generate new bridge vibrations in the $S_3Sn–S–SnS_3$ and $SnS_4$ stretching modes located around 348 cm$^{-1}$.[5-26,5-27] Gradually increasing the amount of sulfur in the Zn/Sn solution leads to relatively stronger signal around 350 cm$^{-1}$, showing an increasing portion of $SnS_4$ character in the Sn-S complexes.[5-27]

Sulfur ligands produced by the reaction of extra sulfur with hydrazine likely initiated the change of coordination in the Zn-complex to generate intermediate zinc-species. Both $NH_2NHCOOH$ and $N_2H_4$ molecules can function as the ligands chelating the central zinc atom via Zn-N bonds. Possibly through an entropically favorable ligand replacement and dissolution process, $Zn(hyc)_3$ evolves into the soluble form $Zn(hyc)_2(N_2H_4)_2$. Thus, the

Zn/Sn solution in Figure 5-1A has the soluble complex $Zn(hyc)_2(N_2H_4)_2$ coexisting with multiple Sn-S species in equilibrium, including $[Sn_2S_7]$ and $[SnS_4]$, as determined by the amount of extra sulfur present in the solution. Thus, the zinc constituent is incorporated into $N_2H_4$-based solutions with greatly enhanced solubility through chelation by two hydrazine molecules. This model, demonstrated in the case of zinc, to form both HD and $N_2H_4$ chelated complexes, is expected to provide a universal route to potentially incorporate previously insoluble elements into hydrazine and other solvents.

## 5.3    Solution stability

The as-prepared colorless Zn/Sn solution was stable for several months in an inert atmosphere. The zinc compound remained stable until the chemical environment was changed by introducing S-ligands. It was observed that the addition of excess sulfur into the Zn/Sn solution, beyond what is required to produce the soluble $Zn(hyc)_2(N_2H_4)_2$ complex (Figure 5-1A) generates precipitation within several days. In the case of stable Zn/Sn solutions, no S-H Raman signal is detectable at its characteristic peak position of 2560 cm$^{-1}$. As shown in Figure 5-2A, the introduction of 1 mmol excess S into 1 ml Zn/Sn solution forms $(N_2H_5)HS$ or $((N_2H_5)_2S$, which is indicated by a strong S-H Raman signal.[5-5] The appearance of S-ligands in the system appears to dramatically modify the coordination of the zinc atom. The formation of thermodynamically favorable Zn-S bonds tends to strip the coordinated ligands of hyc and hydrazine by overcoming the previously dominant Zn-N and Zn-O bonding interactions.

$Zn(NH_2NHCOO)_2(N_2H_4)_2 + SH[N_2H_5]$

$$\rightarrow ZnS + N_2H_4 + NH_2NHCOOH \qquad (3)$$
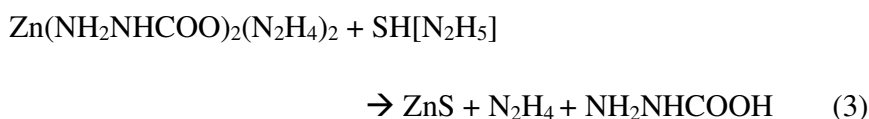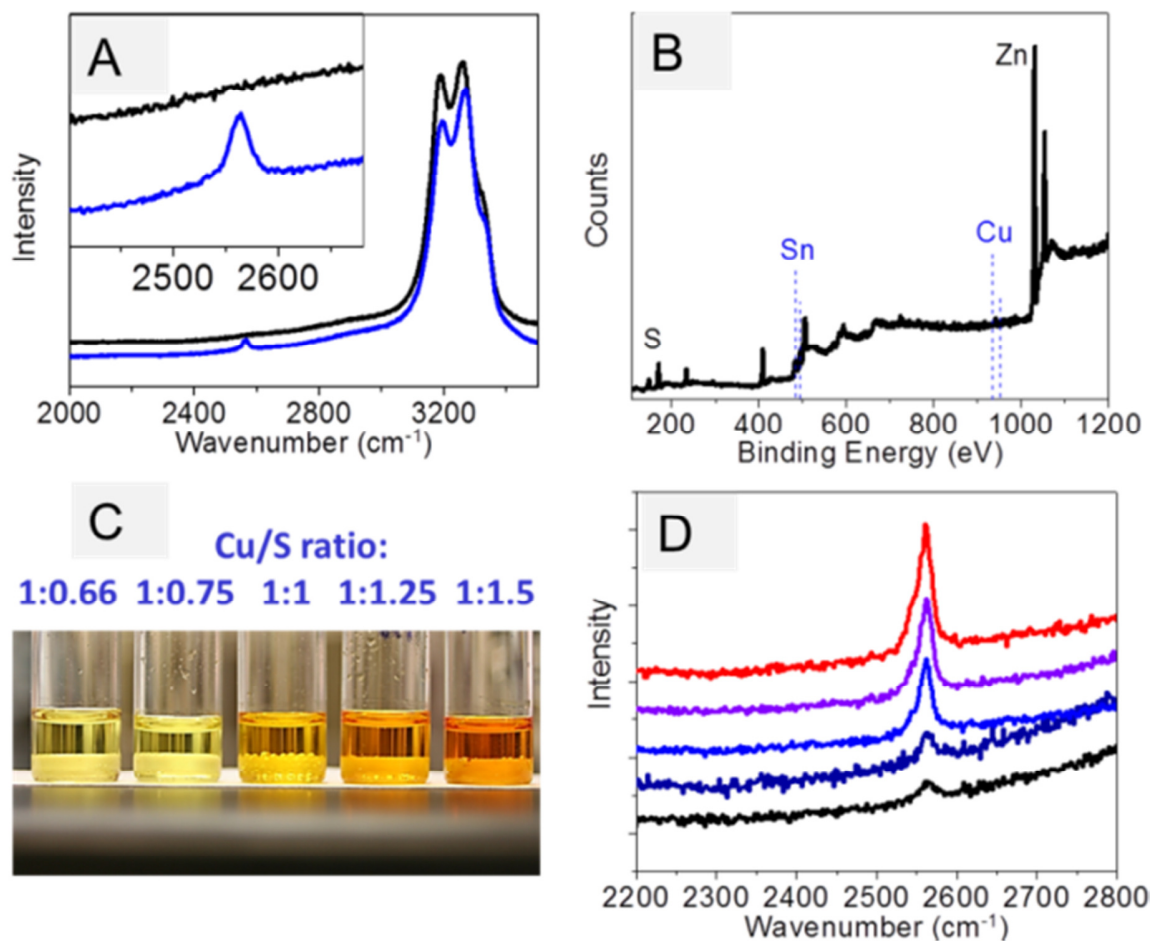
Figure 5-2. (A) Raman spectroscopy of the Zn/Sn solution shown in Figure 5-1A. Incorporating extra sulfur leads to the formation of S-ligands, which produce a strong Raman signal at 2560 cm$^{-1}$. (B) XPS results of precipitation formed adding excess S into the Zn/Sn solution. (C) Cu-precursor solutions with a series of different Cu:S ratios from 1:1.5 to 1:0.75. (D) Raman spectroscopy on the Cu-precursors showing the varying intensity of the signal from S-ligands in solution.

Compositional analysis by XPS (Figure 5-2B) shows that the S-ligands destroy the stability of the zinc complex, forming ZnS precipitation within 1 day at room temperature. This behavior is consistent with the mostly insoluble nature of ZnS, which does not dissolve even in hydrazine solutions containing excess sulfur.[5-28]

The effect of sulfur ligands on the stability of the final CZTS precursor solution has also been verified by mixing the Zn/Sn precursor solution with a series of Cu-S-$N_2H_4$ solutions with decreasing S/Cu ratios. Figure 5-2C shows the freshly made Cu-constituent solutions: the color shift from yellow to brown is attributed to absorption from the increasing amounts of excess sulfur dissolved in hydrazine solution. The normalized S-H vibration signal from the solution-phase Raman spectrum at 2560 cm$^{-1}$ (Figure 5-2D) reveals a reduced presence of S-ligands at lower concentrations of excess sulfur in solution. When mixing the Zn/Sn solution with a S-rich Cu-constituent (S:Cu~1.5), obvious precipitation of ZnS was observed after several hours. Compositional analysis by XPS on the precipitates shows strong Zn and S signal and a near complete absence of Sn- and Cu-signal (Figure 5-2B). The completed mixtures of Zn/Sn solutions with a Cu-constituent containing the sulfur to copper ratio of S/Cu~0.75, with a barely visible S-H signal under Raman spectroscopy, are stable for several weeks without obvious aggregation. This indicates that the Zn-complex can easily coexist with the Cu-constituent in the form of $[Cu_6S_4]^{4-}$. The observed stability collapse in the mixed CZTS precursor solution behaves similarly to that of the Zn/Sn solution with extra sulfur. Therefore, in order to achieve stable multinary molecular solutions, the incorporation of

any excess S-ligands should be avoided when employing metallic complexes with hydrazine or hydrazine derivative ligands.

Molecular solution processing provides a useful platform to further examine the mechanism of transformation from precursor solution to solid film. Compared with the solid state reaction routes that convert binary phases into CZTS, which occur in both hydrazine slurries and in thermal evaporation, the molecular solution produces the final phase from individual molecules in a single step. The completed CZTS precursor solution has the flexibility to realize compositional control by varying the ratio of each constituent solution during preparation. The partial chelation of the zinc complex by easily volatilized hydrazine molecules results in a very low thermal barrier to trigger the release of the central zinc atom. The $Zn(hyc)_3$ complex decomposes into metal and metal oxide powder at temperatures above 500 $^o$C, with a major endothermic reaction at around 200 $^o$C.[5-23, 5-24] In contrast, the CZTS precursor containing the hydrazine coordinated Zn-complex shows near-complete decomposition with exothermic behavior at around 160 $^o$C, as shown in Figure 5-3C. The exothermic process is partially due to the incorporation of the hydrazine molecule onto the zinc atom, and formation of the hydrazinium species from the Cu- and Sn-components.[5-3] The dissociation and decomposition of hydrazinium/hydrazine species has been generally shown to release heat in the process, as exemplified by $[N_2H_5]_4[Sn_2S_6]$ and other compounds.[5-2]

98
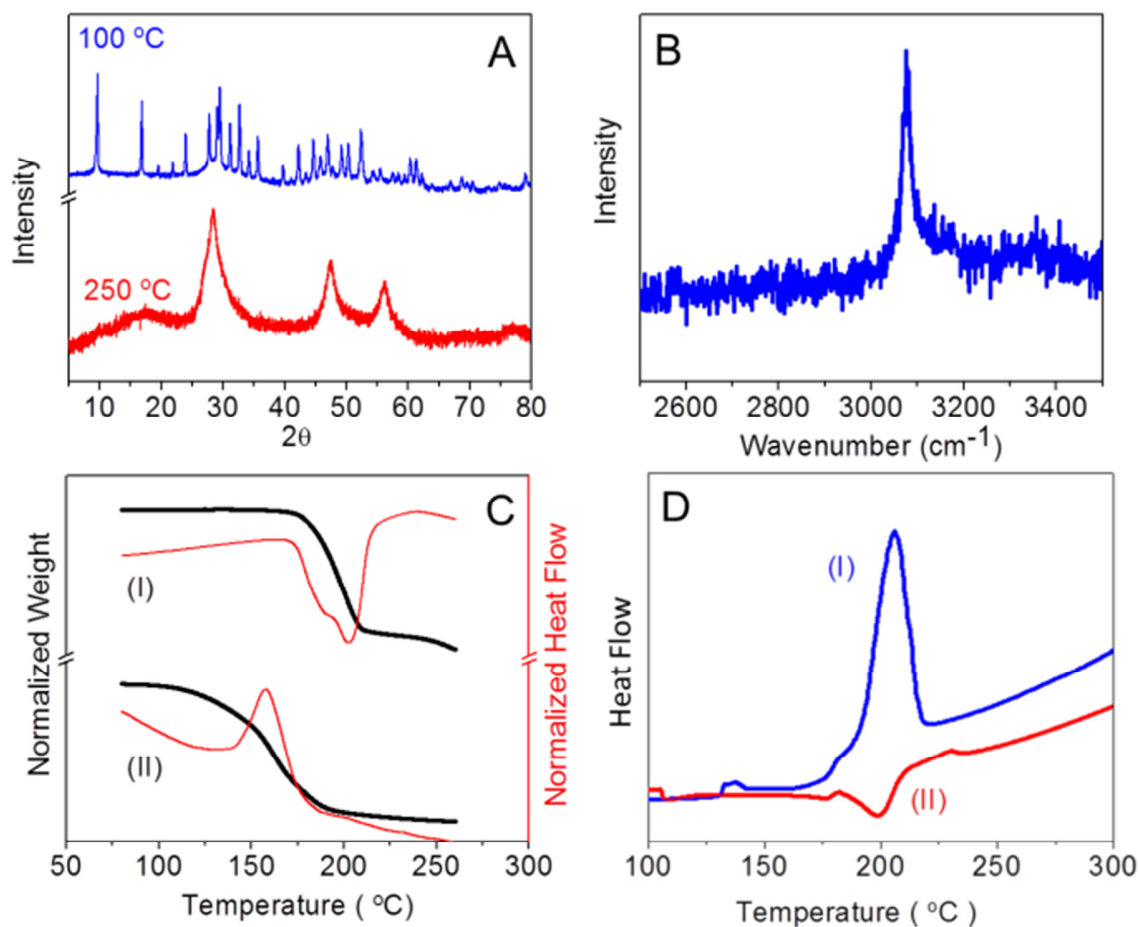
Figure 5-3. The reaction path from molecular precursor to kesterite CZTS phase. (A) X-ray diffraction patterns for CZTS precursors annealed at 100 $^o$C and 250 $^o$C. (B) Raman spectrum of the CZTS precursor at 100 $^o$C showing only the N-H vibration mode. (C) Thermogravimetric analysis (TGA) on (I) Zn(hyc)$_3$, showing the endothermic reaction around 200 $^o$C, and (II) CZTS precursor progressing toward the kesterite phase with an exothermic decomposition step around 150 $^o$C. (D) Differential scanning calorimetry analysis on the Zn(hyc)$_3$ and CZTS precursors.

Another possible route is provided by the chemical modification of the Zn complex by sulfur ligands. While extra S-ligands tend to disturb the stability of the solution system, careful control of the S-ligands during film processing also provides a self-cleaning procedure to chemically strip any remaining hyc ligands from the zinc atoms present. Differential scanning calorimetry analysis on the $Zn(hyc)_3$ and CZTS precursors (Figure 5-3D) also shows exothermic behavior from the zinc complexes with hydrazine ligands, suggesting that the evolution from $Zn(hyc)_3$ to the more reactive Zn-species $Zn-S-(N_2H_4)$ may provide a more favorable thermal decomposition route for the chelated zinc system. Therefore, rather than relying on the thermal decomposition of the Zn-complex, sulfur ligands also provide a chemical route to extract zinc from its precursor complex by replacing the coordinating ligands. As a result, the homogeneously released zinc constituent reacts with the Sn- and Cu-MCC molecular species, contributing to the kinetically favorable reaction path to form the CZTS phase [5-22] at temperatures around $200\ ^oC$ without involving any long-range diffusion process.

$$[Cu_6S_4]^{2-} + Zn[NH_2NHCOO]_2[N_2H_4]_2 + [Sn_2S_6]^{4-} + S + N_2H_5^{+}$$

$$\xrightarrow{T} CZTS + \text{volatile species } (N_2H_4, CO_2) \qquad (4)$$
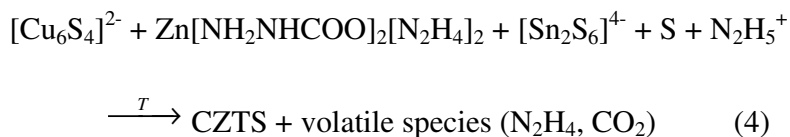
The released $NH_2NHCOOH$ molecules become gaseous species around $160\ ^oC$, much lower than the decomposition temperature of the coordinated form. Further annealing up to $250\ ^oC$ leads to the dissociation of hydrazine and its derivatives into volatile species ($CO_2$, hydrazine, ammonia, etc.).[5-1] Phase characterization of the product by XRD further verifies the proposed dissociation of the spacer molecules. The strong diffraction peak at $8^o$ in Figure 5-3A, obtained from the powder produced by evaporating the solvent

from a CZTS precursor solution, indicates a large d-spacing possibly separated by $N_2H_5^+$ and $N_2H_4$ molecules, which agrees well with peaks observed in other hydrazinium compounds.[5-29] The N-H stretching signal from the Raman spectrum (Figure 5-3B) also suggests the existence of $N_2H_5^+$/$N_2H_4$ spacers.[5-2,5-30] The disappearance of the N-H signal upon an intermediate heat treatment of 250 $^o$C is in agreement with the simple thermal decomposition step from the hydrazinium complex to the metal chalcogenide product. The molecular solution process exhibits the capability to produce single phase and chemically pure films, and may prove a valuable tool for enabling the correlation of material properties and optoelectronic performance.

**Reference**

[5-1]  M. Yuan, D. B. Mitzi, *Dalton transactions (Cambridge, England : 2003)* **2009**, 6078–88.

[5-2]  E. W. Schmidt, *Hydrazine and Its Derivatives : Preparation, Properties, Applications (2 Volume Set)*, Wiley-Interscience, **2001**.

[5-3]  D. B. Mitzi, L. L. Kosbar, C. E. Murray, M. Copel, A. Afzali, *Nature* **2004**, *428*, 299–303.

[5-4]  D. J. Milliron, S. Raoux, R. M. Shelby, J. Jordan-Sweet, *Nature materials* **2007**, *6*, 352–6.

[5-5]  C.-H. Chung, S.-H. Li, B. Lei, W. Yang, W. W. Hou, B. Bob, Y. Yang, *Chemistry of Materials* **2011**, *23*, 964–969.

[5-6]  T. Todorov, D. B. Mitzi, *European Journal of Inorganic Chemistry* **2010**, *2010*, 17–28.

[5-7]  T. K. Todorov, K. B. Reuter, D. B. Mitzi, *Advanced materials (Deerfield Beach, Fla.)* **2010**, *22*, E156–9.

[5-8]  D. B. Mitzi, O. Gunawan, T. K. Todorov, K. Wang, S. Guha, *Solar Energy Materials and Solar Cells* **2011**, *95*, 1421–1436.

[5-9]  C. J. Hibberd, E. Chassaing, W. Liu, D. B. Mitzi, D. Lincot, a. N. Tiwari, *Progress in Photovoltaics: Research and Applications* **2010**, *18*, 434–452.

[5-10] W. Ki, H. W. Hillhouse, *Advanced Energy Materials* **2011**, *1*, 732–735.

[5-11] Y. Cao, M. S. Denny, J. V Caspar, W. E. Farneth, Q. Guo, A. S. Ionkin, L. K. Johnson, M. Lu, I. Malajovich, D. Radu, H. D. Rosenfeld, K. R. Choudhury, W. Wu, *Journal of the American Chemical Society* **2012**, *134*, 15644–7.

[5-12] Q. Guo, G. M. Ford, W.-C. Yang, B. C. Walker, E. a Stach, H. W. Hillhouse, R. Agrawal, *Journal of the American Chemical Society* **2010**, 17384–17386.

[5-13] Q. Guo, H. W. Hillhouse, R. Agrawal, *Journal of the American Chemical Society* **2009**, *131*, 11672–3.

[5-14] C. Steinhagen, M. G. Panthani, V. Akhavan, B. Goodfellow, B. Koo, B. A. Korgel, *Journal of the American Chemical Society* **2009**, *131*, 12554–5.

[5-15] M. V Kovalenko, M. Scheele, D. V Talapin, *Science (New York, N.Y.)* **2009**, *324*, 1417–20.

[5-16] C. Jiang, J.-S. Lee, D. V Talapin, *Journal of the American Chemical Society* **2012**, *134*, 5010–3.

[5-17] M. V Kovalenko, M. I. Bodnarchuk, J. Zaumseil, J.-S. Lee, D. V Talapin, *Journal of the American Chemical Society* **2010**, *132*, 10085–92.

[5-18] T. K. Todorov, O. Gunawan, T. Gokmen, D. B. Mitzi, *Progress in Photovoltaics: Research and Applications* **2012**, *21*, 82–87.

[5-19] D. B. Mitzi, M. Copel, C. E. Murray, *Advanced Materials* **2006**, *18*, 2448–2452.

[5-20] S. Bag, O. Gunawan, T. Gokmen, Y. Zhu, T. K. Todorov, D. B. Mitzi, *Energy & Environmental Science* **2012**, *5*, 7060.

[5-21] T. K. Todorov, J. Tang, S. Bag, O. Gunawan, T. Gokmen, Y. Zhu, D. B. Mitzi, *Advanced Energy Materials* **2012**, *3*, 34–38.

[5-22] W. Yang, H.-S. Duan, B. Bob, H. Zhou, B. Lei, C.-H. Chung, S.-H. Li, W. W. Hou, Y. Yang, *Advanced materials (Deerfield Beach, Fla.)* **2012**, *24*, 6323–6329.

[5-23] B. N. Sivasankar, S. Govindarajan, *Journal of Thermal Analysis* **1996**, *46*, 117–127.

[5-24] B. Novosel , J. Macek, *Journal of Thermal Analysis* **1993**, *40*, 427–435.

[5-25] N. Pienack, S. Lehmann, H. Lühmann, M. El-Madani, C. Näther, W. Bensch, *Zeitschrift für anorganische und allgemeine Chemie* **2008**, *634*, 2323–2329.

[5-26] D. S. Von Nasn, W. Schlwy, *Z. anorg. allg. chem.* **1973**, *398*, 63–71.

[5-27] J. Campbell, D. P. DiCiommo, H. P. A. Mercier, A. M. Pirani, G. J. Schrobilgen, M. Willuhn, *Inorganic Chemistry* **1995**, *34*, 6265–6272.

[5-28] D. B. Mitzi, T. K. Todorov, O. Gunawan, M. Yuan, Q. Cao, W. Liu, K. B. Reuter, M. Kuwahara, K. Misumi, A. J. Kellock, S. J. Chey, T. G. de Monsabert, A. Prabhakar, V. Deline, K. E. Fogel, in *2010 35th IEEE Photovoltaic Specialists Conference*, IEEE, **2010**, pp. 000640–000645.

[5-29] W.-C. Hsu, B. Bob, W. Yang, C.-H. Chung, Y. Yang, *Energy & Environmental Science* **2012**, *5*, 8564.

[5-30] J. R. Durig, *The Journal of Chemical Physics* **1966**, *44*, 4238.

# Chapter 6 Summary

Photovoltaic technology, devices that convert sunlight directly into electricity, is recognized as one of the most promising renewable energy sources capable of powering a sustainable future. Metal chalcogenide-based thin film solar cells are currently regarded as the most viable candidates for the future large scale production of solar energy because of opportunities to produce them in a cost-effective way at scales needed to meet energy demands. The solution process as describe in previous chapters is critical to extend the commercial potential of CIGS by reducing manufacturing costs. The pioneer work on CZTS demonstrated from the molecular solution process for the first time is critical for paving future research directions for CZTS technology that takes advantage of the success of previous materials while slowly eliminating their disadvantages

Among solution processing approaches, hydrazine solution process to dissolve metal chalcogenides presents a viable route to yield impurity free high quality CISS film. The approach is unique due to the unique chemistry of hydrazine that dismantles metal chalcogenides into molecular species and allows them to intermix in solution on the molecular level. Raman spectroscopy on the precursor solution reveals the mechanism of dissolution and verifies the molecular homogeneity. The hydrazine solvent is volatile and capable of decomposing into gaseous products upon intermediate temperature annealing yielding a final well-formed film. Without long range diffusion, the hydrazine precursor thus enables a low temperature synthesis route for high quality chalcopyrite CISS with excellent uniformity. Therefore, solution processing is a feasible and attractive alternative

compared to existing techniques as it does not involve expensive vacuum-based steps or post-selenization step using $H_2Se$ at high temperature.

A new approach has been to introduce sodium into CISS film as a means to modify the properties of CISS absorber. Compatible with the solution processing, the approach provides a simple method to control the extrinsic dopants critical in reducing carrier recombination in absorber. Separating the doping step from the usually adopted soda lim glass, it allows the deposition to be applied on flexible substrates compatible with the low temperature process. Transparent device structure was also demonstrated perquisite for tandem structure which in theory harvest solar spectrum more efficiently. From this technique, the power conversion efficiency was successfully achieved up to 11%. Further improvements are needed to reduce the serial resistance by coarsening the grain size, tuning back contact, and reducing the recombination rate in absorber from defect passivation.

The availability of indium and tellurium might impede CIGS/CdTe solar cells from reaching TW production. Earth abundant kesterite CZTS exhibits optical and electronic properties comparable to those of the CIGS and CdTe material systems while avoiding the scarcity and cost issues associated with indium or tellurium. In addition, CZTS avoids the toxicity and environmental issues associated with cadmium. Therefore, CZTS shows great potential toward both economic and ecological device production. A reliable fabrication route for producing single phase kesterite material has been demonstrated as the platform for an in-depth exploration of its intrinsic materials properties and ultimately the identification of avenues toward further improvement.
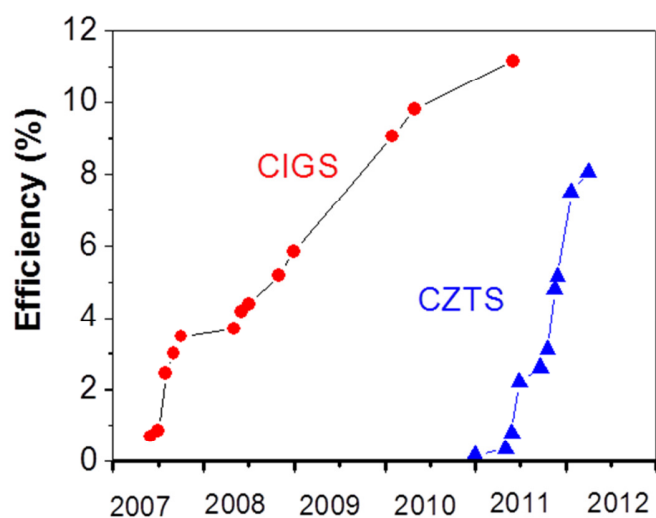
**Figure 6.1** Efficiency progress for hydrazine solution processing CIGS and CZTS thin film solar cells at UCLA**.**

For the first time, a molecular level homogenous CZTS precursor solution was developed. The novel solution-based approach overcomes the previous solubility limitations of zinc by introducing a hydrazine derivative thus forming soluble metal hydrazine & hydrazine derivative compounds. The progress on the chemistry enables fully dissolved hydrazine-based CZTS precursor complexes intermixing on the molecular level in solution. The approach allows for precise stoichiometric control and a kinetically favorable reaction route to form single phase kesterite CZTS with substantial flexibility in tailoring its optoelectronic properties. This technique not only provides a lower cost deposition route, solution processing provides sophisticated control over the stoichiometry and phase purity that are comparable or even better than conventional vacuum-based high temperature approaches. Vacuum processing at high temperatures are unfavorable processing conditions because of the high volatility of several elemental constituents and narrow compositional stability window of the CZTS phase. The CZTS photovoltaic

106

devices produced through solution processing have shown performance rivaling the best devices of its class to date.

The molecular solution processing technique provides a perfect platform for studying and improving CZTS solar cells. To further improve the device performance, comprehensive analysis on electronic properties has been initiated to correlate materials processing, materials properties, and device performance. Of particular importance are the defects that determine carrier recombination and collection rates. The influence of sulfur content in CZTSSe alloys on photovoltaic performance was studied. The trend suggests Se-rich compositions leads to overall better photovoltaic performance. This effect was studied by examining defects properties through admittance spectroscopy and carrier density profiling measurements. These measurements reveal that high sulfur content devices showed higher defect energy level (0.183 eV) as well as high bulk defect density ($8.2 \times 10^{15}$ cm$^{-3}$). These defect properties lead to the strong recombination losses as indicated by low external quantum efficiency values and a large $V_{oc}$ deficit. The relative large hysteresis effect shown in CZTS transistor device indicates a large amount of charge traps in the film. Thus it suggests interface recombination counts for the main loss of CZTS device output, that is the relative large $V_{oc}$ deficit, and loss in fill factor. These findings provide a better understanding of defect properties in kesterite alloys, which are critical for the control of recombination processes, doping, and junction formation in solar cells fabricated from this material. For a transistor device based on a CZTS channel layer, a similar level of mobility to CIGS make from the similar way was observed. This favorable mobility suggests the potential for CZTS to achieve high efficiency photovoltaic devices. Breakthroughs on defects engineering and interface recombination

control is expected to advance the performance of this material system to next level and make it comparable with its analogue CIGS system.

The successful implementation of molecular solution processing from a homogeneous and stable precursor would provide an alternative, more robust approach to processing multinary compounds compared with physical vapor deposition. The key issue requires specific molecular structure design and solvent selection to form the homogeneoussolution. The molecular structure of metal atom chelated by hydrazine and hydrazine derivatives, exemplified in zinc complex of $Zn(NH_2NH_2)_2(NH_2NHCOO)_2$, provides a new model to incorporate materials into molecular solution in hydrazine and other possible solvents. The generation of complex chelated by hydrazine/hydrazine derivativeovercomes the solubility limitation of materials in hydrazine. It is thus expected to substantially expand the current spectrum of materials processable using the concept invented by Mitzi to dismantle metal chalcogens with excess chalcogen forming MCC dispersions in hydrazine. The identified molecular structure is also able to guide solvent selection to forming readily dissolved molecular precursor beyond hydrazine. We anticipate this concept of molecular solution processing to have widespread impact on processing other high quality semiconducting materials and be competitive with evaporation, sputtering, and nanoparticles-based approaches for a variety of optoelectronic devices application.